# Multiscale Modeling of Mechanical Shock Behavior of Environmentally-Benign Lead-Free Solders in Electronic Packaging

by

Huiyang Fei

A Dissertation Presented in Partial Fulfillment
of the Requirements for the Degree
Doctor of Philosophy

Approved June 2011 by the
Graduate Supervisory Committee:

Hanqing Jiang, Co-Chair
Nikhilesh Chawla, Co-Chair
Amaneh Tasooji
Barzin Mobasher
Subramaniam Rajan

ARIZONA STATE UNIVERSITY

August 2011

ABSTRACT

With the increasing focus on developing environmentally benign electronic packages, lead-free solder alloys have received a great deal of attention. Mishandling of packages, during manufacture, assembly, or by the user may cause failure of solder joint. A fundamental understanding of the behavior of lead-free solders under mechanical shock conditions is lacking. Reliable experimental and numerical analyses of lead-free solder joints in the intermediate strain rate regime need to be investigated.

This dissertation mainly focuses on exploring the mechanical shock behavior of lead-free tin-rich solder alloys via multiscale modeling and numerical simulations. First, the macroscopic stress/strain behaviors of three bulk lead-free tin-rich solders were tested over a range of strain rates from 0.001/s to 30/s. Finite element analysis was conducted to determine appropriate specimen geometry that could reach a homogeneous stress/strain field and a relatively high strain rate. A novel self-consistent true stress correction method is developed to compensate the inaccuracy caused by the triaxial stress state at the post-necking stage. Then the material property of micron-scale intermetallic was examined by micro-compression test. The accuracy of this measure is systematically validated by finite element analysis, and empirical adjustments are provided. Moreover, the interfacial property of the solder/intermetallic interface is investigated, and a continuum traction-separation law of this interface is developed from an atomistic-based cohesive element method.

The macroscopic stress/strain relation and microstructural properties are combined together to form a multiscale material behavior via a stochastic approach for both solder and intermetallic. As a result, solder is modeled by porous plasticity with random voids, and intermetallic is characterized as brittle material with random vulnerable region. Thereafter, the porous plasticity fracture of the solders and the brittle fracture of the intermetallics are coupled together in one finite element model. Finally, this study yields a multiscale model to understand and predict the mechanical shock behavior of lead-free tin-rich solder joints. Different fracture patterns are observed for various strain rates and/or intermetallic thicknesses. The predictions have a good agreement with the theory and experiments.

To my wife and parents, whose love and encouragement have helped me to overcome so many obstacles in order to achieve so much.

ACKNOWLEDGMENTS

First and foremost I would like to express my sincerest gratitude to my advisor and chair, Professor Hanqing Jiang. His guidance and support have helped me to overcome obstacles that I would not be able to defeat on my own. I have benefited from his dedicated cultivation and patience to deal with every subtle problem with me. He has provided abundantly help and valuable advices on my research, life and career, in past four years. I attribute the level of my PhD degree to his encouragement and effort.

I would also like to offer my special gratitude to my co-advisor, Professor Nikhilesh Chawla. His great depth of knowledge that he imparted freely has enabled me to learn an unbelievable amount, and his enthusiasm and professionalism have made it an honor working with him. The solid and unreserved collaboration between Professor Jiang and Professor Chawla brought this work to its fruition. I could not express how grateful and appreciative I am of being a PhD student of both of them. Their mentoring will be a forever fortune for me.

My sincere thanks also go to my dissertation committee: Prof. Amaneh Tasooji, Prof. Barzin Mobasher, Prof. Subramaniam Rajan and Prof. Pedro Peralta (former committee member), for their encouragement, insightful comments, and valuable time.

I am indebted to many of my colleagues who have supported me and made this dissertation possible. I am grateful to Kyle Yazzie, who has done most of the

experiments supporting my modeling and simulations. Sincere thanks are also given to other colleagues: Amit Abraham, Dr. Cunjiang Yu, Dr. Jason Williams, Jiaping Zhang, Joseph Shaffer, Dr. Ling Jiang, Rongjun Zhang, Swathisri Kondagari, Teng Ma, Yonghao An, Yuping Pan and so on. They deserve thanks for providing me with many insightful discussions and instant helps on my research and personal life.

Finally, I am grateful for financial support from the National Science Foundation, Division of Materials Research — Metals Division. Special thanks also go to Fulton High Performance Computing Initiative at Arizona State University. And I would also like to thank supportive staff and administrators of the mechanical engineering program and School for Engineering of Matter, Transport and Energy.

TABLE OF CONTENTS

Page

CHAPTER Page

LIST OF TABLES

LIST OF FIGURES

Figure Page

Figure Page

# CHAPTER 1

# INTRODUCTION

## 1.1 Background and Motivation

In recent years, we are experiencing a fast development of modern microelectronic technology, which results in a change of our lifestyle. Many electronic devices have become a necessity in our daily life, as they make our life easier and more efficient. These electronic products are found in many areas of our life, including office, school, home, communication and entertainment, and now it is tough to imagine a life without them.

With the increasing demand on performance from advanced electronic circuits, especially nowadays mobile and compact electronic products, electronic packaging is facing new challenges. Electronic packaging is the bridge to connect the circuits on silicon chips to the outside world. Electronic packages and products, particularly personal portable electronics, may be subject to relatively low cycle stresses, such as the experience of dropping a cell phone or a laptop. Due to the demand on mobility and compactness of new electronic products, engineers encounter more severe mechanical, thermal and material issues [1-7].

In electronic packaging field, solder interconnect plays a critical role in the reliability of the overall package, and it provides electrical, thermal and mechanical continuity in all levels of assemblies. The performance and quality of solder alloys is extremely important because solder joints must retain their mechanical integrity under some severe conditions, such as mechanical shock,

vibration and thermo-mechanical fatigue [1-3]. The microstructure and macroscopic behavior of the solder alloys are of great interest [8-11]. In addition, an intermetallic layer grows from the reaction between liquid solder and the substrate during reflow. The thickness and morphology of the intermetallic compounds also significantly affect the performance of the solder joints [12-15]. Therefore, it is critical to study the mechanical behavior of solder alloys, intermetallics and the interface between solder and intermetallics.

Environmental concerns are more and more important when developing new techniques in electronic packaging. In the United States, about 70% of heavy metals in landfills come from discarded electronics, while electronic waste represents only 2% of America's trash in landfills [16]. The Consumer Electronics Association (CEA) says that U.S. households spend an average of $1,400 annually on an average of 24 electronic items. The U.S. National Safety Council estimates that 75% of all personal computers ever sold are now gathering dust as surplus electronics. Millions of redundant computers, home electronics and their highly toxic components are storing up a huge hidden environmental problem. Electronics contain toxic heavy metals such as lead, cadmium, mercury and chromium, all carcinogenic and not easily degraded. The elimination of toxic metals in electronics is of great environmental and social benefits, and more and more people and societies are working hard on it.

With respect to solder materials, the eutectic Pb-Sn alloy is conventionally the main choice for solder interconnects, because of its low melting point,

excellent wetting characteristics, and adequate creep and thermal fatigue strength [17-19]. Lead (Pb) damages the nervous system and causes brain disorders. Excessive lead also causes blood disorders in mammals. Lead poisoning has been documented thousand years ago, from ancient Rome, ancient Greece, and ancient China, but ironically, it is still widely used in electronic industry in modern era.

Fortunately, environmentally-benign Pb-free solders have received more and more attentions nowadays [1, 4, 20-26]. On July 1, 2006 the European Union Waste Electrical and Electronic Equipment Directive (WEEE) and Restriction of Hazardous Substances Directive (RoHS) came into effect prohibiting the intentional addition of lead to most consumer electronics produced in the EU. California recently adopted a RoHS law and China has a version as well. Manufacturers in the U.S. may receive tax benefits by reducing the use of lead-based solder. Approximately 70 Pb-free solder alloy compositions have been proposed so far [4]. Scientists and engineers are working on the new alloys manufacturing, selection, and reliability test and so on.

Reliability and performance of any product rely on the understanding of the weakest parts in a given design. In electronic packaging, solder joints under various mechanical and thermal loadings are considered as one of the weakest spots [3, 4, 17, 19, 26]. Therefore, numerous efforts have been made to improve the reliability of the entire electronic package or product by characterizing the mechanical and thermal behavior of solder interconnects [1, 2, 7, 9, 18, 20, 22]. As mentioned above, in daily use, the electronic products are typically subject to

relatively low cycle stresses, such as the experience of dropping a cell phone or a laptop. The strain rates of solders in these mechanical shock cases are somewhere between the strain rate ranges of quasi-static and dynamic impact.

## 1.2 Objectives

This dissertation aims to a systematic study of the mechanical shock behavior of lead-free tin-rich solder alloys and the joints at intermediate strain rates. A sophisticated experimental system is developed to control the strain rate and quantify the stress and strain relations on solder joints, as well as bulk solder alloys. Experiment data are used for developing accurate rate-dependant constitutive relations for finite element models. The material property and geometry effects of the intermetallics are investigated. An atomistic-based interfacial constitutive law for the interface between solder and intermetallic is developed. By combining the above constitutive relations together, a meaningful and predictive model for the mechanical shock behavior of the Pb-free solder joints is established. The overall reliability and failure mechanism of solder joints are investigated.

## 1.3 Dissertation Overview

Chapter 1 provides a brief background regarding the mechanical shock reliability issue and environmental concern in electronic packaging.

Chapter 2 presents the macroscopic behavior of the bulk Pb-free solder alloys under mechanical shock conditions. Finite element analysis is conducted to determine appropriate specimen geometry that can balance a homogeneous

stress/strain field and a relatively high strain rate. Three Pb-free solders are tested at the strain rate of 0.001/s to 30/s by Kyle Yazzie in Prof. Chawla's group. A novel self-consistent true stress correction method is then developed to correct the raw data obtained by experiment.

In Chapter 3, in order to study the mechanical behavior of micron-level intermetallics, the micro-pillar compression technology is introduced. A series of FEA simulations of both elastic and plastic materials is conducted, and empirical adjustments to the stress and strain measurement are provided. A simple brittle fracture FE model of the intermetallic compound $Cu_6Sn_5$ is just established.

In Chapter 4, an analytical traction-separation law for solder/intermetallic interface is developed based on an atomistic cohesive element method, namely Modified Embedded Atom Method (MEAM). Then the atomistic-based discrete pair potential is used to develop a continuum traction-separation relation. The cohesive fracture model is studied by finite element analysis.

Chapter 5 considers the overall mechanical reliability and failure mechanism of single solder joints. A porous plasticity model is applied to solder materials to characterize the void-induced fracture. The correlation between microstructure of void distribution and macroscopic behavior of the solder joint is studied. Moreover, plasticity fracture of the solders and brittle fracture of intermetallics are coupled together in one finite model. Failure mechanisms of the solder joints are investigated and theoretical explanations are provided.

Finally, the entire dissertation is summarized in Chapter 6.

# CHAPTER 2

# MECHANICAL SHOCK BEHAVIOR OF BULK LEAD-FREE SOLDERS

## 2.1 Introduction

Mishandling of packages, during manufacture, assembly, or by the users may cause failure of solder joints, and consequently the failure of the product. While we now have a good understanding of microstructure, creep, and thermal fatigue behavior of Pb-free solders [27-31], other important issues related to deformation in these materials remain to be addressed. A fundamental understanding of the behavior of Pb-free solders under mechanical shock conditions, however, is lacking. In particular, reliable experimental stress-strain data, over a range of strain rates needs to be obtained for reliability models.

A variety of experimental techniques have been developed to characterize the strain-rate dependent behavior of materials [32]. Figure 2.1 shows classical strain rate regimes used to classify material behavior. Conventional screw-driven machines can be used to quantify creep and stress relaxation processes, at very slow strain rates. In the high end or impact regime, plate impact is typically used. The strain rates obtained during mechanical shock of solders, such as that experience by dropping a cell phone of laptop, are somewhere between the quasi-static and dynamic impact strain rate range. In fact, a precise value or range of strain rate for these applications has not yet been established. The range from a variety of studies is somewhere between $10^{-1}$/s and $10^{2}$/s [33-39].

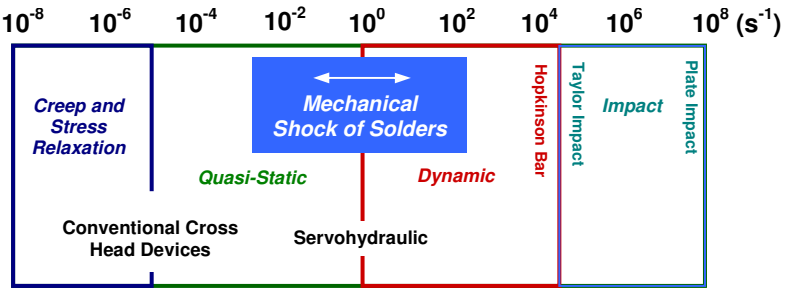


Figure 2.1. Schematic of classification of material behavior in different strain-rate regimes (after [32]). Mechanical shock of solders falls in an intermediate strain rate regime. (Courtesy of Prof. N. Chawla)

A promising technique that has yet to be applied to dynamic testing of solders is impact using servohydraulic methods. Boyce and Crenshaw [40] have demonstrated that controlled strain rates of up to 500/s can be obtained on relatively small specimens using modified servohydraulic methods. Thus, this is a highly desirable technique needed to characterize the mechanical shock of solders in the "intermediate" strain-rate regime.

In this chapter, the mechanical shock behaviors of three bulk Pb-free solders are investigated. First, a finite element model is built to study the gage length effect and obtain a relatively uniform stress (and strain) distribution within the gage section of the specimen. This is followed by a presentation of numerical study of true stress correction in the measurement of stress/strain data in the uniaxial tension test. A high-accuracy self-consistent approach is developed to correct the experimentally measured axial stress for post-necking stage. The accuracy of this methodology is guaranteed by using the criterion of the self-consistence between the experimentally measured and the calculated axial stress from finite element analysis. The accurate equivalent true stress/strain relations

thus can be obtained and used in modeling and theoretical studies. The strain rate effect is also considered in this approach. The correction functions for three Pb-free solders are provided explicitly. This approach can be applied to any material in either round or rectangular geometry, as long as the engineering stress/strain relation is accurately measured.

Moreover, a double-necking phenomenon is observed in the uniaxial tension test on an ASTM E-8M specimen with a 25-mm gage length, which is not observed on other shorter sample (i.e. 10-mm gage length). Finite element model is built for the dog-bone uniaxial tension test with varying gage length and loading strain rate. FEM results of the dynamic behavior of the longer specimens correlate very well with the experimental observations. In particular the trends observed in experiments could be rationalized based on the FEM modeling results.

## 2.2 Materials and Experimental Procedure

High purity cast ingots of Sn (Indium Corporation, Ithaca, NY and Alfa Aesar, Ward Hill, MA) are used in this study. The specimen and experiment were prepared by Kyle Yazzie in Prof. Chawla's group. The ingots are reflowed in an aluminum mold coated with graphite to yield rectangular blanks approximately 10.5 cm in length, 1 cm in width, and 0.8 cm in height.

Microstructure characterization is conducted after reflow and cooling. Samples are polished to a final finish with a 0.05 μm colloidal silica solution. Optical microscopy and image analysis of cross-sections of specimens are carried out in order to quantify the microstructure. Tensile specimens are machined from

a section near the bottom of the reflowed blank, where the cooling rate is measured. Microstructure characterization of the tensile specimens prior to testing indicated uniform microstructure throughout the samples.

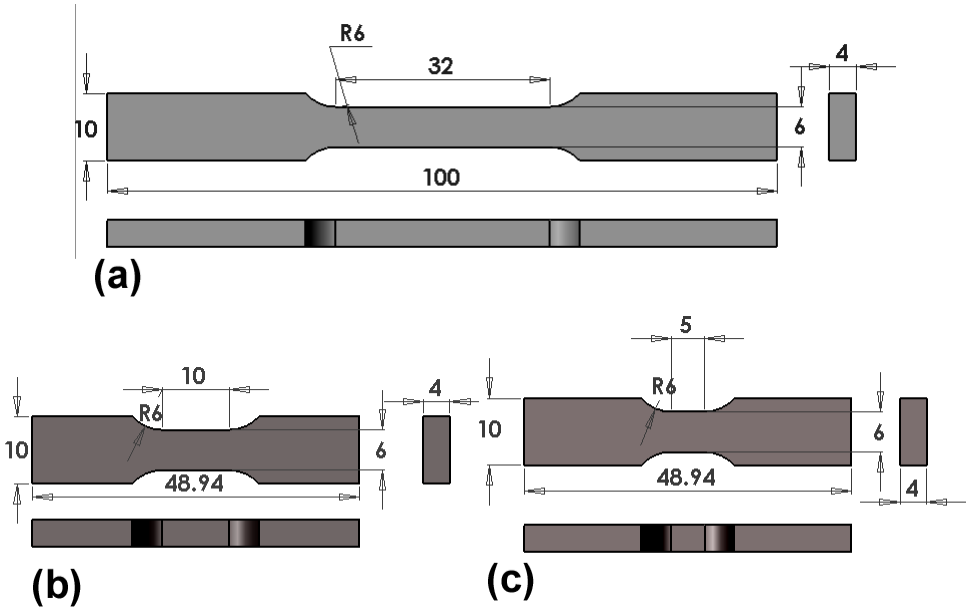


Figure 2.2. Specimen geometries for FEM. (a) ASTM E-8M specimen, (b) 10 mm gage length specimen, (c) 5 mm gage length specimen. All dimensions are mm. (Courtesy of K. Yazzie)

In the finite element modeling of the dog-bone tension, all dimensions, except gage length, are kept constant in order to study the change in stress heterogeneity as a function of gage length. Three specimen geometries are used: the ASTM E-8M standard geometry with a gage length of 25 mm and a total reduced section of 32 mm as shown in Figure 2.2(a), a small geometry with a gage length of 10 mm as shown in Figure 2.2(b), and a smaller geometry with a gage length of 5 mm as shown in Figure 2.2(c).

The overall length of the ASTM E-8M specimen is 100 mm, the overall length of the 10 mm gage length specimen is 48.94 mm, and the overall length of

the 5 mm gage length specimen is 48.94 mm. All three specimens have a width of 6 mm, a thickness of 4 mm in the gage length, a width of 10 mm in the grip sections, and fillet radii equal to 6 mm. Only the ASTM E-8M standard geometry specimen and the 10 mm gage length specimens are used for tensile testing. Tensile tests are performed on a servo-hydraulic load frame, in displacement control, to achieve a nominal strain rate of 10/s.

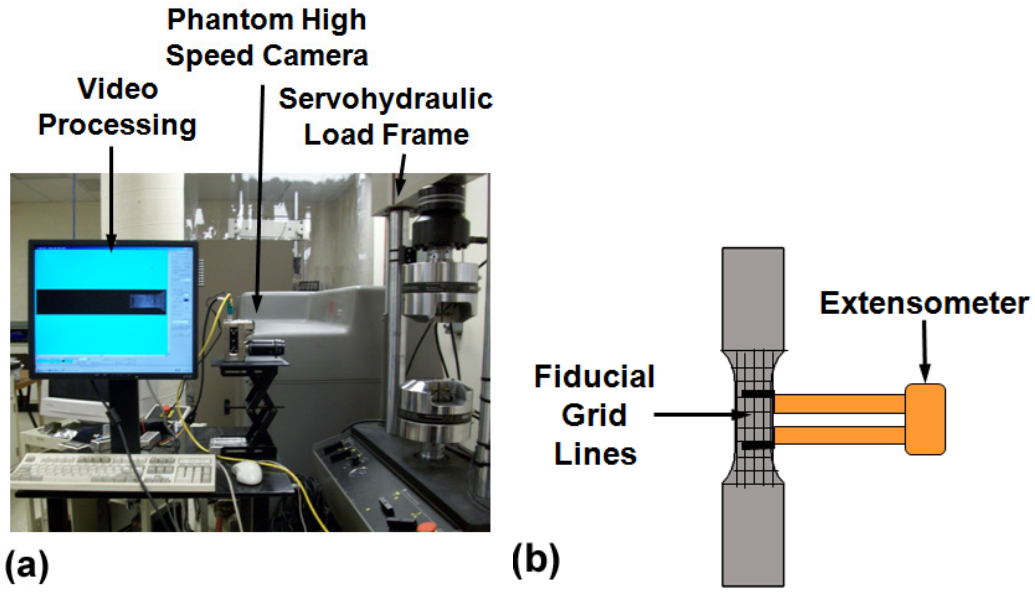


Figure 2.3. (a) Setup for high-speed camera system and servohydraulic load frame. (b) Strain measurement: displacement of fiducial lines and extensometer. (Courtesy of K. Yazzie)

An ultra-high speed camera (Phantom, Vision Research Corporation) with an acquisition rate of 2100 frames per second (at its highest resolution) is used to measure strain on the solder specimen. Strain is calculated in two ways: (a) macroscopic strain given by an extensometer with 25 mm gage length and (b) local strain measured by digital images of fiducial lines on the specimen surface.

Figure 2.3a shows the experimental setup of the servohydraulic load frame, ultra-high speed camera, and video processing station. Figure 2.3b shows how fiducial lines are used in combination with an extensometer to calibrate the displacement rate using ASTM E-8M specimens. The size constraint of the extensometer precludes its use with the 10-mm and 5-mm specimens. Fiducial lines form a rectangular grid with a longitudinal spacing of 2.5 ± 0.1 mm and a transverse spacing of 1.5 ± 0.1 mm. The fiducial lines are scored using a razor blade.

## 2.3 Strain Rate Control and Specimen Geometry

High strain rate experiments in solders can be conducted in strain control or displacement control. Initial experiments conducted in strain control yielded a "lag" in the desired strain rate response. Thus, it is decided to conduct the experiments in displacement control. The strain rate $\dot{\varepsilon}$ is related to the applied displacement, $\Delta L$, as follows:

$$\dot{\varepsilon} = \frac{\varepsilon}{t} = \frac{\Delta L}{L} \cdot \frac{1}{t} \tag{2.1}$$

where $L$ is the gage length of the specimen and $t$ is time. The maximum displacement rate, $\Delta L/t$, is a function of the servohydraulic machine, flow rate, mass of the grips, etc. In our case, the maximum displacement rate possible was about 300 mm/s. Thus, the other way to increase the strain rate is to decrease the gage length, $L$. It should be noted that this must be done carefully because decreasing the gage length may yield a non-uniform stress distribution in the gage volume. In order to quantify this effect, finite element analysis is conducted to

determine the change in stress and strain state, when going from the ASTM E-8M sample (gage length 25 mm), to 10-mm and 5-mm samples. This is followed by experimental characterization at a strain rate of about 10/s and modeling of the effect of strain rate.

The ASTM E-8M, 10 mm gage length, and 5 mm gage length specimen geometries are modeled in order to quantify stress heterogeneity as a function of gage length. The constitutive response of the material used in the FEA is shown in Figure 2.4a, which is the true stress and true strain data from a tensile test of an ASTM E-8M specimen of furnace cooled pure Sn, conducted at a strain rate of 0.2/s. The effect of strain rate is not included, since these models are only used to quantify stress and strain heterogeneity. Only the gage section and fillet regions are considered in FEA. Since the grip sections are clamped in a tensile test, we consider it as fixed boundary conditions at the two ends. Figure 2.4b shows the gage section and fillet regions and the boundary conditions. ABAQUS/Standard is used to conduct static analysis, and the material input for FEA is shown in Figure 2.4a.

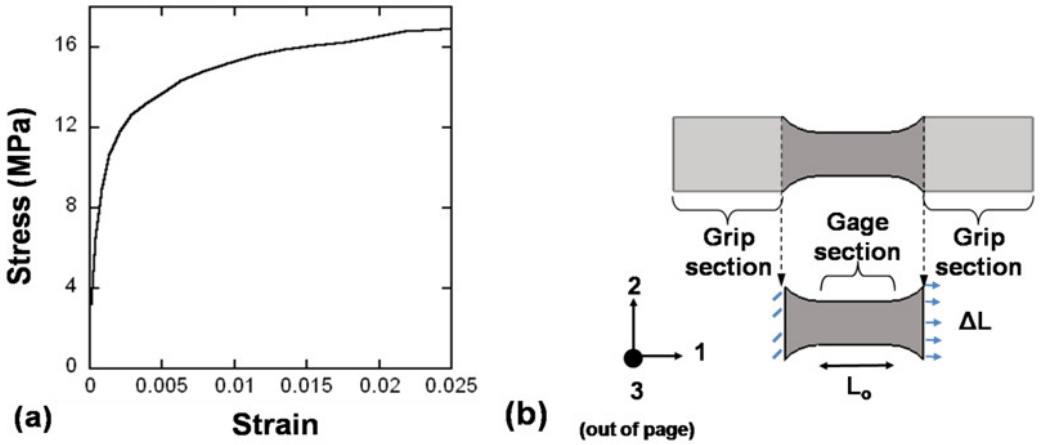


Figure 2.4. FE model for the gage length effect. (a) Constitutive material response, (b) Geometry and boundary conditions. (Courtesy of K. Yazzie)

A mesh of quadratic hexahedral elements is used. A mesh refinement study using the ASTM E-8M model is conducted by incrementally increasing the mesh density. No difference in the simulated stress-strain response nor the local stresses and strains is observed. All specimens are displaced to produce an equivalent strain of 0.02 in their respective gage sections. The average stress and standard deviation in the elements, measured over the gage sections of the models, are plotted versus applied strain in Figure 2.5a. Figure 2.5b shows that the 5 mm gage length model deviates most from the ASTM E-8M model and has the largest standard deviation for stress values. The 10 mm gage length specimen more closely approximates the stress-strain behavior of the ASTM E-8M model.

Figure 2.6 shows the axial strain ($\varepsilon_{11}$) for all three models. The 5 mm gage length model has the most heterogeneous strain distribution in the gage section, whereas the 10 mm gage length model has a reasonably wide region of uniform strain. The ASTM E-8M model has uniform strain throughout the entire 25 mm

gage section. Note that the 10 mm gage length geometry yields a stress-strain behavior that is similar to the ASTM E-8M geometry. Based on this analysis, the ASTM E-8M and 10 mm gage length geometry are used for the tensile tests reported here.

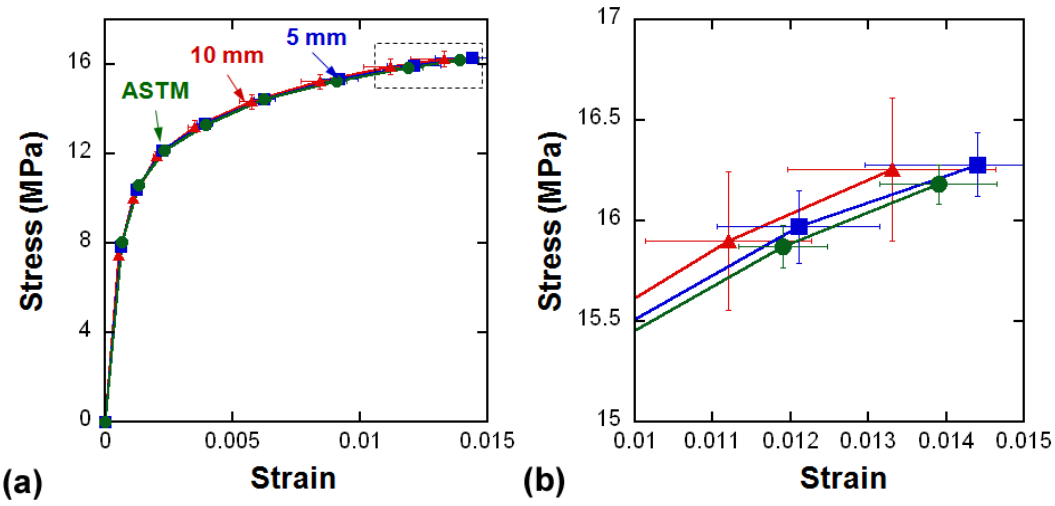


Figure 2.5. Comparison of stress–strain behavior for the different gage sections. (a) Average stress–strain curves and standard deviations (b) Magnified region close to ultimate tensile strength (UTS). (Courtesy of K. Yazzie)

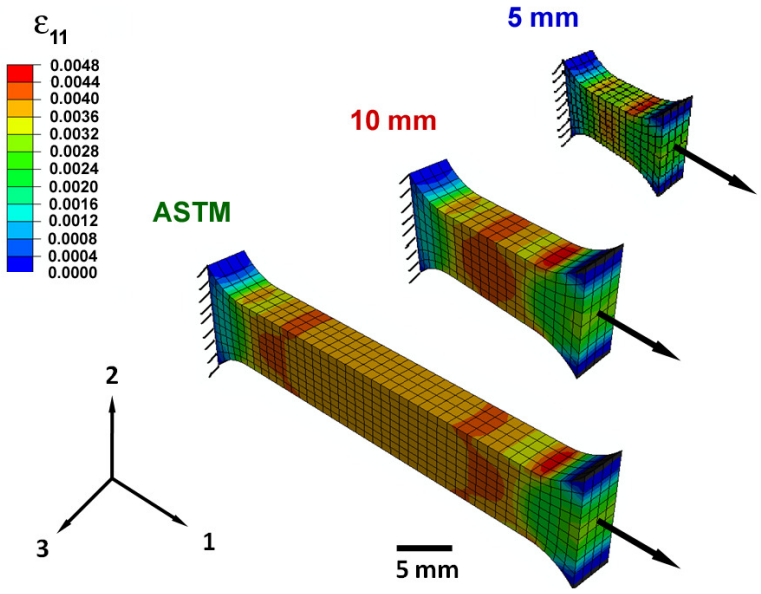


Figure 2.6. Contours of axial strain for all three models. (Courtesy of K. Yazzie)

Table 1.

Grain Size of Pure Sn Solder. (Courtesy of K. Yazzie)

| Orientation | Number of intercepts | Average Grain Size (μm) |
|---|---|---|
| Longitudinal | 203 | 36.5 ± 6.6 |
| Transverse | 107 | 72.5 ± 26.4 |

Microstructure characterization of the reflowed and machined pure Sn bar shows a fairly uniform grain structure, although some elongation of the grains is observed in Figure 2.7. Table 1 shows grain size measurements, based on the linear intercept technique. The microstructure of the specimens is also compared before after machining, and did not show any statistical difference.

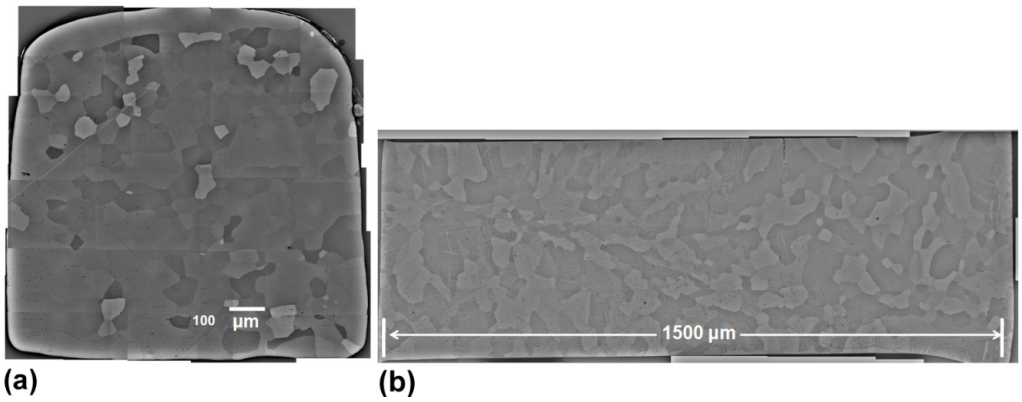


Figure 2.7. Microstructure of reflowed and machined pure Sn bars: (a) transverse microstructure and (b) longitudinal microstructure. (Courtesy of K. Yazzie)

Table 2 shows a summary of the ultimate tensile strength, strain-to-failure, and testing strain rate. The strain rate is about 10/s for both specimen geometries. Note that the $\sigma_{UTS}$ and strain-to-failure are also very similar, indicating that the 10 mm geometry is suitable for tensile testing, in this strain rate regime.

Table 2.

Tensile Results for ASTM and 10 mm Gage Length Specimen Geometry

(Courtesy of K. Yazzie)

| Specimen Geometry | Ultimate Tensile Strength (MPa) | Strain-to-failure | Strain Rate ($s^{-1}$) |
|---|---|---|---|
| 25 mm gage length | 42.3 ± 7.2 | 0.93 ± 0.09 | 9.8 ± 0.4 |
| 10 mm gage length | 44.5 ± 7.4 | 1.08 ± 0.18 | 9.9 ± 0.1 |

2.4 Experimental Results of Three Lead-Free Solder Alloys

By the experiment setup mentioned in section 2.2 and the geometry and loading control discussed in section 2.3, three Pb-free solders are tested at various strain rates in the mechanical shock regime, ranging from 0.001/s to 30/s. Three materials are recrystallized pure Sn, furnace-cooled Sn-Ag-Cu (SAC) and water-quench SAC, respectively, and their engineering stress/strain relations are shown in Figure 2.8. The yield stress and ultimate tensile stress increase, when the strain rate goes up. In other words, the material becomes stiffer at larger strain rate, and SACs are stiffer than pure Sn.

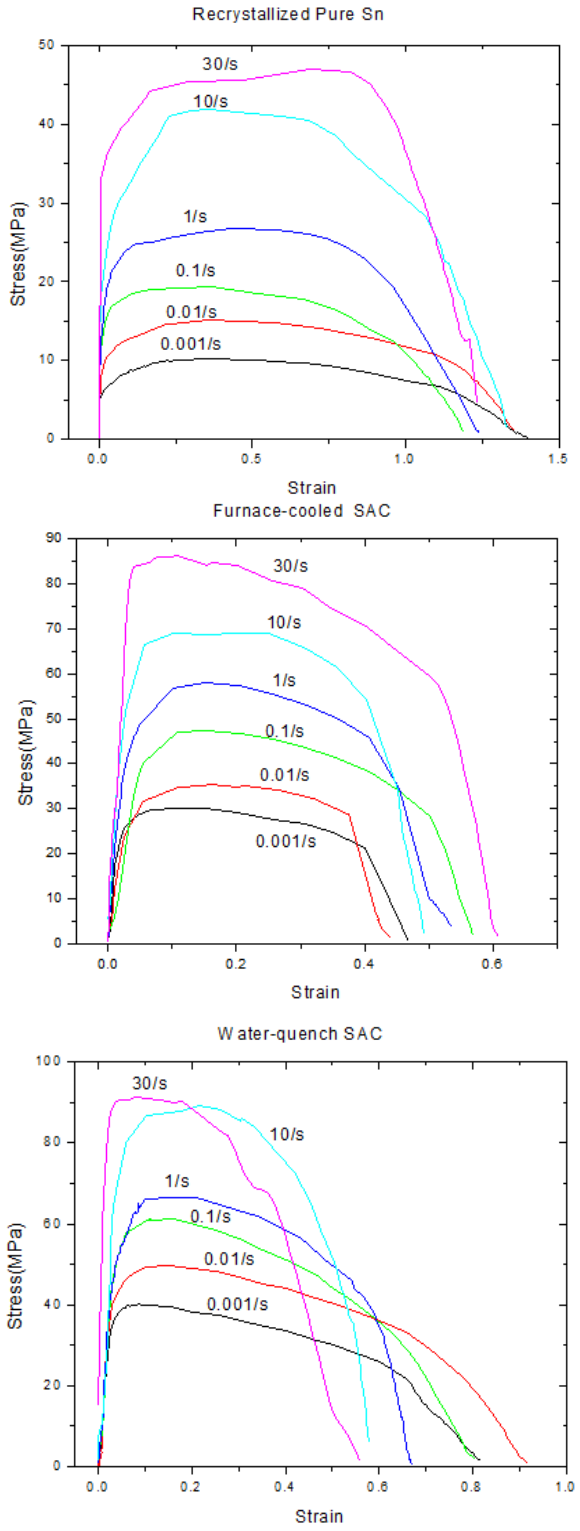


Figure 2.8. Engineering stress/strain relations obtained by experiments at different strain rate $\dot{\varepsilon}$ for (a) recrystallized pure Sn, (b) furnace-cooled SAC and (c) water-quench SAC. (Courtesy of K. Yazzie)

## 2.5 Stress/Strain Relation in Simple Tension Test

The measured stress-strain relations and other material parameters from the tensile test play vital roles on the theoretical analysis, both analytical and particularly numerical analysis. However, the engineering stress/strain relations obtained in section 2.4 is not the true stress/strain relation, which represent the constitutive response of the tested materials. Therefore, the accurate stress-strain relations are in demand for building high-fidelity modeling and simulations.

In a simple tension test, the axial load $P$ is prescribed and the axial elongation $\Delta L$ is recorded. $A_0$ is the original cross-sectional area of the specimen, $L_0$ is the original length. Engineering stress or nominal axial stress $s$ and engineering strain $e$ are defined as

$$s = \frac{P}{A_0},\ e = \frac{\Delta L}{L_0} \tag{2.2}$$

The load and elongation relation ($P$ vs. $\Delta L$ ) or equivalent engineering stress/strain ($s$ vs. $e$) relation can be obtained from the simple tension experiment. Engineering stress-strain is accurate for infinitesimal deformation.

For finite deformation (usually for plastic deformation), it is accurate to use the true stress and true strain. The true stress $\sigma$ is defined as the ratio of the uniaxial load to the instantaneous cross-sectional area, $\sigma = P / A$. Since the elastic deformation (compressible) is infinitesimal compared with the plastic deformation (incompressible), the incompressible condition can be applied and the true stress $\sigma$ is expressed via the engineering stress as

$$\sigma = s(1+e) \tag{2.3}$$

The true strain $\varepsilon$ is defined as the integral of the instantaneous engineering strain $d\varepsilon = dL / L$ over the entire length, and given by

$$\varepsilon = \ln(1+e) \tag{2.4}$$

With Equations (2.3)&(2.4), true stress/strain ($\sigma$, $\varepsilon$) relation can be easily obtained from the engineering stress/strain ($s$, $e$) relation. Figure 2.9 illustrates a typical stress/strain diagram for a conventional metal. True stress/strain relation collapses with the engineering stress/strain relation for small deformation and divides from that for large deformation.

It should be noted that the analysis in this section is based on the assumption of uniaixal stress state. In the uniaxial stress state, the axial stress is the only non-vanishing stress component and equates the equivalent true stress given by $\sigma_{eq} = \sqrt{\frac{3}{2}\sigma'_{ij}\sigma'_{ij}}$ , where $\sigma'_{ij} = \sigma_{ij} - \frac{1}{3}\sigma_{kk}\delta_{ij}$ is the deviatoric stress. The relation between the equivalent stress $\sigma_{eq}$ (or von Mises stress) and the strain is adopted as the material model for theoretical analysis.

When the stress-strain curve goes beyond the onset of necking in Figure 2.9, the cross-sectional area is not uniform anymore, and moreover, the stress state at the necked region is no longer uniaxial but rather triaxial.

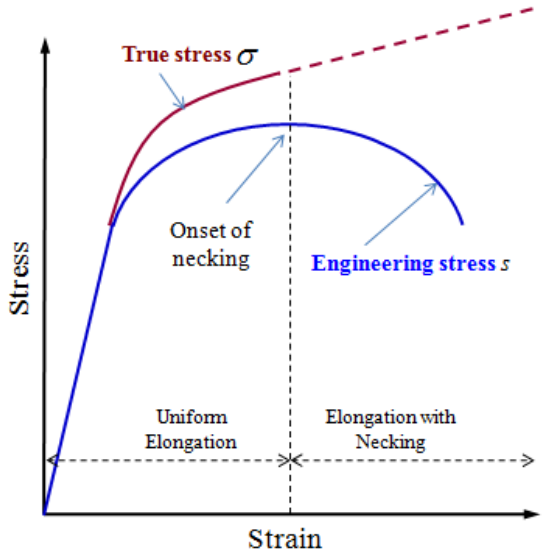


Figure 2.9. Illustration of the engineering stress/strain and true stress/strain.

To illustrate the triaxial stress state, a rod model with round cross-section is constructed. The geometry of the rod is shown in Figure 2.10a, and it is subjected to uniaxial tensile loads at two ends, which are gripped. The simulation is carried out via commercial finite element analysis package ABAQUS [41], and there are 18,500 three-dimensional eight-node brick (C3D8) elements in the model. The stress contours of the cross-section of the necked region are shown in Figure 2.10b. The left panel of Figure 2.10b shows that prior to necking, the stress state of the cross-section is uniaxial and uniform, i.e., the radial stress $\sigma_{rr}$ and circumferential stress $\sigma_{\theta\theta}$ are close to zero and only the axial stress $\sigma_{zz}$ presents. After necking, the right panel of Figure 2.10b shows that the stress state changes to triaxial, i.e., $\sigma_{rr}$ and $\sigma_{\theta\theta}$ develop and become comparable to $\sigma_{zz}$ (10MPa comparing to 30MPa). The triaxial stress state after necking makes the true stress given by Eq. (2.3) can only represent one non-zero stress component $\sigma_{zz}$, but not

the accurate the stress state (with $\sigma_{rr}$, $\sigma_{\theta}$ and $\sigma_{zz}$). Because of the same reason, the equivalent true stress after necking is different from axial stress $\sigma_{zz}$. In order to differentiate the uniaxial and triaxial stress states prior to and after necking, solid and dashed lines are used to represent the axial stress $\sigma_{zz}$ before and after necking, respectively. It should be emphasized that the axial stress $\sigma_{zz}$ prior to necking has more clear physical meaning than that after necking because the former is just the equivalent stress and the latter is not, i.e.,

$$\begin{cases} \sigma_{eq} = \sigma_{zz} & \text{prior to necking} \\ \sigma_{eq} \neq \sigma_{zz} & \text{after necking} \end{cases} \tag{2.5}$$

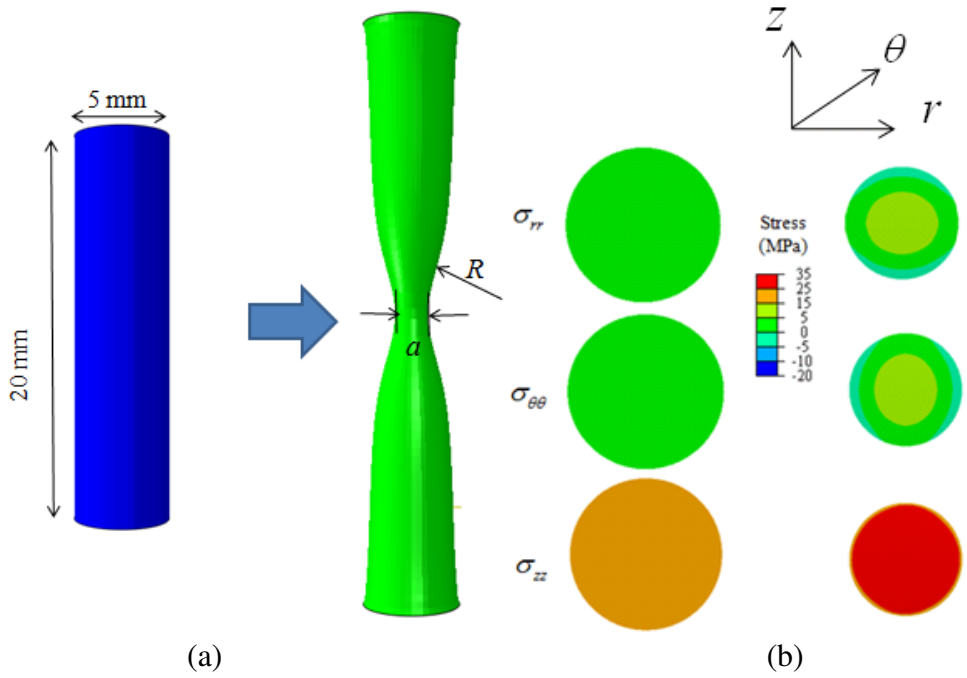


Figure 2.10. A sample with round cross-section under uniaxial tension. The stress state is uniaxial prior to necking and becomes triaxial after necking.

Since the relation between the equivalent stress and strain is of great importantce in theoretical analysis, especially for the large deformation elastic-

plastic analysis and fracture problems, it is extremely important to obtain the equivalent stress from the experimentally measured axial stress, which is different from the equivalent stress after necking. This requires a correction, either analytical or empirical, from the experimentally measured stress/strain to the true stress/strain.

## 2.6 True Stress Correction

### 2.6.1 Review of Previous Work

The correction of true equivalent stress/strain relations can be dated back to 1950's. Bridgman [42] studied the stress distribution in the necked region of a simple tension sample with a round cross-section, and developed an analytical method to obtain the true equivalent stress/strain relation from the experimental measurement. Two parameters, the curvature of the necked region $R$ and the radius of the specimen $a$ were introduced in this approach (Fig. 2.10). This correction is named as Bridgman correction, which has been widely used [43-47], although there are some limitations. The major limitation is that the Bridgman correction can be only applied to the cases with round cross-sections.

In Bridgman's correction [42], the stress state in the necked region of a simple tension specimen with a round cross-section was studied analytically and the true equivalent stress $\sigma_{eq}$ was related to the experimentally measured axial stress $\sigma_{zz}$ (defined by Eq.(2.3)) via

$$\sigma_{eq} = \frac{\sigma_{zz}}{(1+\frac{2R}{a})\ln(1+\frac{a}{2R})} \tag{2.6}$$

where $R$ is the radius of curvature in the necking, and $a$ is the radius of the specimen (Fig. 2.9). Eventually, a unified expression of the true equivalent stress $\sigma_{eq}$ (for both uniaxial stress state prior to necking and triaxial stress state after necking) in terms of the axial stress $\sigma_{zz}$ was obtained as

$$\sigma_{eq} = \sigma_{zz} \cdot \zeta , \tag{2.7}$$

where,

$$\zeta = \begin{cases} 1 & \text{prior to necking} \\ \dfrac{1}{(1+\dfrac{2R}{a})\ln(1+\dfrac{a}{2R})} & \text{after necking} \end{cases} \tag{2.8}$$

$\zeta$ is the correction coefficient. Equation (2.8) indicates that the equivalent true stress $\sigma_{eq}$ is a one-to-one linear function of the axial stress $\sigma_{zz}$. Once the geometry of the necking region (i.e., $R$ and $a$) is measured, the correction coefficient $\zeta$ then can be calculated and thus the true equivalent stress $\sigma_{eq}$ can be obtained from the axial stress $\sigma_{zz}$, i.e., the red solid and dashed lines in Fig. 2.12.

Since specimens with rectangular cross-sections are also widely used, many efforts have been devoted to develop the correction function for this type of specimen. Aronofsky [48] used an analytical method to study the stress state at the necked section of rectangular specimen, and found that the stress distribution was not uniform. Ling [49] developed a half-analytical method called weighted average method to calculate true equivalent (von Mises) stress from the axial stress, but the weight constants in the formula are difficult to determine. Choung and Cho [47] provided an empirical formula to calculate true equivalent stress of

steel for rectangular specimen based on the Bridgman correction. Two parameters were involved in this work, namely the curvature of the necked region (adopted from the Bridgman correction) and the hardening index $n$ (a material property). The involvement of the material property in the correction intrinsically limits the application to other materials, even though this correction has been used to study other materials without attentive justification.

Choung and Cho [47] established a new correction coefficient $\zeta$ for specimens with rectangular cross-sections. The new correction coefficient $\zeta$ is an empirical function obtained from the parametric finite element analysis of steel specimens, given as

$$\zeta = \begin{cases} 1 & \text{for } \varepsilon_{eq}^{p} \le 1.4n \\ \alpha(\varepsilon_{eq}^{p})^2 + \beta\varepsilon_{eq}^{p} + \gamma & \text{for } \varepsilon_{eq}^{p} > 1.4n \end{cases} \qquad (2.9)$$
$$\alpha = -0.0704n - 0.0275, \beta = 0.4550n - 0.2926, \gamma = 0.1592n + 1.024$$

where $\varepsilon_{eq}^{p}$ is the equivalent plastic strain and $n$ is the hardening exponent of the material. For uniaxial tension (both prior to and after necking), the equivalent plastic strain $\varepsilon_{eq}^{p}$ is identical to the true strain (Eq.(2.4)).

Finite element simulations, using ABAQUS/Standard [41], are executed to study the simple tension of a bar with rectangle cross-section. Figure 2.11c shows the geometry and meshes of the finite element analysis. The geometry is a quarter of the real specimen, and axisymmetric boundary conditions are applied on the two axisymmetric surfaces. The prescribed displacement load is applied on the two ends of the rectangular specimen. Eight-node brick elements (C3D8) are used

for discretization. Mesh sensitivity is studied, and a typical finite element mesh with 25000 elements that leads to converged results.

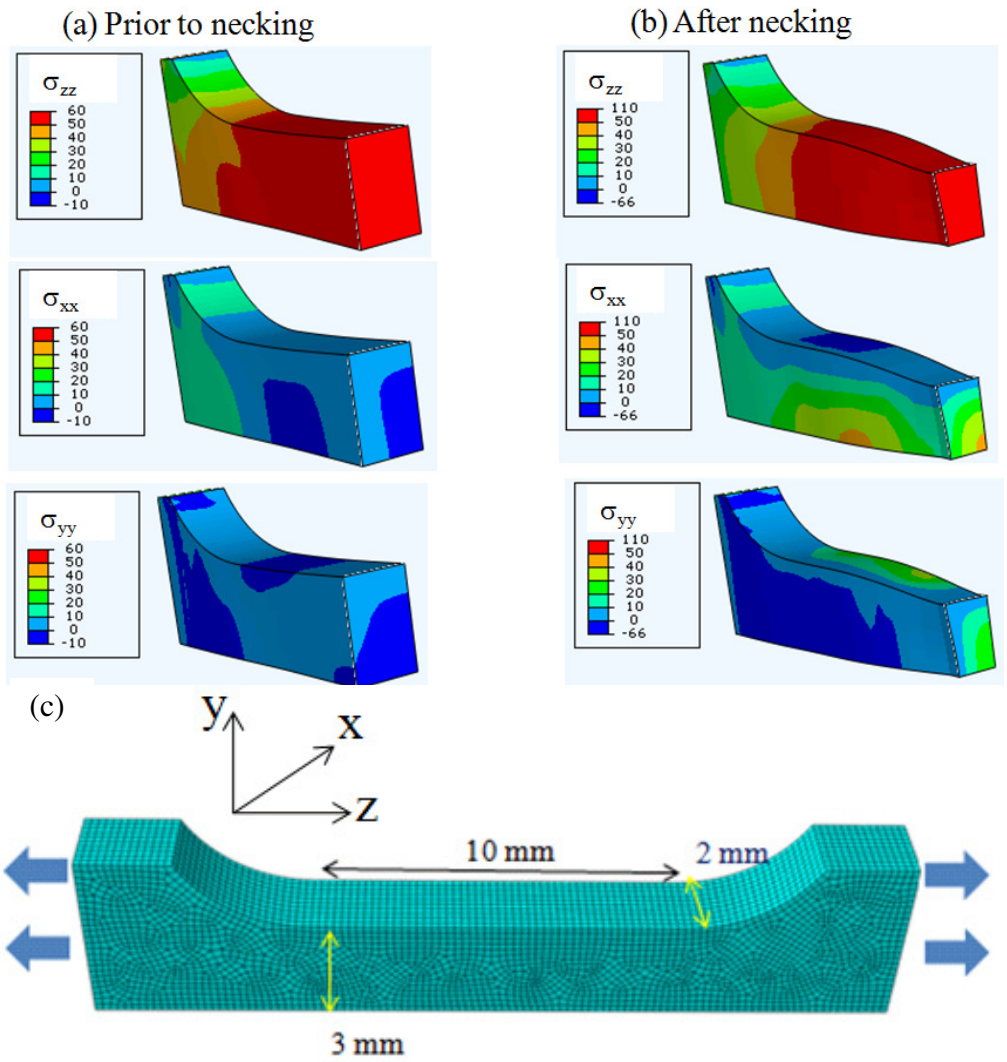


Figure 2.11. Symmetric FE model of 1/4 rectangular specimen under simple tension. (a) Uniaxial stress state prior to necking; (b) Triaxial stress state after necking; (c) Geometry and mesh.

Figures 2.11a & 2.11b clearly suggest that the stress state is uniaxial prior to necking and becomes triaxial after onset of necking. The cross sectional area of the rectangular specimen is irregular shape after necking. Appendix A explains how to measure local stress and strain at the necking zone. The pink curve in

Figure 2.12 is used as an assumed axial stress $\sigma_{zz}$/strain relation in the simulation. A power law was used, i.e., $\sigma_{zz} = \sigma_0 + K\varepsilon_p^n$, where $\sigma_0$ = 10 MPa is the yield stress, $n = 2$ is the hardening exponent and $K = 20$. The solid line presents the uniaxial stress state and the dashed line is the triaxial stress state.

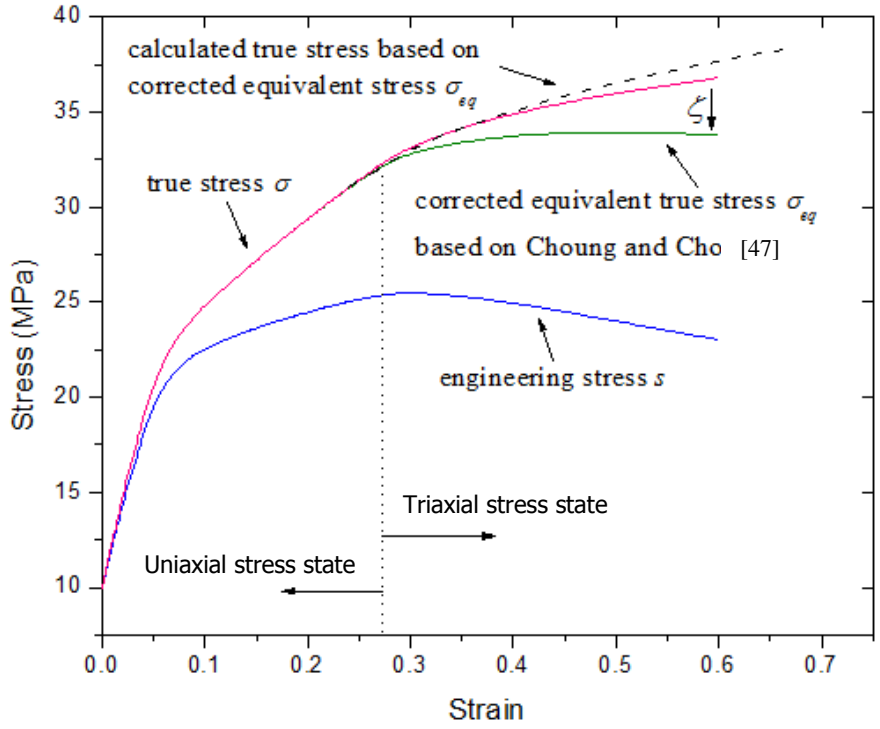


Figure 2.12. Stress/strain relation for one assumed material for which Choung and Cho's correction [47] is valid.

Based on the correction suggested by Choung and Cho [47], the curve in olive is the corrected equivalent true stress/strain relation that was used in the finite element simulation. With the corrected equivalent true stress/strain relation as the input for finite element analysis, the simulated axial stress $\sigma_{zz}^{theoretical}$ after necking was shown as the black curve, which approximately collapses with the assumed axial stress $\sigma_{zz}$. This simulation indicates that for the present assumed

axial stress/strain relation, Choung and Cho's correction [47] is able to give a means to obtain the correct equivalent true stress/strain relation.

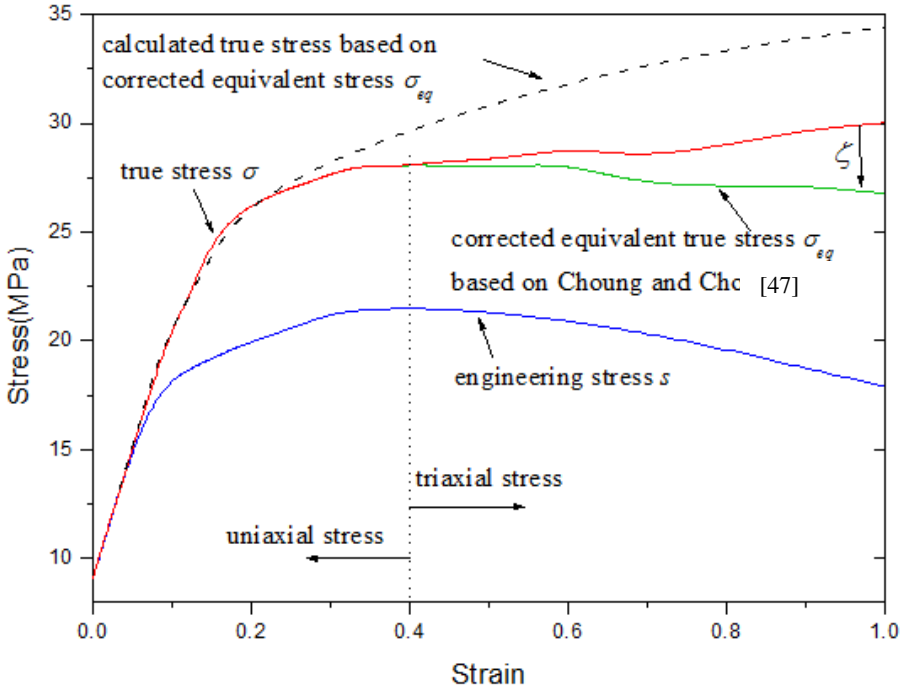


Figure 2.13. Stress/strain relation for one assumed material for which Choung and Cho's correction [47] is not valid.

Figure 2.13 shows another example with different assumed axial stress/strain relation, which is also given by the curve in pink. Unlike the case in Figure 2.12, the stress/strain relation in Figure 2.13 does not strictly obey power-law. The hardening exponent $n$ is obtained by calculating the slope of log(stress) vs. log(strain) curve up to the UTS, and in this case, $n \approx 0.259$ for the red curve in Figure 2.13. The corrected equivalent true stress/strain relation (olive curve) is obtained by following Choung and Cho [47]. However, one can find that based on the corrected equivalent true stress/strain relation, the simulated axial stress $\sigma_{zz}^{theoretical}$ obviously deviates from the assumed axial stress, which indicates that

Choung and Cho's method [47] is not a good correction for this axial stress/strain relation.

The two cases shown in Figures 2.13 & 2.13 indicate that Choung and Cho [47] does not hold for all materials. The reason may result from the appearance of the hardening exponent *n* in the correction function, which limits the application of this correction function to particular type of materials. In order to form a general method to formulate the correction function, a self-consistent method is developed and presented in Section 2.6.2.

2.6.2 A Self-Consistent Method for True Stress Correction

The criterion of stress correction is specified in the following. In experiment, the axial stress is calculated as the axial force divided by the area of the cross-section. Then the equivalent stress, which is the input for theoretical analysis, is just the measured axial stress prior to necking or obtained from the measured axial stress via a proper correction function. Based on the equivalent stress as input, the axial stress in theoretical analysis can be determined, which should accurately reproduce the experimental measured axial stress if the input (i.e., the equivalent stress) is correct. Therefore, the criterion for stress correction is that

$$\sigma_{zz}^{theoretical}\left(\text{based on corrected equivalent true stress}\right)=\sigma_{zz}^{experimental} \tag{2.10}$$

If the criterion in Eq. (2.10) is satisfied, the simulation and experimental results will agree to each other, as shown in Figure 2.14.

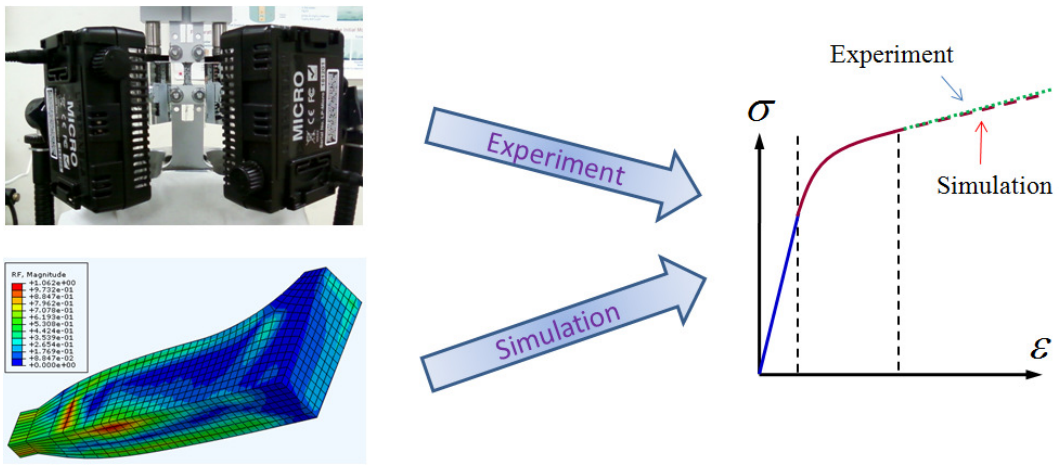


Figure 2.14. Consistency between simulation and experimental results.

A flow chart of this self-consistent method is provided in Figure 2.15. The correction firstly starts from a guessed correction function $\zeta$ and the equivalent stress $\sigma_{eq}$ is corrected based on the experimentally measured axial stress. Using the corrected equivalent stress $\sigma_{eq}$, the finite element analysis is conducted and the axial stress $\sigma_{zz}^{theoretical}$ is then calculated. Based on the theoretically calculated axial stress $\sigma_{zz}^{theoretical}$ and the correct equivalent stress $\sigma_{eq}$, a new correction function $\zeta^{new}$ can be obtained. Then the axial stresses in experiments $\sigma_{zz}^{experimental}$ and finite element analysis $\sigma_{zz}^{theoretical}$ will be compared via the least square method. When the correction coefficient of the least square method R is close to 1, $\sigma_{zz}^{experimental}$ and $\sigma_{zz}^{theoretical}$ thus very close, which indicates the correction is accurate. Then the correction function $\zeta$ is obtained. If not, the correction function $\zeta$ is updated by $\zeta^{new}$ and then the aforementioned procedure will be conducted again until the experimentally measured axial stress $\sigma_{zz}^{experimental}$

and calculated stress $\sigma_{zz}^{theoretical}$ closely collapse. Finally, the correction function is fitted to be a function of equivalent plastic strain $\varepsilon_p$.

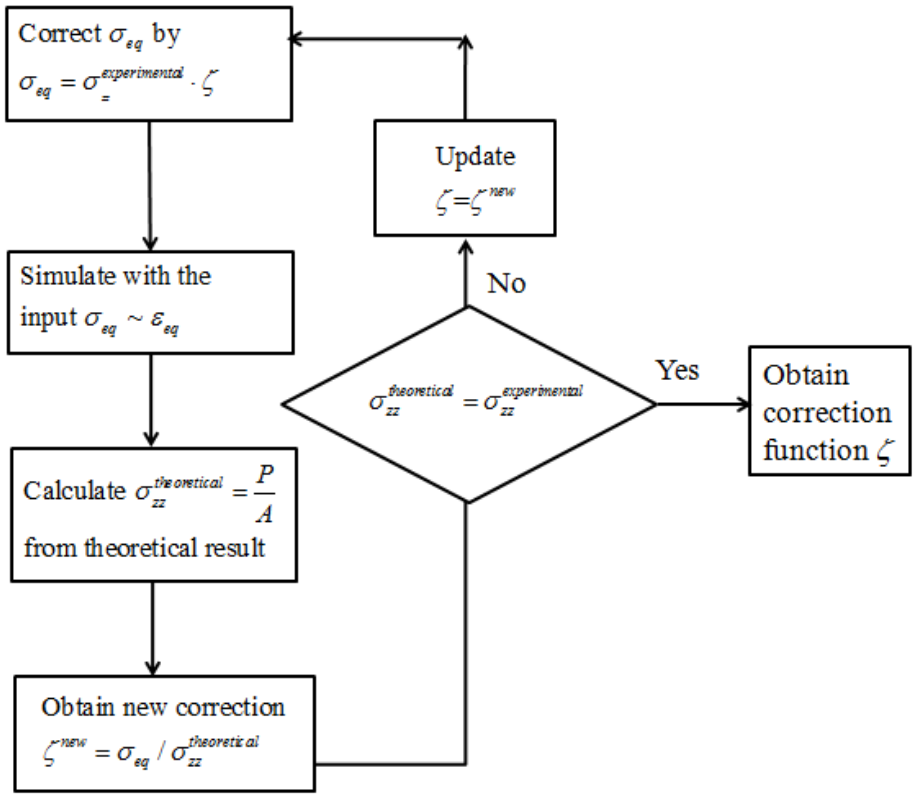


Figure 2.15. Flow chart of the self-consistent true stress correction method.

Since this method is self-consistent in terms of its capability to reproduce the experimental measurement and the accuracy is not limited to specific materials, this method is generally able to be applied to all materials once the accurate true stress in the axial direction can be obtained.

2.7 Correction Functions for Three Pb-free Solder Alloys

In this section, the self-consistent true stress correction method is applied on the three Pb-free solder materials, namely recrystallized pure tin (Sn), furnace-cooled SAC (tin/silver/copper alloy) and water-quench SAC, to obtain the correction functions by using the experimental data as shown in Figure 2.8. The same geometry (Figure 2.11) used in experiments is adopted in the finite element analysis. The finite element model has approximately 25000 eight-node brick elements (C3D8) and the mesh convergence has been ensured.

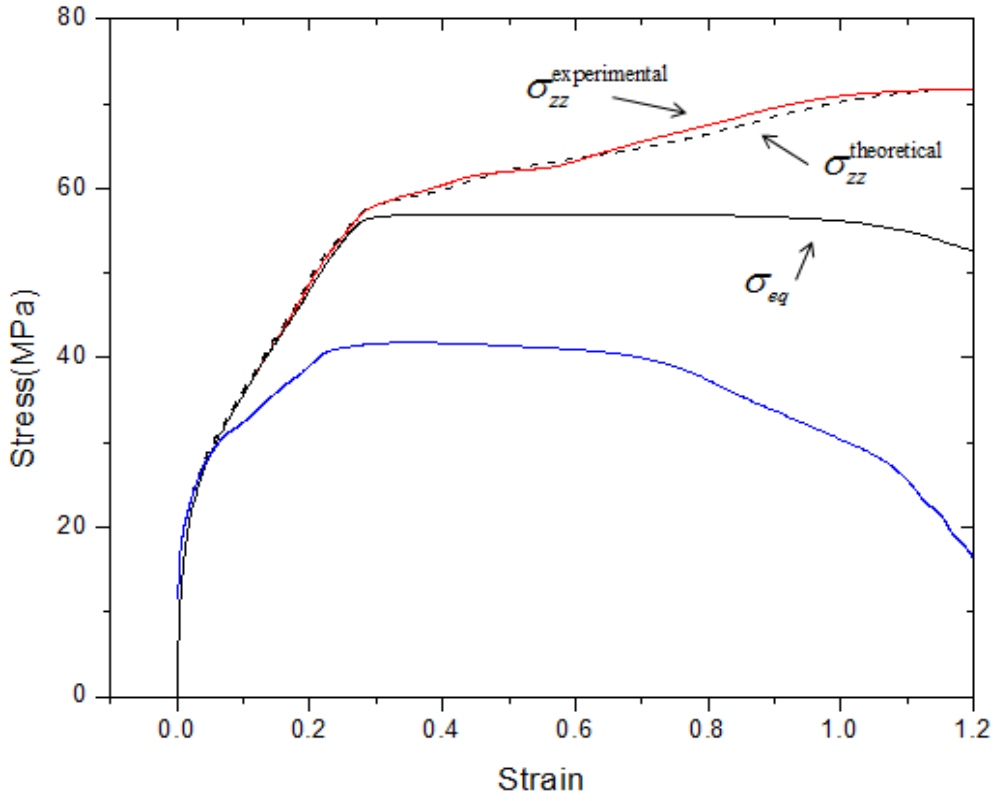


Figure. 2.16. Stress correction for pure Sn at strain rate of 10/s

An example is to deal with the experimental engineering stress/strain data of pure Sn to obtain the accurately corrected stress, based on this method. Figure 2.16 re-plots the stress/strain relation for pure Sn under strain rate 10/*s*. It shows that using the correction coefficient,

$$\zeta = -0.0479(\varepsilon_{eq}^{p})^2 - 0.1607\varepsilon_{eq}^{p} + 1.0702 \tag{2.11}$$

The experimentally measured axial stress $\sigma_{zz}^{\text{experimental}}$ is consistent with the calculated axial stress $\sigma_{zz}^{\text{theoretical}}$. Therefore, the corrected equivalent true stress $\sigma_{eq}$ should be used in the theoretical analysis. It is also noticed that this correction function is quite different from what was developed by Choung and Cho [47]. Now with the accuracy of this self-consistent method being shown with this example, the effect of strain rate on the correction function $\zeta$ is investigated.

As one can see from in Figure 2.8, solder materials are strain rate dependant [1, 9, 50]. Thus the correction function $\zeta$ should depend on both equivalent plastic strain $\varepsilon_{eq}^{p}$ and strain rate $\dot{\varepsilon}$, i.e., $\zeta = \zeta\left(\varepsilon_{eq}^{p}, \dot{\varepsilon}\right)$. Figure 2.17 shows the relation of the correction function $\zeta$ and equivalent plastic strain $\varepsilon_{eq}^{p}$ at different strain rate $\dot{\varepsilon}$ for the three solder materials. For the sake of clearness of the presentation, Figure 2.17 only shows the correction function $\zeta$ for four strain rates, namely, $\dot{\varepsilon}$ = 0.1/s, 1/s, 10/s and 30/s, although the correction function $\zeta$ for other strain rates are also studied. The plots of correction functions covering all strain rates in our test can be found in Appendix B.

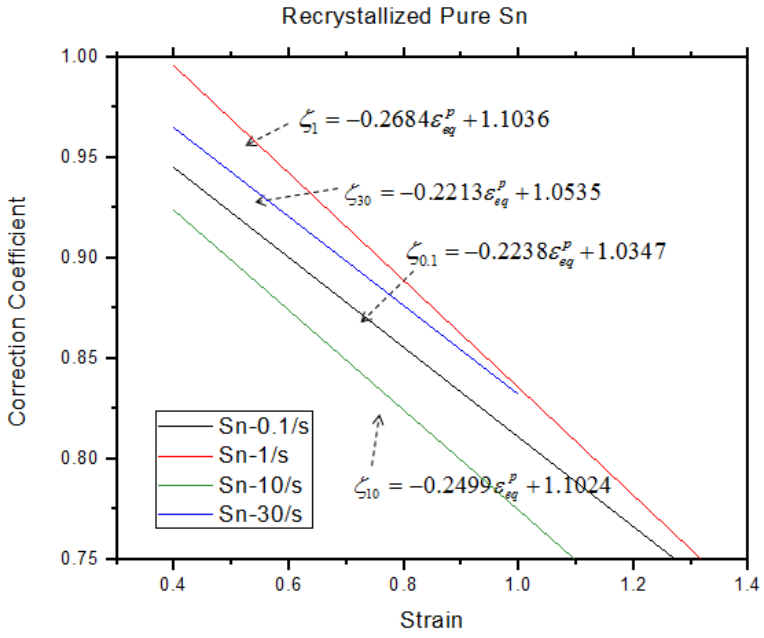


Figure 2.17 (a) Correction functions of pure Sn.

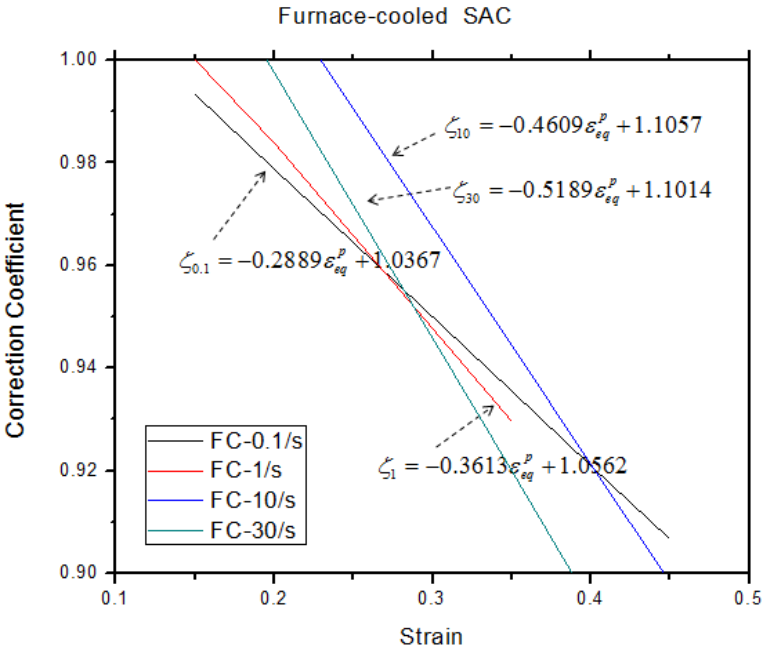


Figure 2.17 (b) Correction functions of Furnace-cooled SAC.

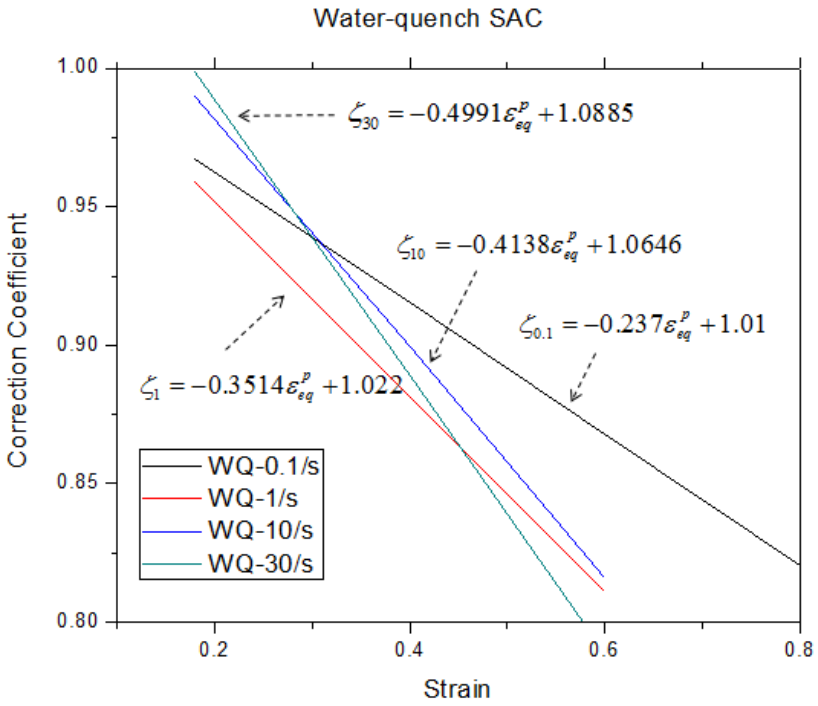


Figure 2.17 (c) Correction functions of Water-quench SAC.

Here linear relation between $\zeta$ and $\varepsilon_{eq}^{p}$ has been used, i.e., $\zeta = a\varepsilon_{eq}^{p} + b$. It is found that the pre-factor or slope $a$ depends on the strain rate $\dot{\varepsilon}$, while the intercept $b$ does not show strong dependence on the strain rate $\dot{\varepsilon}$. Figure 2.18 shows the relations between the pre-factor $a$ and the strain rate, which provides a means to get a functional expression for $a(\dot{\varepsilon})$. Eventually, the correction functions for the three solder materials are obtained as

$$\zeta_{Sn}\left(\varepsilon_{eq}^{p}, \dot{\varepsilon}\right) = \left[0.004 \cdot \log\left(\dot{\varepsilon}\right) - 0.235\right]\varepsilon_{eq}^{p} + 1.051 \tag{2.12}$$

$$\zeta_{FC-SAC}\left(\varepsilon_{eq}^{p}, \dot{\varepsilon}\right) = \left[-0.019 \cdot \log\left(\dot{\varepsilon}\right) - 0.440\right]\varepsilon_{eq}^{p} + 1.052 \tag{2.13}$$

$$\zeta_{WQ-SAC}\left(\varepsilon_{eq}^{p}, \dot{\varepsilon}\right) = \left[-0.045 \cdot \log\left(\dot{\varepsilon}\right) - 0.366\right]\varepsilon_{eq}^{p} + 1.02 \tag{2.14}$$

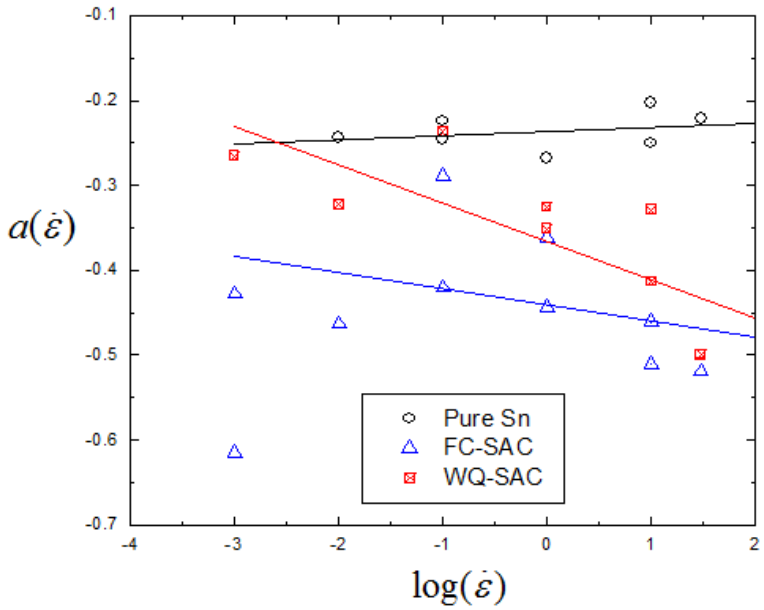


Figure 2.18. Linear relations between the pre-factor *a* and strain rate.

One can find from Eq. (2.12) or more clearly from Fig. 2.18, the correction function of pure Sn does not strongly depends on the strain rate $\dot{\varepsilon}$, compared with the other two solder materials. The reason is that pure Sn is very ductile, even at high strain rate up to 30/s. Therefore, pure Sn continues to neck uniformly and does not show strong strain rate dependence. The stronger strain rate dependence in water quenched SAC is most likely caused by the greater strain hardening that occurs as a result of the fine dispersion of spherical $Ag_3Sn$ precipitates which act as barriers to dislocation motion. In the case of furnace cooled SAC, the fractography shows that the large precipitates, especially $Ag_3Sn$, dominate the fracture process. The strain-to-failure (ductility) for furnace cooled SAC is less than that for water quenched SAC at all strain rates. The large precipitates make the furnace cooled SAC to fracture quickly without greatly affecting flow behavior. This explains that the furnace cooled SAC correction

factor has weaker strain rate dependence. Since the weak dependence on the strain rate $\dot{\varepsilon}$ of correction function $\zeta$ for pure Sn, a unified correction function $z$ can be used, i.e.,

$$\zeta_{Sn}\left(\varepsilon_{eq}^{p}\right) = -0.235\varepsilon_{eq}^{p} + 1.051 \tag{2.15}$$

2.8 Strain Rate Effect of Longer Specimen

2.8.1 Double Necking Phenomenon

Based on the study on the specimen geometry in section 2.3, all the above experiments and analyses are conducted on dog-bones with 10-mm gage length. In this section, an interesting phenomenon is found in the tensile tests of ASTM specimen (25 mm gage length), but not found in the 10-mm specimen tensile test.

Examination of the stress-strain curves for both 10-mm and 25-mm geometries shows that while $\sigma_{UTS}$ and strain-to-failure are indeed similar, the curves for the 25-mm dog-bones (ASTM E-8M) exhibit two distinct “peaks” in the stress/strain curves, as shown in Fig. 2.19. Oscillations in stress-strain curve are due to reflected elastic waves.

By using the high-speed video analysis, it is found that the peaks of the stress/strain curves correspond to two separate necks forming in the gage section. Thus, it is called double-necking phenomenon. Fig. 2.20a shows the analysis of one of the tensile tests. Figure 2.20b lists the still images from selected points in the entire test sequence, which illustrates the progress of specimen deformation. The phenomenon of multiple necking at high strain rates has been observed in other materials, such as aluminum and copper [51, 52]. The dynamics of plastic

instability are quite complicated and are not treated here. The smaller gage section, on the other hand, only exhibits one peak in the curve.

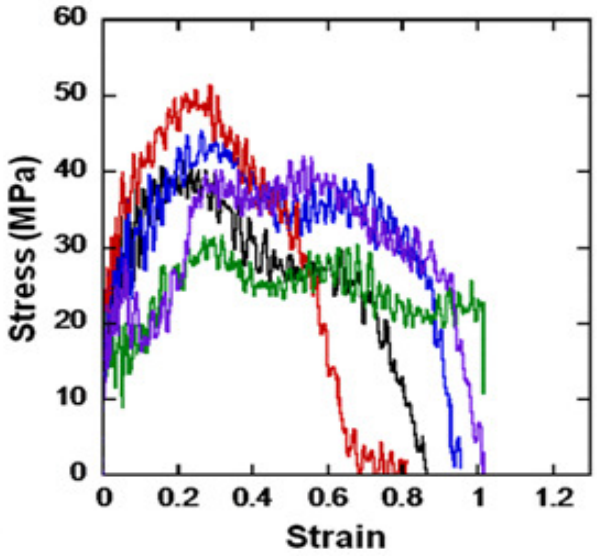


Figure 2.19. Stress-strain curves of ASTM E-8M specimens under tension at a strain rate of 10/s, exhibiting two distinct peaks. (Courtesy of K. Yazzie)

Within the population of these curves, two experiments have somewhat higher ultimate tensile strength and lower ductility, which are indicated by bold line thicknesses in Fig. 2.21a. The gage sections are indicated by white dotted lines in Fig. 2.21b, and videos of these experiments indicate a fair amount of bulging in the gage section, especially for specimens 5 and 6 which correspond to the bold curves in Fig. 2.21a. The reasons for bulging in some specimens are likely related to evolution of inhomogeneous deformation, perhaps due to individual grain orientation and/or defects. A more detailed study is needed to understand this behavior.

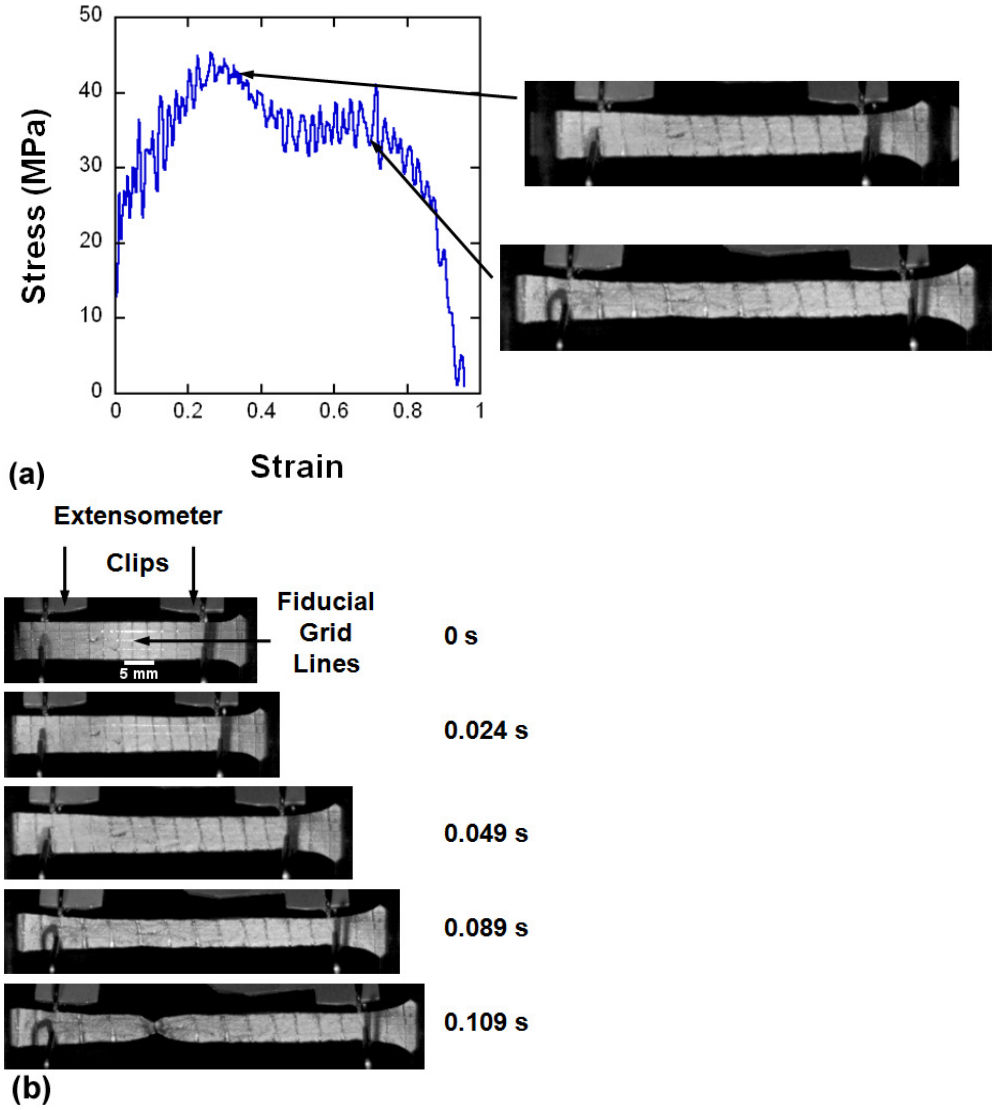


Figure 2.20. High speed video analysis of dog-bone tensile tests. (a) The "peaks" correspond to formation of two separate necks in the gage section. (b) Progress of specimen deformation. (Courtesy of K. Yazzie)

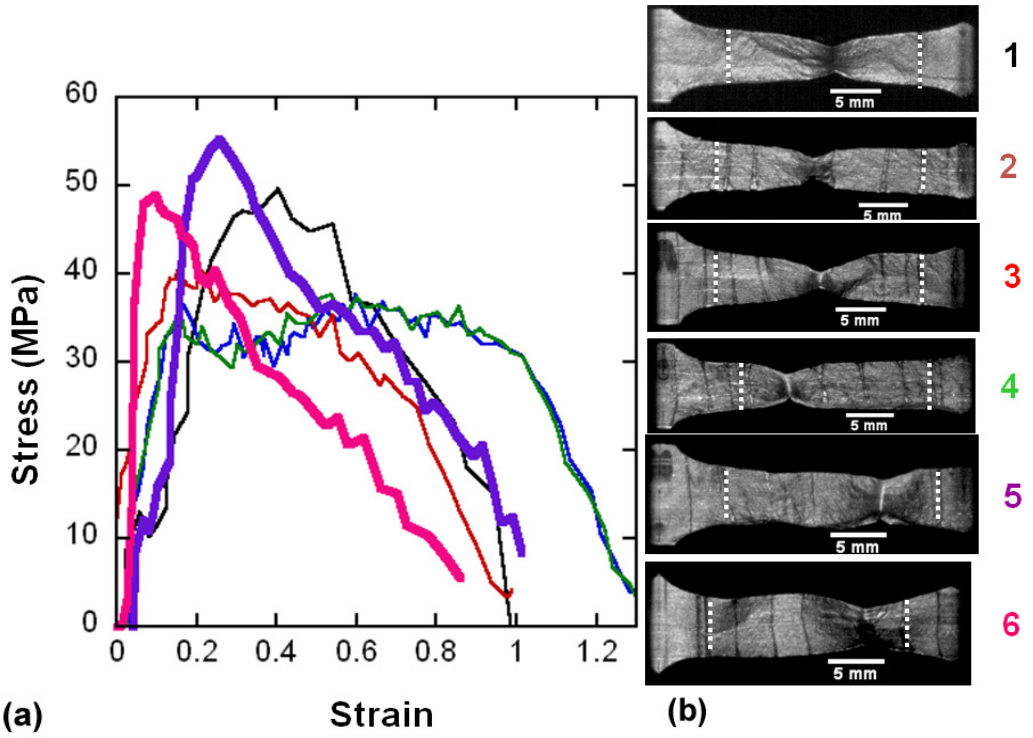


Figure 2.21. Stress-strain curves of 10 mm gage length specimens tested at a strain rate of 10/s (a) Stress/strain curves. (b) High speed video analysis. (Courtesy of K. Yazzie)

2.8.2 Finite Element Analysis on Double Necking

In this section a series of FEA simulations are conducted to study the deformation of dogbones with various gage length at various strain rates. The objective of the theoretical study is to qualitatively explain the experimentally observed behavior, as influenced by gage length and applied strain rate. This analysis is carried out via ABAQUS/Explicit [41]. To accurately investigate the geometric effects on the double-necking, three-dimensional elements are used. In order to ensure convergence of the explicit analysis, a very fine mesh and time increment were used. After the studies of mesh sensitivity, element C3D8R (continuum three-dimensional 8-node solid element with reduced integration

scheme) is chosen. Depending on the geometry of our model system, the total number of elements ranged from 6,000 to 28,000.

The following two empirical criteria are used to simulate the necking phenomena: (1) local maximal principal plastic strain exceeding 50%, or (2) local maximal principal strain rate larger than 10/s. These are relatively arbitrary criteria, which give a good comparison with the experimental observations. And experimental measurements are being conducted to obtain more accurate values of the local plastic strain and strain rate. The rate-dependent strain-strain relation are based on Long et al.'s experiments [53], with Young's modulus of 46 GPa, Poisson's ratio of 0.3, and density 7.6 g/cm$^3$. Our experimental measurements show that both the strain and displacement in fillet region are relatively small compared with the strain in the gage section. Thus, a 3D rectangular geometry, representing the gage section only, is modeled for the simulation.

Figure 2.22a shows the simulation results of the ASTM E-8M specimen. A velocity of 500 mm/s is imposed at one end while keeping the other end fixed. The contour plot of the maximal principal plastic strain on the deformed bar, at $t$ = 56 ms, clearly shows the double-necking close to the two ends of the bar. Figure 2.22b shows that the majority of the specimen has reached 50% plastic strain, so plastic strain alone cannot explain the double-necking phenomenon. This is reasonable since under low strain rates under uniaxial tension, double-necking does not take place. Figure 2.22c shows the contour of the maximal principal strain rate at the same time $t$ = 56 ms. Here, the localized strain rate reaches the

necking criterion (10/s) only at the two double-necking sites near two ends. Since the maximal localized strain rate only appears at the double-necking sites, it seems that the localized strain rate is a better indicator of where necking will take place.

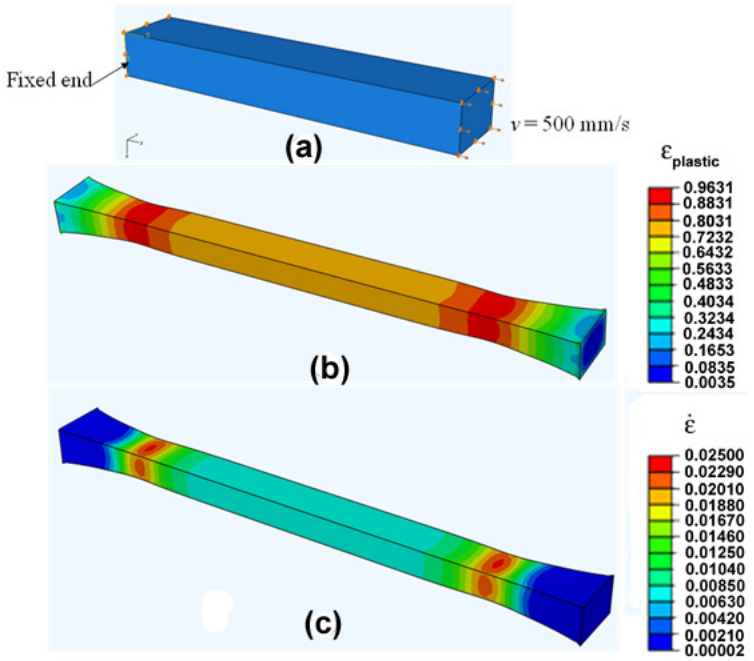


Figure 2.22. Finite element analysis of ASTM E-8M specimen subjected to 500 mm/s velocity load. (a) Boundary condition (b) Contour of plastic strain at time $t$ = 56 ms,(c) Contour of strain rate at time $t$ = 56 ms.

In addition to specimen geometry, the effect of strain rate is also investigated. A series of simulations are conducted by varying the applied displacement rates, from 100 mm/s to 400 mm/s. Table 3 summaries the relations between double-necking and maximal principal plastic strain and localized strain rate. It is interesting to note that double necking only takes place above a critical strain rate of about 10/s, which correlates well with our experimental results. Based on these facts and data, the conclusion is that the localized plastic strain,

closely related to the displacement rate, plays an important role on the potential sites for necking.

Table 3.

Relation of the Double-Necking with Maximal Plastic Strain and Localized Strain Rate for ASTM E-8M Specimen.

| Velocity (mm/s) | Maximal principal plastic strain | Maximal localized strain rate (/s) | Double-necking | Time when necking firstly visible (ms) |
|---|---|---|---|---|
| 100 | 50.7% | 2.8 | No | 170 |
| 200 | 51.6% | 6.0 | No | 92.5 |
| 300 | 57.1% | 10.3 | Yes | 67.5 |
| 400 | 57.8% | 11.1 | Yes | 53.1 |
| 500 | 55.6% | 12.8 | Yes | 41.4 |

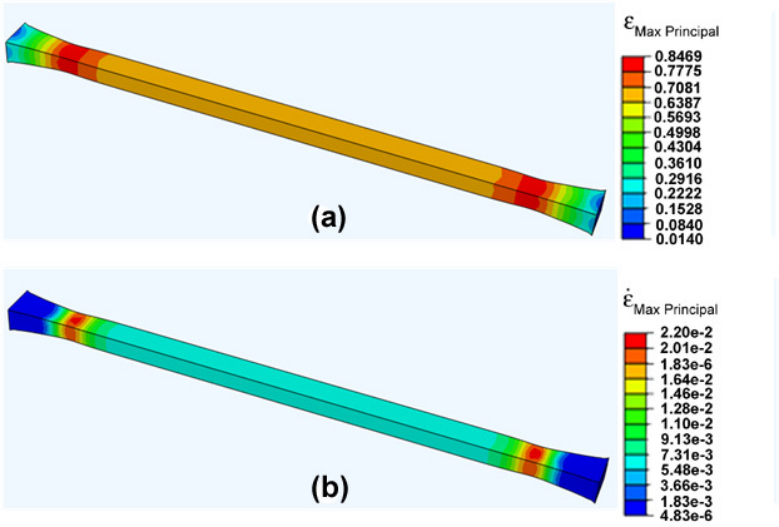


Figure 2.23. FEA contours of a 50-mm-long bar subjected to 700 mm/s velocity load. (a) Contour of plastic strain at time $t$ = 70 ms, (b) Contour of strain rate at time $t$ = 70 ms.

The length of the gage section is also varied to quantify the effect of geometry on double necking. Figure 2.23 shows double-necking at $t$ = 70 ms in a

50-mm-long bar subjected to a displacement rate of 700 mm/s. The maximal principal plastic strain reaches the necking criterion globally throughout the gage section, Figure 2.23a, while the maximal principal strain rate criterion is met locally, as in Figure 2.23b. The same results are observed in the case of the 32-mm gage section, Figure 2.22 and Table 3.

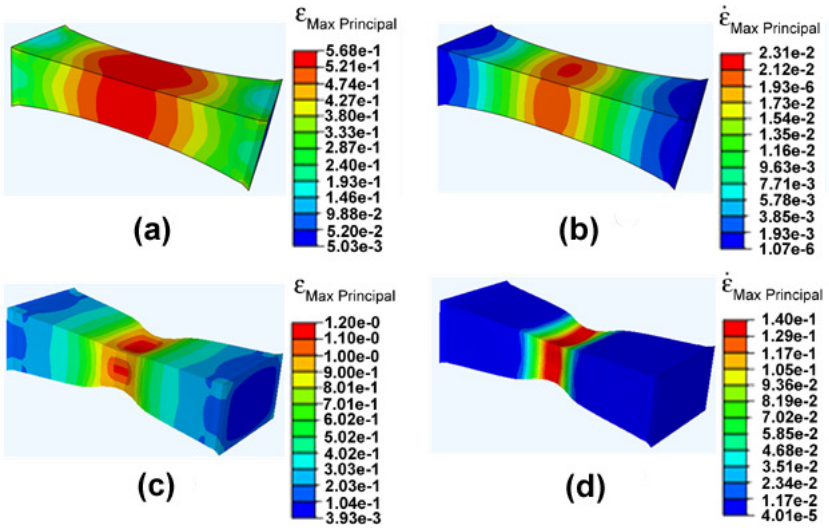


Figure 2.24. FEA contours of a 10-mm-long bar subjected to 150 mm/s velocity load. (a) plastic strain at time $t$ = 35 ms (b) strain rate at time $t$ = 35 ms. (c) plastic strain at time $t$ = 45 ms (d) strain rate at time $t$ = 45 ms.

For a bar with shorter gage section, i.e., $L$ = 10 mm, subject to 150 mm/s velocity load, double necking is not observed, Figure 2.24. Because of the short gage section, the maximal principal strain rate is not localized at either of the two different sites for potential double-necking, Fig. 2.24b. Eventually, at time $t$ = 45 ms, a single neck takes place, Figures 2.24c and 2.24d. These two results indicate that the gage section also plays an important role. Double-necking only occurs for the specimens with longer gage section. The critical length of the gage section

may depend on various parameters, such as constitutive behavior of the material and displacement rate.

## 2.9 Summary

In this chapter, we first investigate and try to define the strain rate range for the mechanical shock loading, which sits between quasi-static and dynamic impact range. To be precise, the range is somewhere between $10^{-1}$/s and $10^{2}$/s.

To determine proper specimen geometry, finite element modeling and analysis are conducted, and stress/strain distributions within the gage section are examined. The dogbone specimen with 10-mm gage length produces a homogeneous strain distribution, similar to that for the ASTM E-8M specimen geometry (25 mm gage length). The strain rate control is also studied, and the smaller gage length enabled us to obtain a higher strain rate for a given applied displacement rate. Thus, 10 mm specimen is more suitable for obtaining reliable and accurate constitutive data for FEM reliability models.

Then the stress/strain relation of three Pb-free solder alloys, namely recrystallized pure Sn, furnace-cooled SAC (tin-silver-copper alloy) and water-quench SAC are experimentally measured under the mechanical shock condition. High-speed video coupled with fiducial markings on the specimen surface is used to correlate the local deformation mechanisms with the measured stress–strain behavior. This technique is quite valuable in trying to understand the behavior of solder alloys at intermediate strain rates. The applied strain rate ranges from 0.001/s to 30/s, which represents regime from quasi-static to mechanical shock.

The higher strain rate will make material stiffer (higher yield stress and ultimate tensile strength).

A high-accuracy self-consistent approach is developed to correct the experimentally measured axial stress for post-necking stage in uniaxial tension tests. The accuracy of this methodology is guaranteed by using the criterion of the self-consistence between the experimentally measured and the calculated axial stress from finite element analysis. The correction functions and accurate equivalent true stress/strain relations of the three Pb-free solders are obtained, and a typical correction function is a function of plastic strain and strain rate. This approach can be applied to any material in any geometry shape (either round or rectangular), as long as the engineering stress/strain relation is accurately measured.

A double-necking phenomenon is observed in the uniaxial tension test on an ASTM E-8M specimen with a 25-mm gage length, which is not observed on other shorter sample (i.e. 10-mm gage length). Finite element model is built for the dog-bone uniaxial tension test with varying gage length and loading strain rate. FEM results of the dynamic behavior of the longer specimens correlate very well with the experimental observations. In particular the trends observed in experiments could be rationalized based on the FEM modeling results.

The mechanical shock stress/strain relation of bulk solder materials obtained in this chapter will be utilized in the following analysis on solder joints.

# CHAPTER 3

# NUMERICAL EVALUATION OF MICRO-COMPRESSION TESTS FOR DETERMINING ACCURATE CONSTITUTIVE RELATIONS OF INTERMETALLICS IN SOLDER JOINTS

## 3.1 Introduction

Most Pb-free solders are Sn-rich, with slight alloying additions of Ag, Cu, or both Ag and Cu. The important microstructural features of a typical Sn-rich joint, with composition of $Sn_{3.9}Ag_{0.7}Cu$, are shown in Fig. 3.1. The solder microstructure consists of Sn dendrites decorated by a eutectic mixture of $Ag_3Sn$ and $Cu_6Sn_5$ intermetallic particles. The solder microstructure, as controlled by cooling rate, inherently controls the mechanical response of the joint. In addition, a $Cu_6Sn_5$ intermetallic layer grows from the reaction between the Sn-rich liquid (during melting) and the Cu substrate [54-56]. The nature of the interfacial products formed between solder and substrate greatly influences the thermo-mechanical behavior of the solder joint [12, 13, 57-59]. In particular, the mechanical behavior of solder joints is very sensitive to the thickness and morphology of the intermetallic layer. A relatively thin layer of intermetallic compounds may be beneficial in enhancing mechanical and chemical bond between Sn-rich solder and Cu substrate [60, 61]. However, when the intermetallic layer is relatively thick, it often acts as a crack initiation site, leading to poor toughness of the joint, because of its brittle nature [58, 59, 62, 63].

Thus, a fundamental understanding of the elastic and plastic properties of Cu-Sn intermetallics is very important. Some researchers fabricated bulk intermetallics by casting and annealing processes, and tested mechanical properties of the bulk material by conventional method [25, 64, 65]. However, the intermetallic compounds in the solder joint and that in bulk may differ significantly in grain size, defects, and crystallographic orientation, which lead to different material properties. In fact, preliminary studies on Young's modulus of Cu–Sn intermetallics show a scattered results [25, 64-66]. Therefore, the mechanical properties of micron-scale intermetallics in the solder joint are the target of interest.

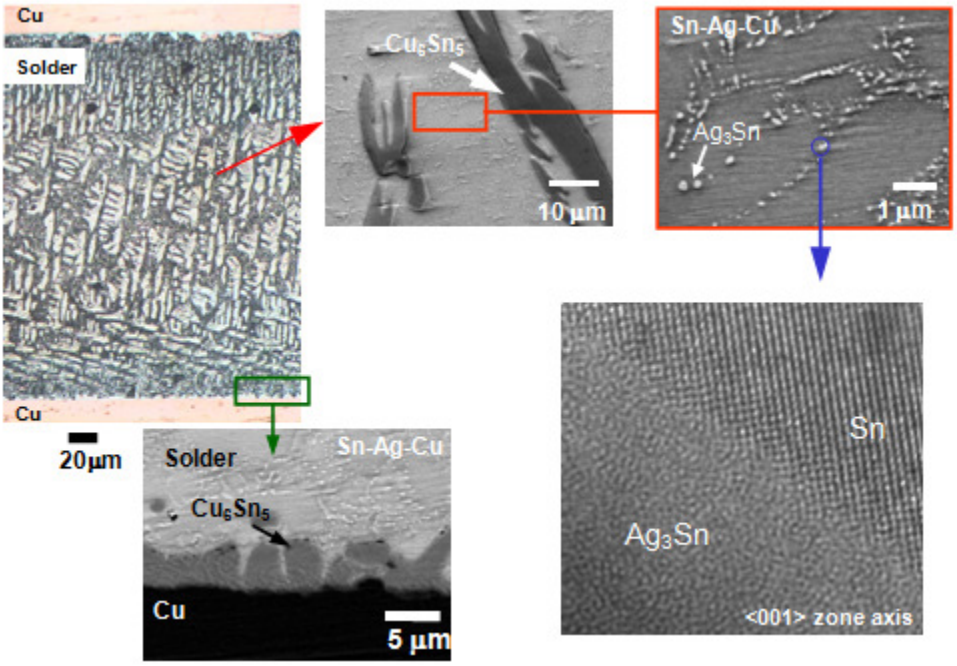


Figure 3.1. Microstructure of a $Sn_{3.9}Ag_{0.7}Cu$ joint (Courtesy of N. Chawla).

In this chapter, a novel method, namely micro-compression or micropillar compression, is introduced to probe the mechanical properties of intermetallics.

We execute a systematic study via finite element analysis (FEA) to evaluate the accuracy of micro-compression test from some aspects. We propose adjustments to calculate stress and strain with a good correlation with experimental measurements. Then the method is applied to obtain the mechanical properties of $Cu_6Sn_5$ by micro-compression test. Using the obtained properties, a simple brittle fracture model is built via ABAQUS/Explicit.

The structure of Chapter 3 is constructed as following. Section 3.2 introduces the micropillar compression test. The strain measurement of pillar is discussed in Section 3.3. The deformations of indenter, pillar and substrate are coupled together, so the purpose of the study in Section 3.3 is to eliminate the influences of substrate and indenter. In Section 3.4, we considered factors that affect the pillar stress measurement. The shape of pillar will cause the non-uniform stress field, which will make the stress calculation more difficult. Based on this, the taper angle and aspect ratio effects are evaluated in Section 3.4. A brittle fracture model of $Cu_6Sn_5$ is built using the mechanical properties obtained by micro-compression test.

## 3.2 Micropillar Compression Test

The importance of having accurate constitutive relations to understand the mechanism of how materials deform cannot be overemphasized. Its indispensability is further strengthened for materials featured with micro-structures. For instance, the mechanical behavior of Pb-free solder and intermetallic materials that is extremely important because solder joints must

retain their mechanical integrity under conditions of mechanical shock, vibration fatigue, thermal fatigue, and creep, is primarily determined by their micro-structures and other alloying compositions, including Ag, Cu, or both Ag, Cu, and $Sn_{3.9}Ag_{0.7}Cu$ (SAC). To study the micro-structure based constitutive relations, the conventional experimental technique, such as uniaxial tension is invalid; and therefore, may different techniques have been developed.

As a result, techniques that test material hardness by indenting a material using various size and shape of indenters have been developed. Current nano-indentation has achieved sub-nanometer displacement resolution and 1 nano-newton force resolution, which makes this technique widely used to determine the mechanical properties [67]. Despite of the popularity of the indentation test, it still has some intrinsic shortcomings, such as strain hardening (pill-up), annealing (sink-in), and surface finish. Moreover, indentation test involves complex stress/strain field underneath the indenter depending on the specific tip geometry, such that the indirect or complicated methods must be used to extract constitutive relations [67].

Recently, micro-compression method is developed to measure the material stress/strain relation. In micro-compression experiment, a flattened indenter is used to compress micro-pillars (Fig. 3.2a), Micro-pillars are machined by milling materials of interest using focused ion beam (FIB) (Fig. 3.2b) with diameters ranging from 200 nanometers to a few microns [68] within a single phase of constituent. Jiang and Chawla [12] investigate the fracture stress and fracture

mechanism of $Cu_6Sn_5$ by the micro-compression test. Liu et al. [69] study the crystal plasticity at submicron-to-nanometer scales by simulations of micro-compression on pillars. Akarapu et al. [70] investigate the heterogeneous deformation and dislocation dynamics in single crystal micropillars under compression. Byer et al. [71] conduct micro-compression experiments of single-crystal magnesium micro-pillars fabricated by focused ion beam (FIB) milling. El-Awady et al. [72] analyze trapping and escape of dislocations in micro-crystal pillars. Kaufmann et al. [73] study the size dependent mechanical behavior of tantalum by compression test of micropillars.

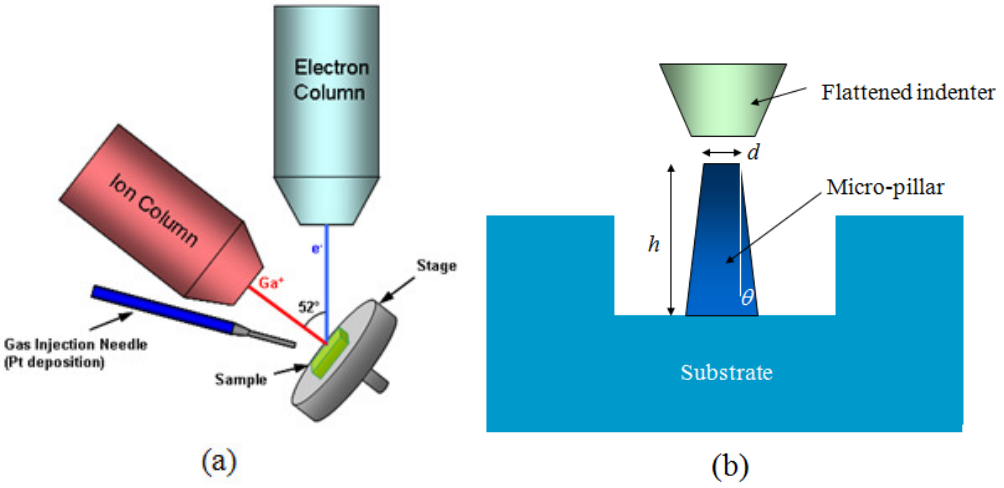


Figure 3.2. (a) Schematic of focused ion beam (FIB); (b) Schematic of the nano-indentation and micro-compression test (Courtesy of N. Chawla).

Figures 3.3a & 3.3b show scanning electron microscopy images of micro-pillars. Compared with the micro-indentation test, micro-compression is believed to have an obvious advantage of uniform stress/strain field under uniaxial compression. There may, however, be some experimental variables to affect the accurate measurements of strain and stress (as illustrated in Fig. 3.2b). These

variables include the aspect ratio $\alpha$ (the ratio of height $h$ and diameter $d$ of the pillar), size of substrate, taper angle $\theta (> 0)$ (the angle between the tangent of wall and axis of the pillar), fillet angle, the misalignment between the pillar axis and the compression direction, and materials of the substrate.

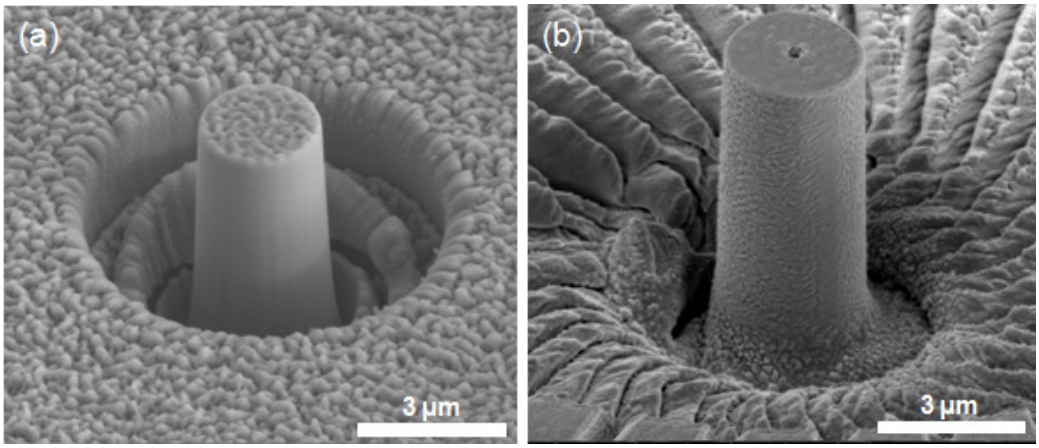


Figure 3.3. Scanning electron microscopy (SEM) image of a micro-pillar on a single grain of SAC alloy, with a taper angle of (a) $4^{o}$, (b) $0^{o}$ (Courtesy of L. Jiang and N. Chawla)

Some of these variables can be intuitively understood. For example, for a compliant substrate, the pillar will sink in upon compression load and majority of the deformation is borne by the substrate instead of the pillar, which leads to inaccurate measurement of pillar deformation. This sink-in effect maybe enlarged for pillars with large aspect ratio and suppressed for pillars with large taper angle. The large aspect ratio may also lead to buckling of the pillars upon compression. This intuitive argument indicates that these factors are coupled together to influence the accuracy of the experimental measurement. Zhang et al.[74] used finite element method to study some of these effects, including aspect ratio, fillet

angle, taper angle and misalignment for a pillar on a very thin substrate sitting on a rigid base.

## 3.3 Measurement of Pillar Strain

In this section, we conducted a systematic and thorough study on the measurement of pillar strain in the micro-compression test by finite element analysis.

### 3.3.1 Finite Element Model

We use axisymmetric geometry to model the micro-compression test, as shown in Fig. 3.4a. The indenter with radius $r_{indenter}$ is included though its deformation maybe very small, and modeled as elastic materials. $r_{pillar}$ is the top radius of the pillar; $\theta$ is the taper angle; and $h$ is the height of the pillar. The dimension of the substrate is $L \times L$. Figure 3.4a is not scaled since the dimension of the substrate is usually two orders greater than that of the pillar. The pillar and substrate are the same materials and can be elastic or plastic. The prescribed displacement boundary condition $v = 0$ is applied at bottom of the substrate to model the rigid base underneath the substrate; and the axisymmetric boundary condition $u = 0$ is applied along the symmetric axis. Here $u$ and $v$ represent the displacements along $x$ and $y$ directions, respectively. The prescribed pressure load $p$ is applied on top of the indenter, thus the axial compressive force is $f = \pi r_{indenter}^2 p$. The finite element analysis is conducted via the commercial finite element package ABAQUS/Standard [75]. Axisymmetric 4-node continuum elements (CAX4) and 3-node elements (CAX3) are chosen for discretization.

Mesh sensitivity is studied by reaching a convergent load/displacement curve of the pillar region. A typical convergent mesh with about 200,000 elements is shown in Fig. 3.4b, with the inset of the pillar region.

The range of geometry parameters used in the following analyses are listed: $r_{indenter} = 1\mu m$ , $r_{top} = 0.5\mu m$ , $\theta = 0 \sim 5^o$ , $\alpha = 2 \sim 4$ , $L = 10 \sim 70\mu m$ . The elastic materials used have Poisson's ratio 0.3 and Young's modulus ranging from 50GPa to 400GPa. And the plastic material used is shown in Figure 3.5.

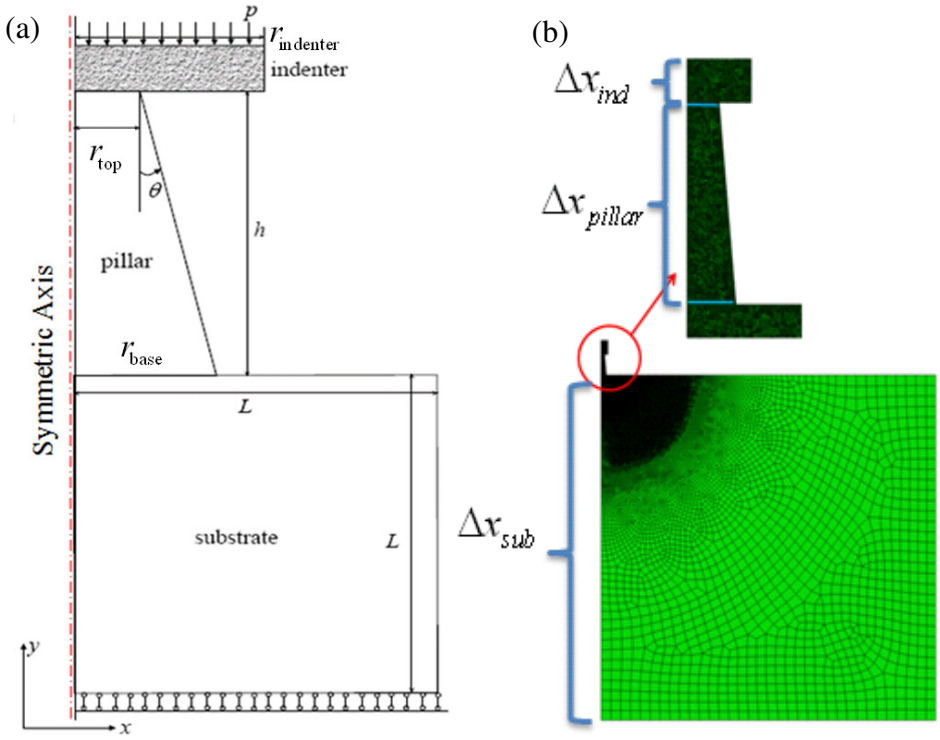


Figure 3.4. (a) Schematic of axisymmetic model of the micro-pillar; (b) Geometry and mesh of finite element model.

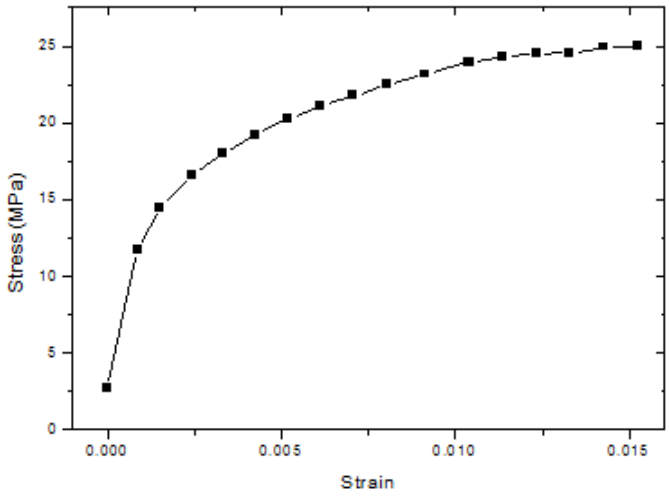


Figure 3.5 Plastic Constitutive relation used in the parametric study.

3.3.2 Indentation Depth and Sneddon's Formula

Due to the mechanism of micro-compression test, the pillar strain cannot be directly measured. The load is applied on the top of the indenter (Figure 3.4a), and the measurable variable is the indentation depth, i.e.. the displacement of the top surface of indenter. The indentation depth is actually the total displacement of the system. The relation between indentation depth and pillar deformation is

$$\Delta x_{total} = \Delta x_{ind} + \Delta x_{pillar} + \Delta x_{sub} \tag{3.1}$$

where, $\Delta x_{total}$ is indentation depth, $\Delta x_{ind}$ is the deformation of indenter itself, $\Delta x_{pillar}$ is the pillar deformation, and $\Delta x_{sub}$ is the substrate deformation.

The pillar deformation $\Delta x_{pillar}$ is the variable of interest, and the deformations of indenter and substrate are considered to be “noises”. To quantify these noises, we conducted finite element simulations with two materials: one elastic material and one plastic material. The finite element model is discussed in Section 3.3.1.

We define the deformation ratios by

$$pillar\% = \frac{\Delta x_{pillar}}{\Delta x_{total}}$$
$$substrate\% = \frac{\Delta x_{sub}}{\Delta x_{total}} \quad (3.2)$$
$$indenter\% = \frac{\Delta x_{ind}}{\Delta x_{total}}$$

Figure 3.6a & 3.6b show the deformation ratios for elastic and plastic materials, respectively. For elastic material, the pillar deformation is around 80% of the indentation depth, the substrate deformation ratio is close to 20%, and the indenter deformation ratio is less than 1%. For the plastic material, deformation ratios are no longer constants, and they change along with the applied load changes. The indentation deformation ratio is still very small, less than 1%. The pillar's deformation ratio is over 80% and becomes larger and larger when the applied load increases, while the substrate% decreases at the same time. The substrate's deformation is pretty large, compared to the indenter's deformation.

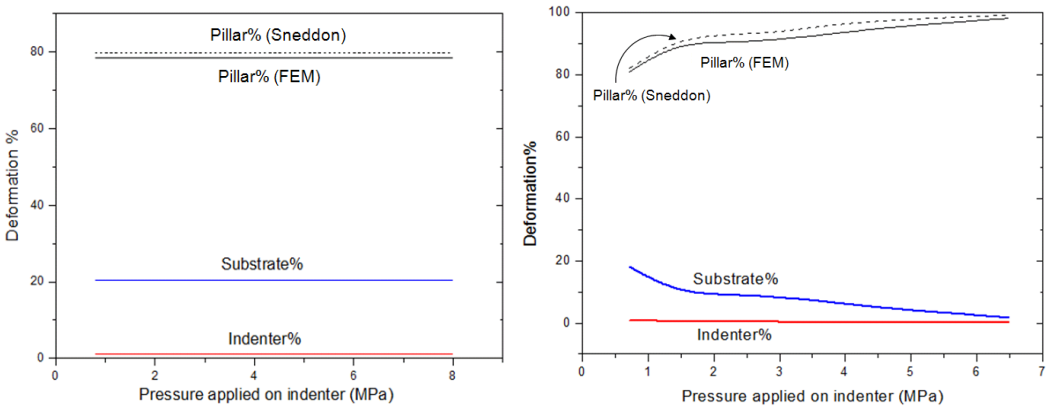


(a) (b)

Figure 3.6. The deformation percentage of pillar/substrate/indenter over the total deformation of (a) elastic material and (b) plastic material

To accurately calculate the pillar deformation, the deformations of indenter and substrate must be eliminated from the total deformation. Sneddon [76] considered the punching effect of a cylindrical punch indenting into an elastic half space, and developed an analytical formula to calculate the compliance associated with the deformation of substrate material and the indenter.

$$C_{Sneddon} = \frac{(1-v^2)\sqrt{\pi}}{2E\sqrt{A_p}} \tag{3.3}$$

where, $C_{Sneddon}$ is the compliance of indenter (or substrate), $E, v$ are the Young's modulus and Poisson's ratio of indenter (or substrate), and $A_p$ is the contact area between pillar and indenter (or substrate). By known compliance, the deformation of indenter/substrate can be calculated by

$$\Delta x_{ind} = C_{ind} f,\ \Delta x_{sub} = C_{sub} f \tag{3.4}$$

where, $f = \pi r_{indenter}^2 p$ is the applied force on top of indenter, and $p$ is the pressure. Therefore, Eq.(3.1) can be rewrote as[12, 77, 78]

$$\Delta x_{pillar} = \Delta x_{total} - \frac{(1-v_{sub}^2)\cdot f}{2E_{sub}\cdot r_{base}} - \frac{(1-v_{ind}^2)\cdot f}{2E_{ind}\cdot r_{top}} \tag{3.5}$$

where, $r_{top}$ and $r_{base}$ are the radius of the top and base surface of pillar, respectively. A typical indenter used in the micro-compression test is made of diamond, which has Young's modulus 1,141GPa and Poisson's ratio 0.07 [79]. Normally the substrate is of the same material as the pillar.

3.3.3 Strain Error and Strain Error Ratio

The Eq. (3.5) explicitly includes two parts of corrections: substrate and indenter, and gives an estimated pillar deformation. The estimated pillar strain can be easily obtained by

$$\varepsilon_{pillar}^{Sneddon} = \frac{1}{h_{pillar}}\left( \Delta x_{total} - \frac{(1-v_{sub}^2)\cdot f}{2E_{sub}\cdot r_{base}} - \frac{(1-v_{ind}^2)\cdot f}{2E_{ind}\cdot r_{top}} \right) \tag{3.6}$$

To evaluate the accuracy of $\varepsilon_{pillar}^{Sneddon}$, we define two quantities, strain error,

$$e = \varepsilon_{pillar}^{Sneddon} - \varepsilon_{pillar}^{FEM} \tag{3.7}$$

and strain error ratio,

$$\eta = \frac{\varepsilon_{pillar}^{Sneddon} - \varepsilon_{pillar}^{FEM}}{\varepsilon_{pillar}^{FEM}} \tag{3.8}$$

where, $\varepsilon_{pillar}^{FEM}$ is the strain of pillar obtained from the FEM simulation results,

$$\varepsilon_{pillar}^{FEM} = \frac{u_{pillar}^{top} - u_{pillar}^{base}}{h_{pillar}} \tag{3.9}$$

Compared with the Sneddon's correction, we consider $\varepsilon_{pillar}^{FEM}$ is more accurate.

The strain error represents the absolute difference between Sneddon's strain and real pillar strain. The strain error ratio describes the corresponding relative difference. To get a brief idea of how large are the strain error and strain error ratio, we consider a cylindrical pillar on top of a substrate, subjecting to pressure form a diamond indenter. The height of the pillar is 3 micrometer, and the radius of it is 0.5 micrometer. The size of substrate is 50 micrometer by 50 micrometer. The detail of finite element analysis is discussed in section 2. We

tested four elastic materials with Young's modulus E=50, 100, 200 and 400GPa, which cover the range of conventional metals. Figure 3.7 shows that the strain error $e$ increases when applied pressure increases, and strain error ratio $\eta$ is a constant and irrelevant to the applied pressure due the constant property parameters of elastic material. The strain error ratio is larger for material with larger Young's modulus. When material getting stiffer, it's getting close to the diamond indenter. The indenter deformation will take more weight in the total indentation depth.

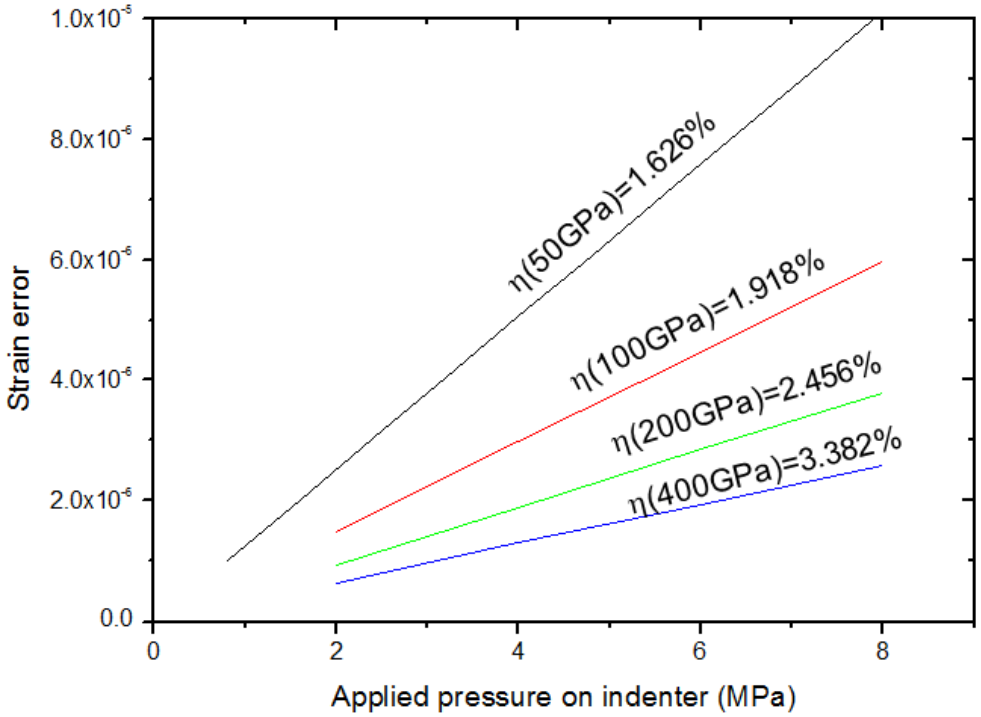


Figure 3.7. The strain error and strain error rate of a series of elastic materials.

3.3.4 Substrate Effect

Based on the previous analysis, the substrate deformation is the main "noise" to the measurement of pillar strain, and Sneddon's formula cannot completely compensate the substrate deformation. The ideal scenario that the substrate has vanishing size, i.e., pillar rests on top of a rigid base, which completely eliminate the sink-in effect and the strain measurement is more accurate. However, the mechanism of micro-machining the pillars (i.e., milling the substrate and generating the pillar) requires a certain thickness of the substrate.

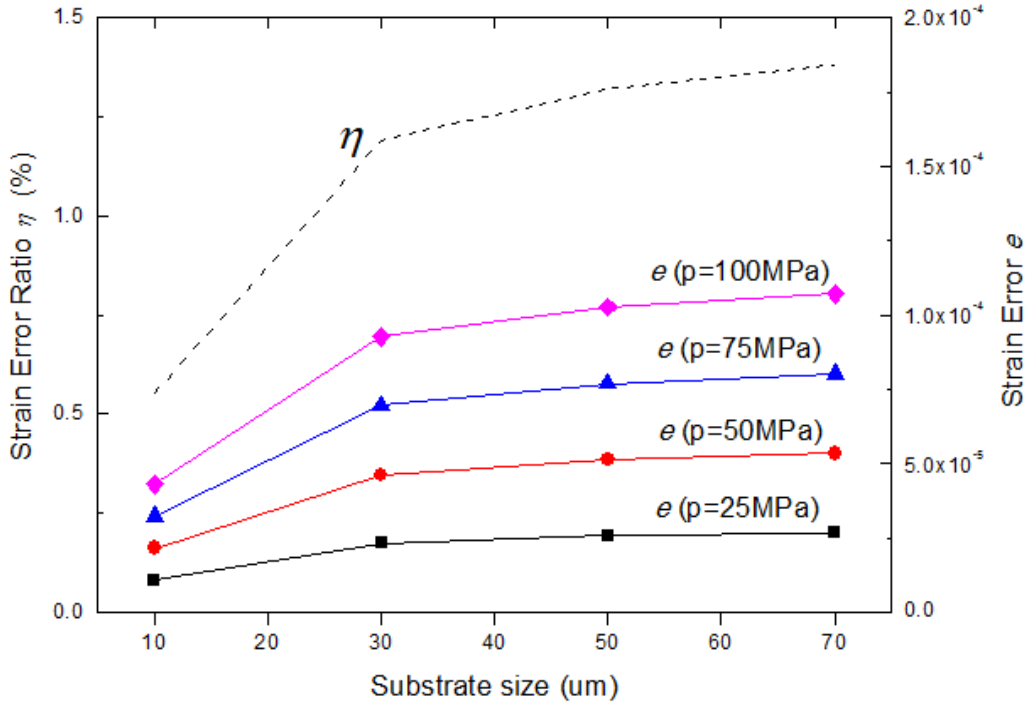


Figure 3.8 The substrate size effect of an elastic material (E=50GPa, v=0.3).

To quantify how the substrate size affects the strain measurement, we considered substrate effect by varying the size of it from 10umX10um to 70umX70um. The height of the pillar is 3 micrometer, and the radius of it is 0.5

micrometer. First, an elastic material is used, Young's modulus is 50GPa, and Poisson's ratio is 0.3. In Figure 3.8, the x-axis is the size of substrate L, the right y-axis is the strain error $e$, and the left y-axis is the strain error ratio $\eta$. The strain error goes up when the size of substrate increases, and it has a convergent trend when L > 50um. The strain error ratio, which is dash line in the plot, shows the similar trend. And the overall strain error ratio is less than 1.5%, even the substrate size is very large. Thus, the substrate size effect is small, when applying Sneddon's correction.

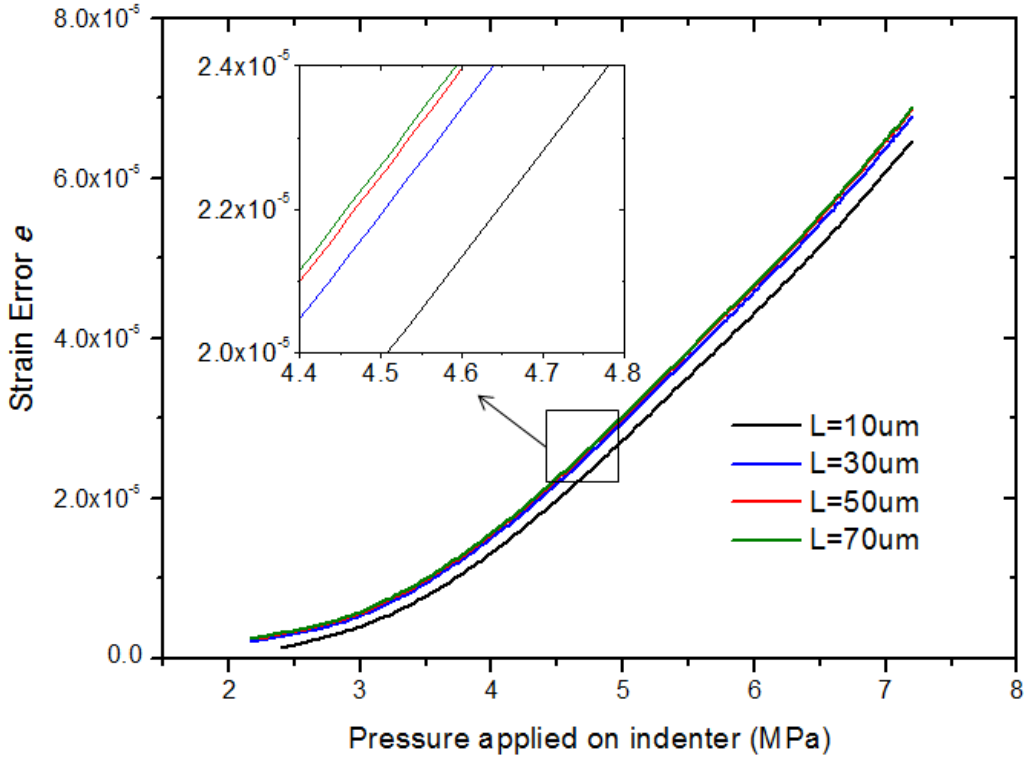


Figure 3.9 The substrate size effect for strain measurement of a plastic material.

Elastic substrate is one of the important assumptions of Sneddon's correction, and the FEM simulations discussed above are based on elastic materials. However, micro-compression is also used to study plastic materials, so

the substrate effect for plastic material is also of great interest. We tested a plastic material, whose stress-strain curve is shown in Figure 3.5. Same geometry as the elastic case is used, and the substrate size is varying from 10umX10um to 70umX70um. Figure 3.9 shows the trend of strain error is similar to elastic materials. The strain error curve of L=70um is very close to the curve of L=50um. The trend confirms that small substrate has small influence to the measurement of strain pillar. It also indicates that the substrate effect has a convergent value at $L \approx 50$um. And most importantly, by using Sneddon's correction, the strain error due to the substrate effect is small, less than 8E-5.

We can conclude that Sneddon's formula (Eq.(3.6)) can alleviate the substrate effect for both elastic and plastic materials, and the strain error is small and converges at $L > 50$um.

3.3.5 Aspect Ratio and Taper Angle Effect

Besides the substrate effect, the shape of the pillar itself will also affect the strain measurement, too. In this sub-section, we will discuss how the shape of pillar influences the pillar strain measurement.

An ideal cylindrical micro-pillar has two geometrical parameters, height and radius. The aspect ratio of a micro-pillar is defined as height over diameter,

$$\alpha = \frac{h_{pillar}}{2 \cdot r_{pillar}} \tag{3.10}$$

Usually, the pillar radius is fixed due to the machining, so we can control the aspect ratio by changing the pillar height. We conducted FEM simulations for

$\alpha = 2,3,4$ with a 50umX50um substrate. $r_{pillar}$ is fixed to 0.5um, and $h_{pillar} = 2,3,4$ um. First, elastic material is tested, E=50GPa, $\nu$ =0.3. Figure 3.10 shows that the absolute value of strain error is still small, less than 1.2E-4 when applied load is 100MPa. The strain error ratio $\eta$, dash line in Figure 3.10, decreases when the aspect ratio increases. This trend agrees with substrate effect in section 3.2.4, since the pillar height and substrate size are relative to each other. We can combine the two effects together by defining a ratio,

$$SNR = \frac{h_{pillar}}{L_{substrate}} \tag{3.11}$$

SNR is acting like signal-to-noise ratio. The larger the signal (pillar) or the smaller the noise (substrate), the more accurate the measurement of pillar strain. Large SNR will guarantee a good strain measurement.

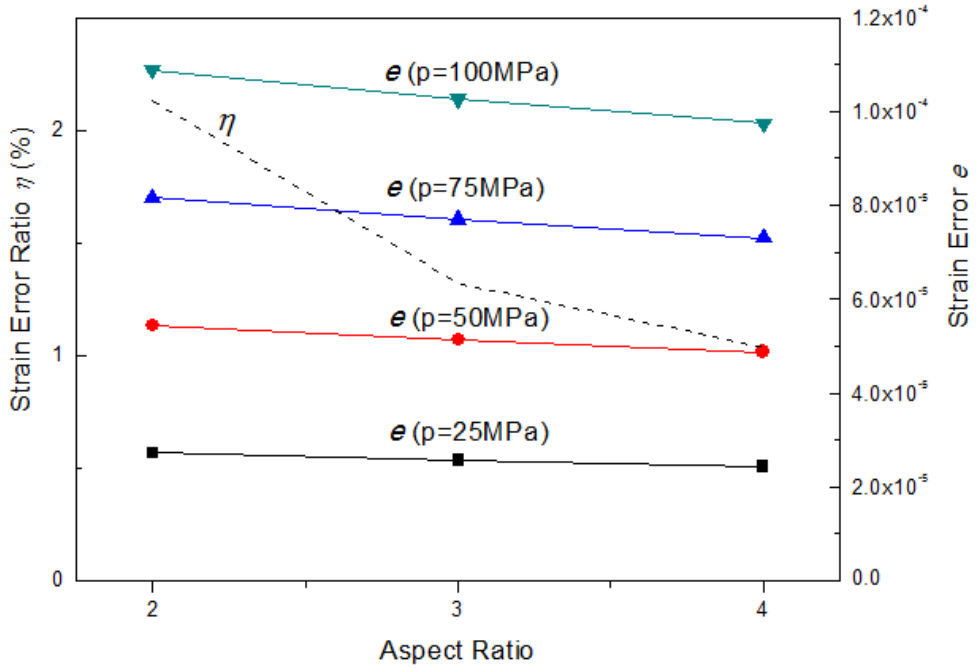


Figure 3.10. The aspect ratio effect of strain measurement for elastic material.

Plastic material (stress-strain curve in Figure 3.5) is also investigated for aspect ratio effect. Same geometry is used as elastic material cases above. As shown in Figure 3.11, the absolute value of strain error is small, less than 1.6e-4. And the strain rate ratio decreases when the aspect ratio increases. It's the same trend as the elastic material; higher aspect ratio is good for the strain measurement.

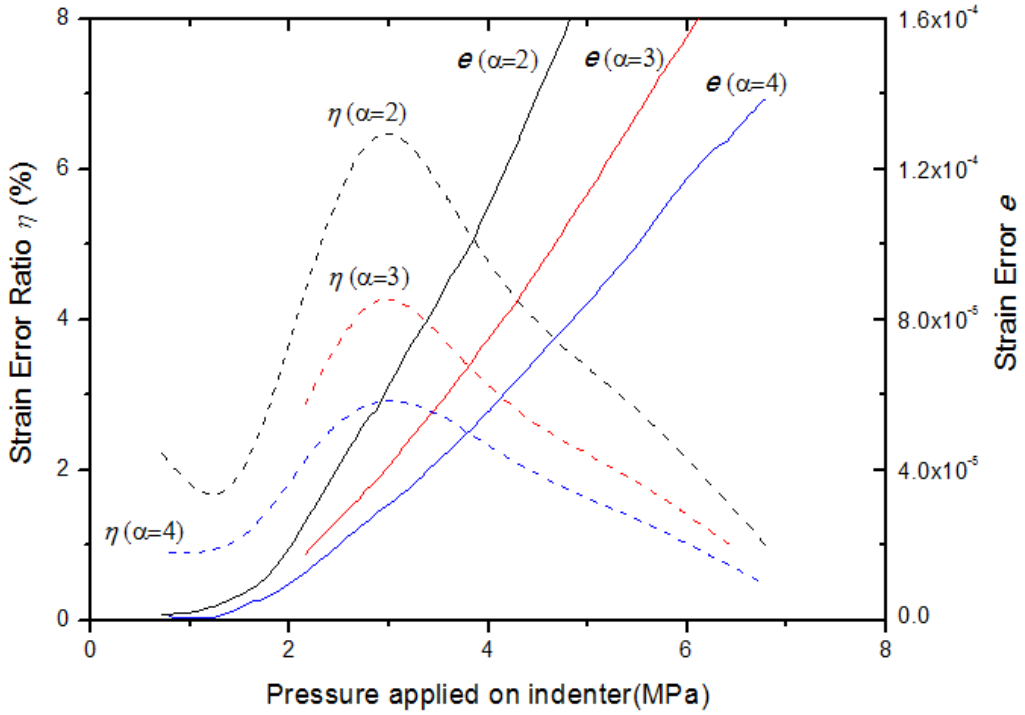


Figure 3.11. The aspect ratio effect of strain measurement for plastic material.

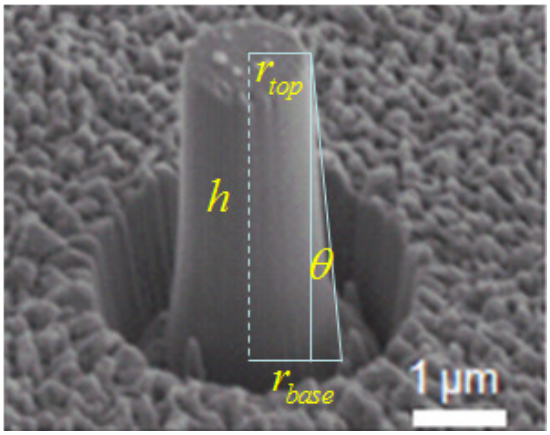


Figure 3.12. Micro-pillar with taper angle.

Besides the aspect ratio, another important shape parameter of pillar is taper angle. The micro-pillar is supposed to be perfectly vertical. However, due to the limitation of micro-machining, taper angle exists for most micro-pillars. Figure 3.12 shows a typical angled pillar, with an taper angle $\theta$. For an angled pillar, the base radius is larger than the top radius of the pillar, and they obey the following relation,

$$r_{base} = r_{top} + h \cdot \tan\theta = r_{top}(1 + \alpha \cdot \tan\theta) \tag{3.12}$$

We now investigate the effect of taper angle. A series of FEM simulations are conducted with taper angle ranging from $0^o$~$5^o$. The height of the pillar is 3 micrometer, the top radius of it is 0.5 micrometer, and the substrate size is 50 micrometer. Figures 3.13 & 3.14 represent the simulation results of elastic and plastic materials, respectively. The plots include both strain error and strain error ratio, left y-axis is the strain error ratio $\eta$, and right y-axis is the strain error $e$. The trend is very clear that higher taper angle has smaller strain error ratio and smaller strain error. The absolute value of strain error $e$ is small, less than 2.5E-4. Larger taper angle means a larger pillar base that will reduce the sinking effect of the pillar, thereby increase SNR. Larger aspect ratio results in large SNR, too. Therefore, large aspect ratio and taper angle can improve the strain accuracy.

The higher taper angle results in large base radius, and a larger base will make the pillar harder to sink into the substrate. And smaller pillar sinking means less deformation of substrate, which is desirable, as far as strain measurement is concerned.

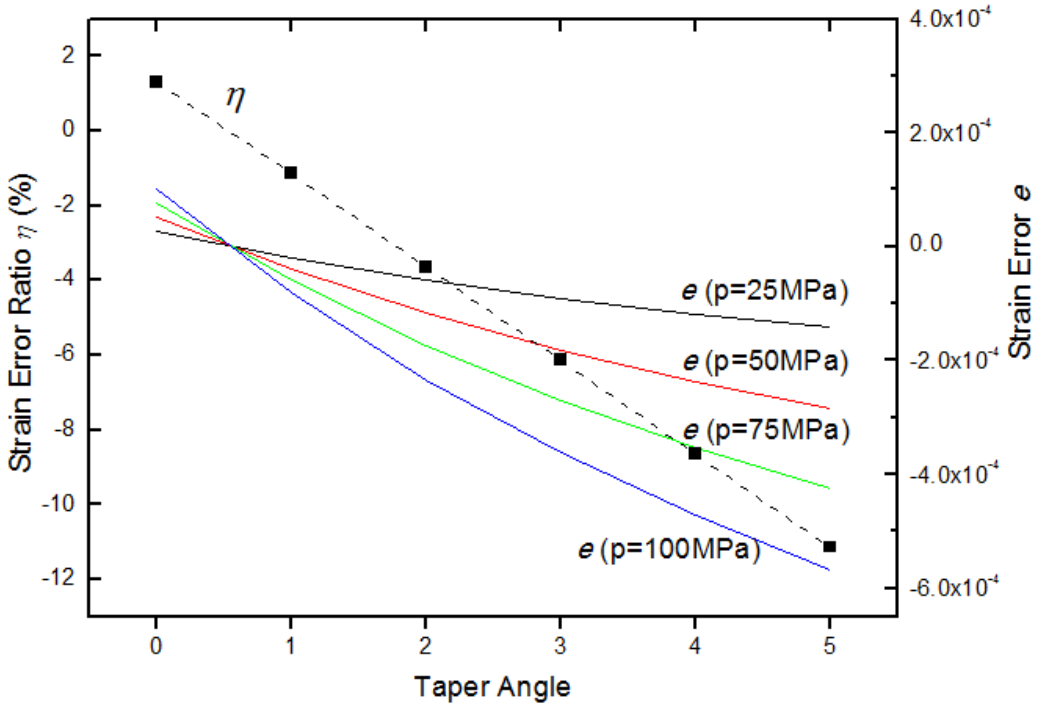


Figure 3.13. The taper angle effect of strain measurement for elastic material.

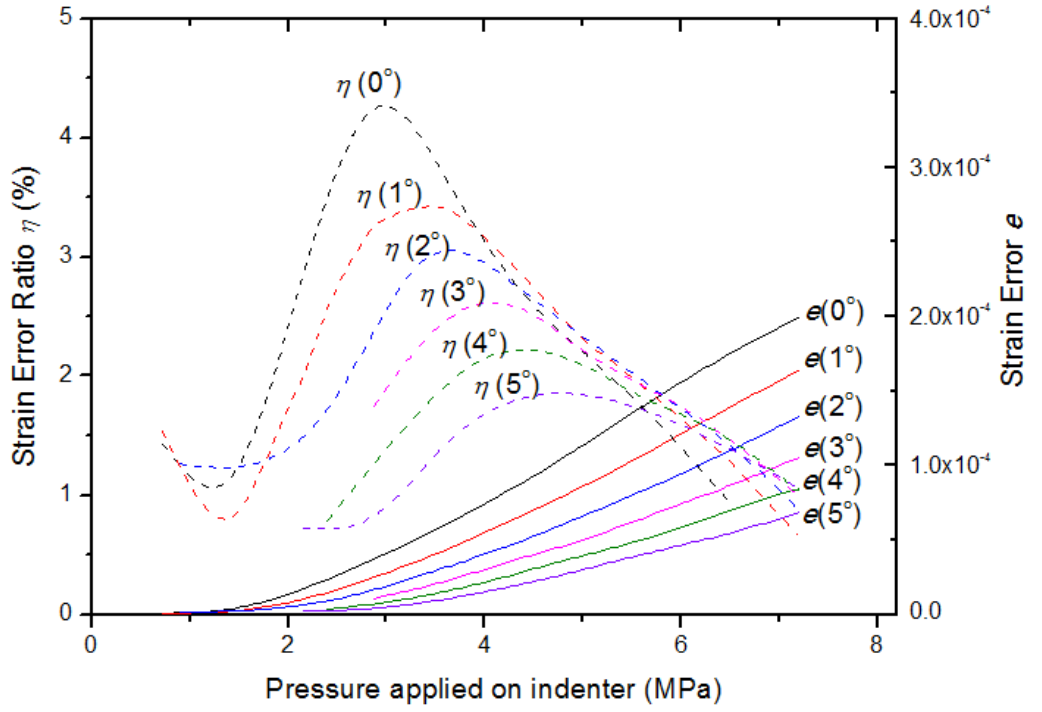


Figure 3.14. The taper angle effect of strain measurement for plastic material.

To conclude, the accuracy of strain measurement is influenced by two major factors: substrate and pillar. Larger substrate size will introduce more noise into the strain measurement, but when the size goes high (L > 50um), the strain error induced by substrate size converges to a certain value, which is acceptably small. As to the shape of the pillar, it is recommended to make pillars with high aspect ratio, before considering the destabilization of the high and tiny pillar. Pillar with large taper angle will reduce the deformation of substrate, and consequently increase the accuracy of strain measurement.

## 3.4 Measurement of Pillar Stress

The stress calculation in the micro-compression test is based on the assumption of uniaxial stress status in the pillar. The test is force-controlled, e.g. the pressure $p$ applied on top of the indenter is known, given by $f = \pi r_{indenter}^2 p$. The axial stress can be calculated by

$$\sigma_{yy} = \frac{f}{A_{pillar}} = \frac{r_{indenter}^2}{r_{pillar}^2} p \tag{3.13}$$

### 3.4.1 Taper Angle Effect

As mentioned above, due to the systematic error of micro-machining, taper angle exists for most micro-pillars. Figure 3.15 compares the stress field of two pillars, a vertical one and an angled one. The perfectly vertical pillar ($\theta = 0^o$) has a uniform axial stress distribution, so Eq. (3.13) can be directly applied. While for the angled pillar ($\theta = 5^o$), the axial stress is large on top, and small on bottom.

Due to the non-uniform stress field, we need a suitable formula to calculate macroscopic axial stress for the angled pillar.

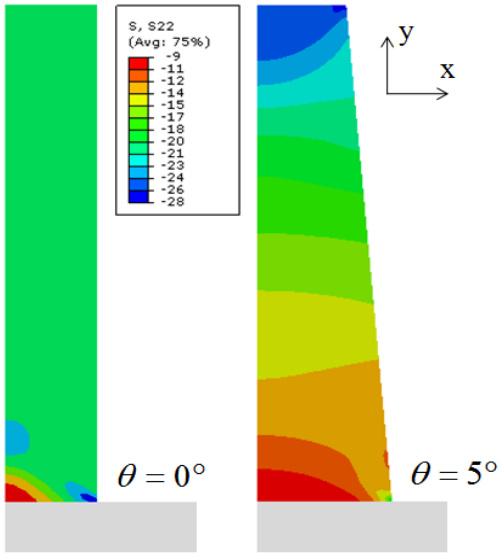


Figure 3.15. Axial stress distribution in vertical pillar and angled pillar.

Since $r_{top} \neq r_{base}$ for angled pillar, three straight-forward adjustments to Eq.(3.13) are established: the first one is regarding to the average cross sectional area of the pillar, given by

$$\sigma_{yy}^{(1)} = \frac{f}{\frac{1}{2}(A_{top} + A_{base})} = \frac{r_{indenter}^2}{\frac{1}{2}(r_{top}^2 + r_{base}^2)} p \tag{3.14}$$

the second one is based on the average pillar radius, given by

$$\sigma_{yy}^{(2)} = \frac{r_{indenter}^2}{\left(\frac{r_{top} + r_{base}}{2}\right)^2} p \tag{3.15}$$

and the third one is obtained by averaging the stress at the top and bottom surface,

$$\sigma_{yy}^{(3)} = \frac{1}{2}\left(\frac{f}{A_{top}} + \frac{f}{A_{base}}\right) = \frac{1}{2}\left(\frac{r_{indenter}^2}{r_{top}^2} + \frac{r_{indenter}^2}{r_{base}^2}\right) p \tag{3.16}$$

To quantify the taper angle effect on stress measurement, a series of FEM simulations are conducted via ABAQUS/Standard [41]. The taper angle changes from $0^o$ to $5^o$. Other geometrical parameters keep unchanged. The height of the pillar is 3 micrometer, the top radius of it is 0.5 micrometer, the indenter's radius is 1 micrometer, and the substrate size is 50 micrometer.

First, an Elastic material is used in the finite element analysis. The input material parameters are E=50GPa, $\nu$ =0.3. Then we calculate the Young's modulus from the simulation results by formula,

$$E_{test} = \frac{\Delta\sigma_{yy}^{(i)}}{\Delta\varepsilon_{pillar}^{Sneddon}}, i = 1,2,3 \tag{3.17}$$

Figure 3.16 shows that the measured Young's moduli are higher than the input Young's modulus 50GPa, especially when the taper angle is high. So the micro-compression test is not a good method to test Young's modulus.

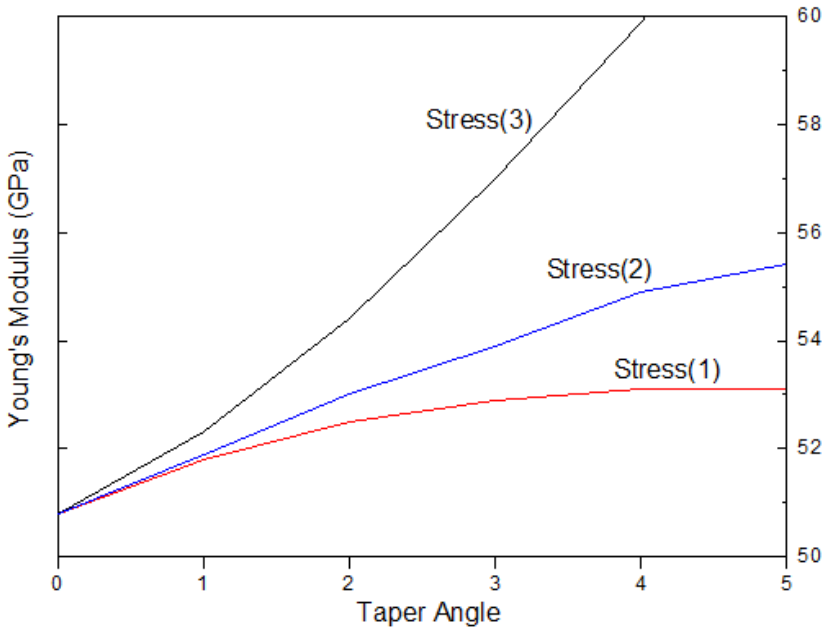


Figure 3.16. Comparison between Young's modulus obtained by three stress formulas for elastic material.

We also tested the plastic material given by Figure 3.5. To verify which stress form among Eq.(3.14),(3.15)&(3.16) gives the most accurate pillar stress, we compared two cases: $0^o$ pillar and a $5^o$ pillar. When $\theta = 0^o$, Eq.(3.14),(3.15) &(3.16) turn out to be the same. Figure 3.17 shows that the $0^o$ output stress-strain relation matches the input data very well. While for the $5^o$ pillar, stresses obtained by Eq.(3.14),(3.15)&(3.16) are different, and it is clear that

$$\sigma_{yy}^{Input} \approx \sigma_{yy}^{(3)} > \sigma_{yy}^{(2)} > \sigma_{yy}^{(1)} \tag{3.18}$$

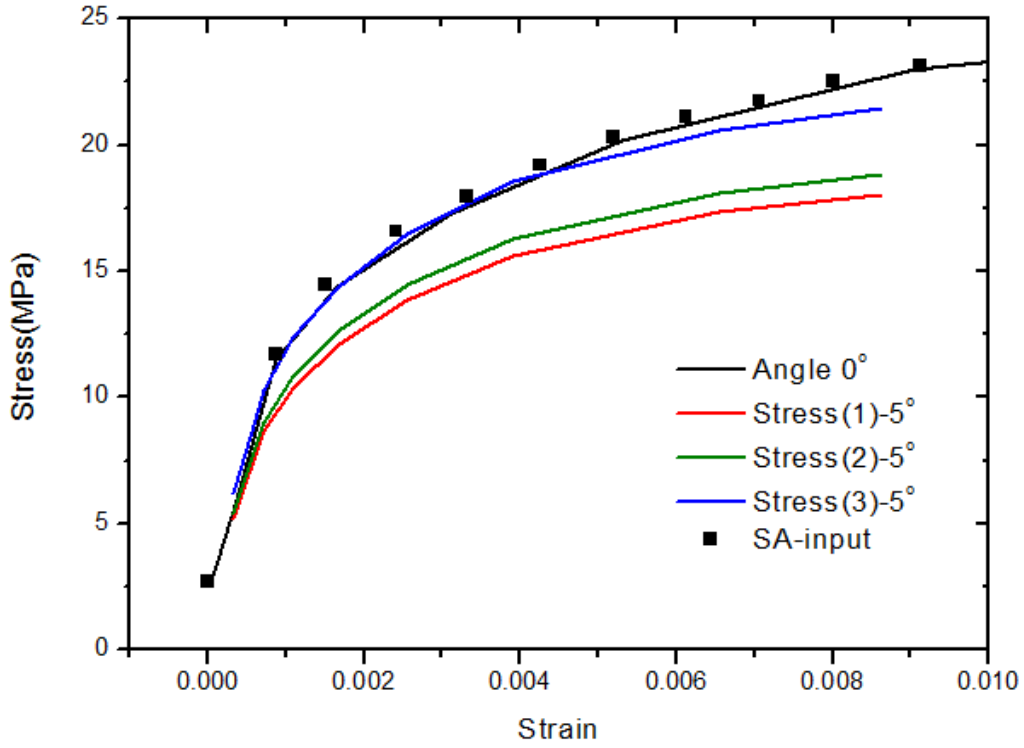


Figure. 3.17. Comparison between three formulas to calculate axial stress for a $5^o$ pillar, plastic material.

Thus, for the following analysis, Eq. (3.16) will be used to calculate axial stress for angled pillar. It should be noted that large taper angle leads to large error in stress measurement. By calculating stress with Eq. (3.16), Figure 3.18

illustrates this clear trend, which differs from the angle effect for strain measurement in Section 3.3.

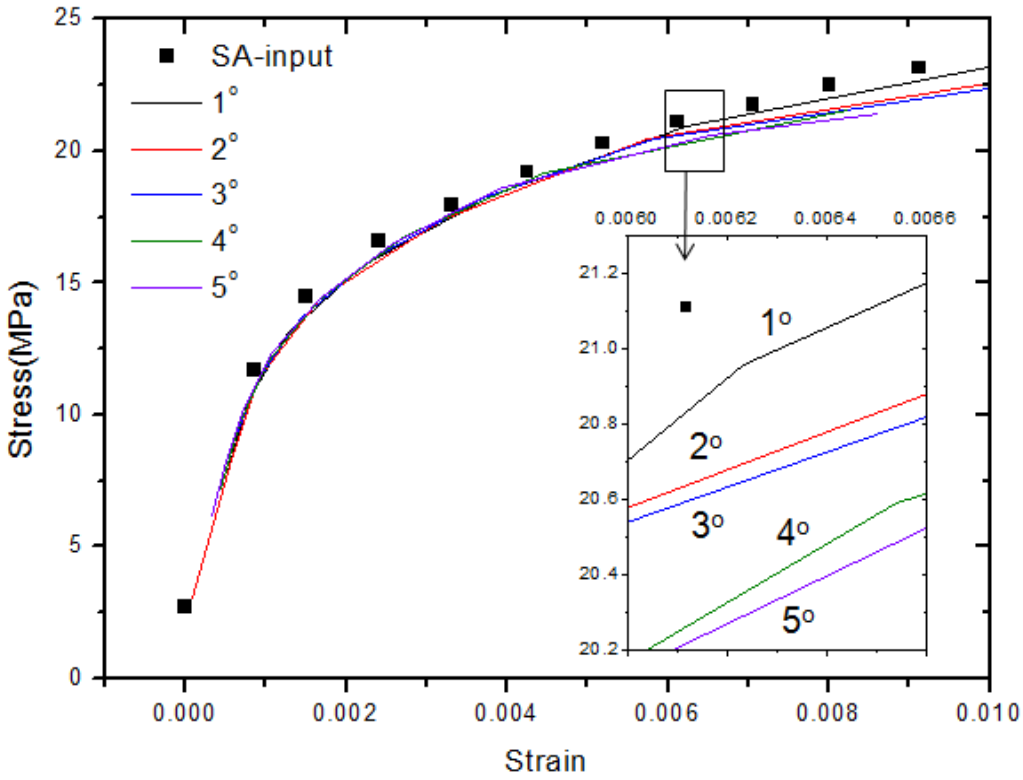


Figure 3.18. The taper angle effect for stress measurement of the plastic material.

3.4.2 Aspect Ratio Effect

The other concern is about how the aspect ratio of the pillar affects the stress measurement. Usually, the aspect ratio effect is coupled with angle effect. To calibrate the aspect ratio effect, two sets of FEM simulations are conducted via ABAQUS/Standard [41]. In the first set, the taper angle is fixed to $0^{o}$, and the substrate size is 50 micrometer. The pillar radius is 0.5 micrometer, and the height of the pillar changes from 2 to 4 micrometer. In the second set, the taper angle is fixed to $5^{o}$, and other parameters keep the same with set one. Figure 3.19 shows

the simulation results of these two sets (totally six cases), and the stress is calculated by Eq. (3.16).

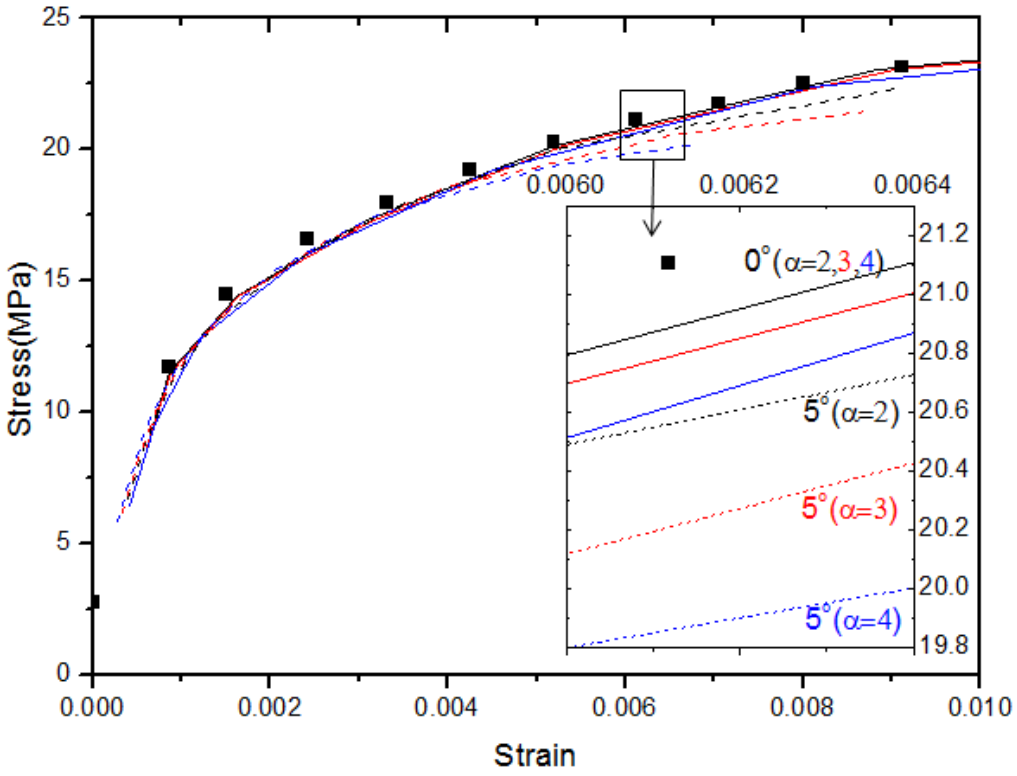


Figure 3.19. The coupled taper angle and aspect ratio effects for stress measurement of plastic material

Generally, high aspect ratio will make the stress measurement inaccurate. The solid lines in the Figure 3.19 represent cases of $0^o$, and dash lines are $5^o$ cases. When the taper angle is $0^o$, the aspect ratio effect is small. And the aspect ratio effect is enlarged, when the taper angle increases to $5^o$. The physical meaning for the phenomena is that the base radiuses of vertical pillar and angled pillar are different. The vertical pillar has a uniform radius, while the base radius of angled pillar is a function of aspect ratio and taper angle, as shown in Eq. (3.12). Both aspect ratio and taper angle contribute to the increase of the base radius.

Consequently, large base radius leads to a more severely inhomogeneous stress field, which will make the stress measurement more inaccurate.

3.5 Finite Element Model of Brittle Fracture Based on Experiment Results

The adjustments for strain/stress measurement proposed in previous sections were applied on experimental result. Collaborative experiment work was done by Jiang and Chawla [12]. The single-crystal nodules of $Cu_6Sn_5$ were fabricated by FIB and tested in compression using a nanoindenter (MTS XP, Agilent Technologies, Chandler, AZ), and a Berkovich indenter (three-sided pyramid, Micromaterials, Wrexham, UK) with a flat triangular cross-section ($10\ \mu m \times 10\ \mu m$). Experiments were conducted with a nominal strain rate of 0.05/s [12]. The average fracture stress of the micropillar is 1,356±64 MPa and the strain to failure is 1.37±0.18% [12].

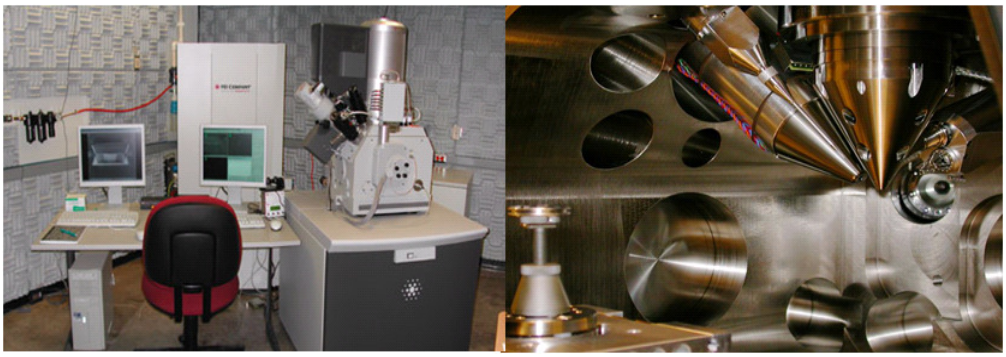

Figure 3.20. Focused Ion Beam (FIB) at ASU and the chamber inside FIB (Courtesy of L. Jiang and N. Chawla)

The experimental data is utilized to build a finite element model for brittle fracture. Fracture type is strain controlled. Young's Modulus is 112GPa. Direct cracking fracture strain is set to 1.21%, and fracture stress is 1356 MPa. Failure strain is 1.37%. Shear retention is described by power law retention in ABAQUS,

and the power is set to 2. The same failure criteria will be used in Chapter 5 when studying the brittle fracture of intermetallics in solder joint.

Figure 3.21 shows the FE model and simulation result of a bulk rectangular specimen under uniaxial tension. The left end is fixed, and the right end is subject to velocity load. This is a simple example to illustrate how the brittle fracture works in ABAQUS/Explicit [41]. With 2,400 CPS4R elements (4-node bilinear plane stress quadrilateral with reduced integration), the result does have cracks when it reaches the failure criteria. Further study of the brittle fracture in the intermetallic layer of the solder joint will be seen in Chapter 5.

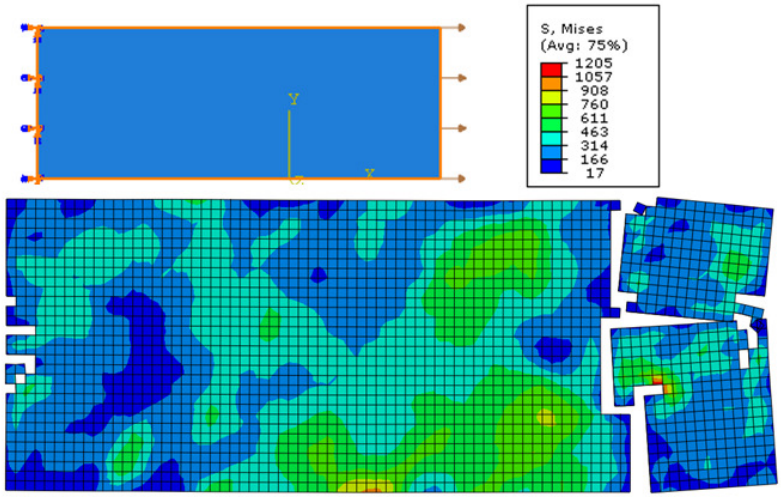


Figure 3.21. FE model and simulation result of the brittle fracture of $Cu_6Sn_5$.

## 3.6 Summary

In this chapter, we introduced the micro-compression method to study the mechanical behavior of micro-scale intermetallics. Due to the limitation of the small scale, the stress and strain of the micropillar cannot be directly measured in the experiment. We systematically investigated factors that may affect the stress/strain measurement in the micro-compression test. With certain empirical

adjustments to stress/strain measurement, the micro-compression test is believed to a reliable method to obtain the elastic-plastic properties of intermetallics and other small scale materials.

For the strain measurement, we use Sneddon's formula to calculate the real pillar strain from the indentation depth. Generally, Sneddon's formula can provide a good estimation for the pillar strain, and the absolute value of strain error is very small (1E-5 order of magnitude). Our parametric study suggests that the substrate size is the smaller the better; however, even the substrate size goes very large, the influence of the substrate to the strain measurement converges to a certain value. The accurate strain measurement prefers high aspect ratio and taper angle of the pillar.

Pillars with taper angle have inhomogeneous stress distribution, which differs from the ideally vertical pillars. In the study of stress measurement of angled pillar, we proposed three formulas to calculate axial stress of the pillar, and it turns out that the linear average of the top and base stress is the most accurate one for angled pillar. Taper angle effect and aspect ratio effect are investigated, and it is believed that low aspect ratio and taper angle will benefit the accuracy of stress measurement.

Collaborators have done the micro-compression experiment on the fracture mechanisms of the important intermetallic $Cu_6Sn_5$. Adjustments on stress/strain measurements were successfully applied.

# CHAPTER 4

# INTERFACIAL LAW FOR SOLDER/INTERMETALLIC INTERFACE

## 4.1 Introduction

The fracture mechanisms of Pb-free solder joints are quite complex due to: (a) the large difference in deformation behavior of the individual components, and (b) the many interfaces that are formed in the system. We have investigated the mechanical behaviors of bulk solder alloys and intermetallic compound in previous chapters. A comprehensive understanding of the fracture behavior of Pb-free solder joints requires the application of accurate and realistic constitutive relations for the individual components as well as the behavior of the interfaces.

One way to study the interfacial behavior of the interfaces in this system is by molecular simulations, for example, molecular dynamics using empirical bond order potentials. Molecular simulations, however, are only valid for short time scales (on the order of $10^{-12}$ second) and length scales (on the order of 1 μm), so it is unpractical to model the entire solder joint using this approach.

On the other hand, continuum models, especially cohesive zone model is used in the continuum study of interfacial fracture. Pioneered by Dugdale [80], Barenbalatt [81], Rice [82] and others, interfaces have been characterized by the cohesive zone model [83-95], as an alternative to the conventional crack initiation and propagation criteria, which are normally based on the measurement of fracture parameters (e.g., stress intensity factor K and J-integral). A cohesive zone model assumes a cohesive zone law that is described by the relationship between

normal traction and the opening displacement of the interface. Fracture or decohesion is controlled by the interfacial separation across cohesive zone (interface). The interfacial separation is resisted by the cohesive traction which, in turn, is described as a function of the separation. The interfacial behavior is thus specified in terms of the critical interfacial strength and work of separation per unit area (i.e., cohesive energy), and no assumptions regarding the presence of an initial decohesion are required.

By using the multi-scale approach, the continuum cohesive law can be extended to the atomic domain. Recently, this approach is used to develop a cohesive law for the interface between carbon nanotubes and a polymer matrix in polymer composites[96-100].

With respect to fracture analysis of the solder joint system, the interface between solder and intermetallic deserves further investigation, since the fractures always occur somewhere close to the solder/intermetallic interface. In this chapter, a cohesive zone law for the interface between Sn and $Cu_6Sn_5$ is developed from the Modified Embedded Atom Method (MEAM)[101-110]. We begin with a briefly review of the Modified Embedded Atom Method. By converting atomistic relations to homogeneous continuum relation, an analytical interfacial traction-separation law for Sn/$Cu_6Sn_5$ interface is created. To study the fracture cohesive zone, we build a finite element model that incorporates the interfacial law for Sn/$Cu_6Sn_5$ interface. Then we conclude with a comparison with experiments of Pb-free solder joints and fractographic analysis.

## 4.2 Modified Embedded Atom Method

In this section, we first briefly review the Modified Embedded Atom Method (MEAM) potential, and then utilize it to determining the cohesive law of the interface between Sn and $Cu_6Sn_5$ in a solder joint.

### 4.2.1 Review of MEAM

The review of MEAM theory is based on Baskes' work [103, 108, 109]. The total energy, $U$, of an embedding atom $A$ into a sea of "background atoms" $B$ is given by (Fig. 4.1):

$$U = \sum_i \left[ F_A\left(\overline{\rho}_{i,AB}\right) + \frac{1}{2}\sum_j \phi_{AB}\left(R_{ij}\right) \right] \tag{4.1}$$

where $i$ and $j$ denote the spatial positions for type $A$ atoms and type $B$ atoms, respectively. $F_A$ is the embedding function of the type $A$ atom and is a function of the local electron density $\overline{\rho}_{i,AB}$ given by the background atoms $B$. $F_A$ is given by the following expression:

$$F_A = A_A E_A^0 \overline{\rho}_{i,AB} \ln \overline{\rho}_{i,AB} \tag{4.2}$$

where $A_A$ is a dimensionless adjustable parameter and $E_A^0$ is the cohesive energy of atom type $A$. The local electron density $\overline{\rho}_{i,AB}$ encompasses the total contributions from all background atoms $B$ to the embedding atom $A$ at position $i$.

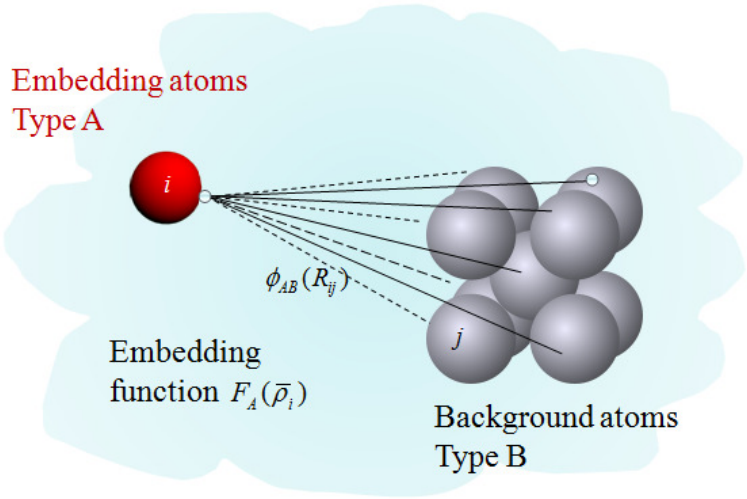


Figure 4.1. Schematic of the embedding atoms interacting with the background atoms through embedding function depending on the local electron density.

This function decays with an increase in distance between atoms *A* and *B*, which is given by:

$$\bar{\rho}_{i,AB} = \sum_j \exp\left[-\beta_B\left(\frac{R_{ij}}{R_{AB}^0} - 1\right)\right] \tag{4.3}$$

where $\beta_B$ is a decay constant and $R_{AB}^0$ is the equilibrium distance between nearest neighboring atoms in the reference lattice (i.e., a conceptual material comprising atoms *A* and *B* with a ratio of their valences). Function $\phi_{AB}$ is the pair potential between two atoms of type *A* and *B* and depends on the interatomic distance $R_{ij}$. It is noted that the embedding atom and the background atom can be the same or different since one can embed a pure metal into an alloy that has the composition of the metal as we will discuss in the following.

4.2.2 Interfacial Potential

In solder joint system, we are interested in the potential of the interface between solder alloy and intermetallics. In the following derivation, we will focus on the interface between pure Sn and $Cu_6Sn_5$. According to the MEAM theory, pure Sn is considered as the background, due to its majority in the system. Cu and Sn atoms of $Cu_6Sn_5$ are embedded into the pure Sn matrix.

Applying Eq.(4.3), the local electron density of a Cu atom is $\bar{\rho}_{i,Cu} = \sum_j \exp\left[-\beta_{Sn}\left(R_{ij} / R^0_{Cu_3Sn} - 1\right)\right]$ by taking a Cu-Sn alloy with ratio of 3:1. It should be noted that $Cu_3Sn$ (by the ratio of valences of Cu and Sn) is taken as the reference, although $Cu_3Sn$ is not the really alloy here, and $R^0_{Cu_3Sn}$ is taken as the average lattice constant in $Cu_3Sn$. The local electron density for a Sn atom is $\bar{\rho}_{i,Sn} = \sum_j \exp\left[-\beta_{Sn}\left(R_{ij} / R^0_{Sn} - 1\right)\right]$. The pair potential for two Sn atoms is then given by:

$$\phi_{Sn-Sn}\left(R_{ij}\right) = \frac{1}{2}\left\{-E^0_{Sn}\left[1+\alpha_{Sn}\left(\frac{R_{ij}}{R^0_{Sn}}-1\right)\right]\exp\left[-\alpha_{Sn}\left(\frac{R_{ij}}{R^0_{Sn}}-1\right)\right] - F_{Sn}\left(\frac{\bar{\rho}_{i,Sn}}{4}\right)\right\} \tag{4.4}$$

and the counterpart potential for a Cu atom and a Sn atom is:

$$\phi_{Cu-Sn}\left(R_{ij}\right)=-\frac{1}{3}E^{0}_{Cu_3Sn}\left[1+\alpha_{Cu_3Sn}\left(\frac{R_{ij}}{R^{0}_{Cu_3Sn}}-1\right)\right]\exp\left[-\alpha_{Cu_3Sn}\left(\frac{R_{ij}}{R^{0}_{Cu_3Cn}}-1\right)\right]$$
$$-\frac{1}{4}F_{Cu}\left(\frac{\overline{\rho}_{i,Cu}}{12}\right)-\frac{1}{12}F_{Sn}\left(\frac{\overline{\rho}_{i,Sn}}{4}\right)$$
$$-\frac{1}{6}\left\{-E^{0}_{Cu}\left(1+\alpha_{Cu}\left(\frac{R_{ij}}{R^{0}_{Cu}}-1\right)\right)\exp\left[-\alpha_{Cu}\left(\frac{R_{ij}}{R^{0}_{Cu}}-1\right)\right]-F_{Cu}\left(\frac{\overline{\rho}_{i,Cu}}{12}\right)\right\} \tag{4.5}$$

The parameters used are listed in Table 4.

Table 4.

Parameters of MEAM Potential for the Sn/$Cu_6Sn_5$ Interface.

| Composition | $E^0\left(\text{eV}\right)$ | $A$ | $R^0\left(\text{nm}\right)$ | $\alpha$ | $\beta$ |
|---|---|---|---|---|---|
| Cu | 3.62 | 1.07 | 0.25 | 5.106 | 3.62 |
| Sn | 3.08 | 1.0 | 0.344 | 6.20 | 6.2 |
| $Cu_3Sn$ | 3.5 | | 0.268 | 5.38 | |

4.3 Cohesive Law for Solder/Intermetallic Interface

Based on the MEAM potential obtained in section 4.2, we can now formulate the cohesive law for the Sn/$Cu_6Sn_5$ interface in the system. It should be noted that fracture in Sn-Cu joints almost always takes place within the solder, in the vicinity of the Sn/$Cu_6Sn_5$ IMC layer, or within the IMC layer. Since fracture never really takes place between Cu and $Cu_6Sn_5$, we assume perfect bonding at this interface. Atomic structures of Cu (FCC), IMC, and Sn (BCT) are needed to calculate the number densities of atoms to be used in the analysis and the interface is illustrated in Fig. 4.2.

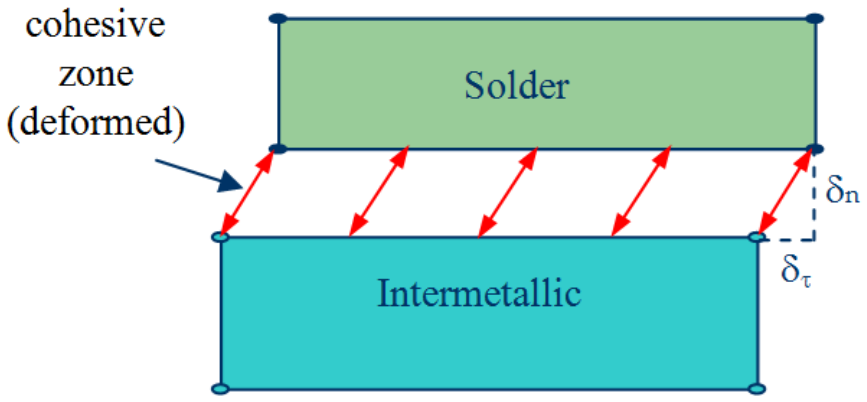


Figure 4.2. Solder/intermetallic interface.

4.3.1. Atomistic Potential of Single Intermetallic Layer

We first consider the interaction of one layer of IMC atoms and Sn (Fig. 4.3), i.e., the interaction between the IMC and Sn is limited to the nearest neighboring IMC atoms. The separation distance between the IMC layer and Sn is represented by $h$ (which is to be determined). The energy stored in an infinitesimal area $d\Omega$ of the IMC layer can be written as:

$$U = \sum_{i \text{ of Sn in } d\Omega} \left[ F_{Sn}\left(\bar{\rho}_{i,Sn}\right) + \frac{1}{2} \sum_{j \text{ of bulk Sn}} \phi_{Sn-Sn}\left(R_{ij}\right) \right] + \sum_{i \text{ of Cu in } d\Omega} \left[ F_{Cu}\left(\bar{\rho}_{i,Cu}\right) + \frac{1}{2} \sum_{j \text{ of bulk Sn}} \phi_{Cu-Sn}\left(R_{ij}\right) \right] \tag{4.6}$$

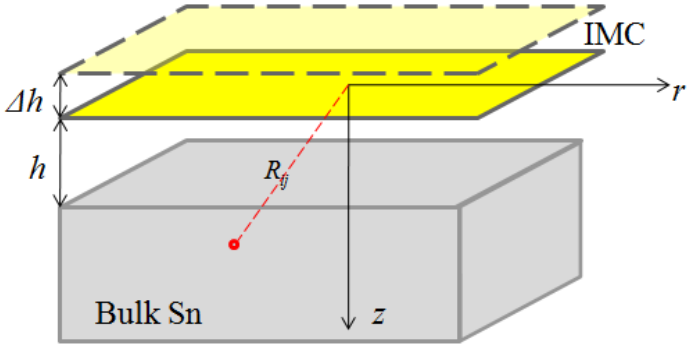


Figure 4.3. A schematic diagram of an IMC layer parallel to the surface of an infinite bulk Sn. $h$ is the separation and $\Delta h$ is the opening displacement.

Instead of using a discrete summation over all Cu and Sn atoms, we adopt a continuum method by homogenization. Specifically, the discrete summation is evaluated by means of integral. Equation (4.6) then becomes:

$$\begin{aligned} U = \rho_{Sn}^{IMC} t_{IMC} d\Omega \left[ F_{Sn}\left(\bar{\rho}_{Sn}\right) + \frac{1}{2} \int_{V_{\text{bulk Sn}}} \phi_{Sn-Sn}\left(R\right) \rho_{Sn}^{bulk} dV \right] \\ + \rho_{Cu}^{IMC} t_{IMC} d\Omega \left[ F_{Cu}\left(\bar{\rho}_{Cu}\right) + \frac{1}{2} \int_{V_{\text{bulk Sn}}} \phi_{Cu-Sn}\left(R\right) \rho_{Sn}^{bulk} dV \right] \end{aligned} \tag{4.7}$$

where $\rho_{Cu}^{IMC}\left(=26.76/nm^3\right)$ and $\rho_{Sn}^{IMC}\left(=22.3/nm^3\right)$ are number densities of Sn and Cu atoms in $Cu_6Sn_5$ (see Appendix C for number density calculation); $t_{IMC}=\left(a_{IMC}+b_{IMC}+c_{IMC}\right)/3=0.45nm$ is the average thickness of an IMC layer; $V_{\text{bulk Sn}}$ is the volume of the bulk Sn as the background; and $\rho_{Sn}^{bulk}\left(=34/nm^3\right)$ is the number density of Sn atom in the bulk Sn. The subscripts "*i*" and "*j*" for local electron density $\bar{\rho}$ and distance $R$ are dropped since for the infinite two-dimensional layer and three-dimensional bulk, specific positions are not important in the infinite body.

The local electron density can also be evaluated by integration over all background Sn atoms. The distance between a point (0, 0) on the IMC layer and a point ($z$, $r$) ( $z \geq h, r \geq 0$ ) in the bulk Sn (Fig. 4.3) is $R_{ij}=\sqrt{r^2+z^2}$ . Then, the local electron densities can be expressed and obtained as:

$$\begin{aligned}\bar{\rho}_{Cu} &= \int_{z=h}^{\infty}\int_{r=0}^{\infty} -\beta_{Sn}\left(\frac{\sqrt{r^2+z^2}}{R^0_{Cu_3Sn}}-1\right)\rho^{bulk}_{Sn}\,2\pi r dr dz \\ &= 2\pi\rho^{bulk}_{Sn} h\frac{\left(R^0_{Cu_3Sn}\right)^2}{\beta^3_{Sn}}\left(\beta_{Sn}+\frac{2R^0_{Cu_3Sn}}{h}\right)\exp\left[\beta_{Sn}\left(1-\frac{h}{R^0_{Cu_3Sn}}\right)\right]\end{aligned} \tag{4.8}$$

$$\begin{aligned}\bar{\rho}_{Sn} &= \int_{z=h}^{\infty}\int_{r=0}^{\infty} -\beta_{Sn}\left(\frac{\sqrt{r^2+z^2}}{R^0_{Sn}}-1\right)\rho^{bulk}_{Sn}\,2\pi r dr dz \\ &= 2\pi\rho^{bulk}_{Sn} h\frac{\left(R^0_{Sn}\right)^2}{\beta^3_{Sn}}\left(\beta_{Sn}+\frac{2R^0_{Sn}}{h}\right)\exp\left[\beta_{Sn}\left(1-\frac{h}{R^0_{Sn}}\right)\right]\end{aligned} \tag{4.9}$$

The analytical expressions for the pair potential can also be obtained, although it is somewhat lengthy (see Appendix D). The above expressions all depend on a single variable, the separation distance $h$. The cohesive energy $\Phi$ is the energy per unit volume and is given by:

$$\Phi(h) = \frac{U(h)}{t_{IMC} d\Omega} \tag{4.10}$$

The equilibrium separation between a single layer of IMC and a bulk Sn is determined by the minimization of the cohesive energy with respect to the separation $h$, i.e., to solve $h$ via

$$\frac{\partial\Phi}{\partial h} = 0 \tag{4.11}$$

and

$$h = h_0 = 0.297 \text{ nm} \tag{4.12}$$

Upon external load, the separation deviates from the equilibrium separation $h_0$ to $h_0+\Delta h$, where $\Delta h$ is the increment or opening displacement. Thus, the

cohesive energy depends on the opening displacement $\Delta h$, i.e., $\Phi = \Phi(h_0 + \Delta h)$, by simply replacing $h$ to $h_0+\Delta h$. Note that the sliding displacement does not affect the cohesive energy because of the infinite size of the two-dimensional layer and three-dimensional plate. This leads to the shear cohesive stress being negligible. The tensile cohesive stress is the obtained from the work-conjugate relation by:

$$\sigma(\Delta h) = \frac{\partial \Phi(\Delta h)}{\partial(\Delta h / h_0)} \tag{4.13}$$

Equation (4.13) gives the cohesive law for one layer of IMC and bulk Sn, as shown in Fig. 4.4. The cohesive strength is given by $\sigma_{\max} = 12.67\ GPa$ and is reached at the critical separation distance, $\Delta h_{critical} = 0.062nm$. The area under the curve represents the total cohesive energy and is $\Gamma = 2.22\ J/m^2$.

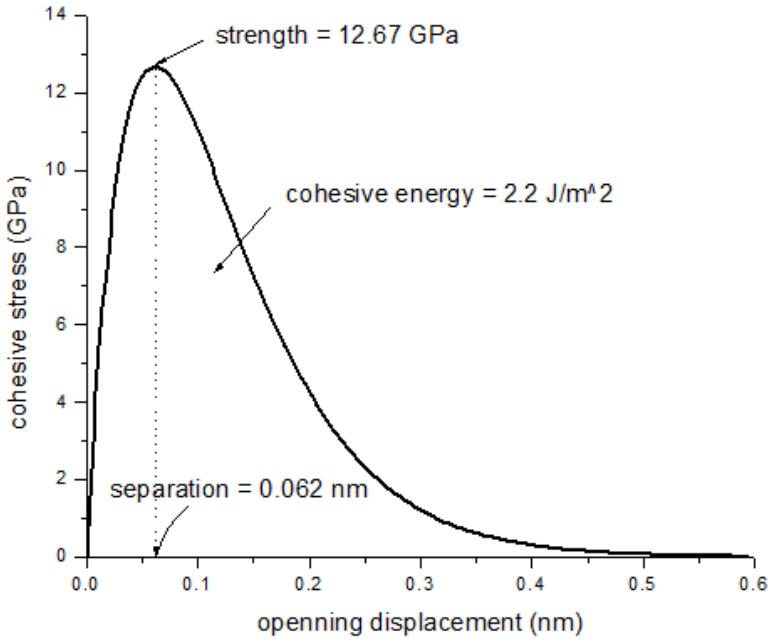


Figure 4.4. The tensile cohesive stress versus the opening displacement.

4.3.2. Atomistic Potential of Multiple Intermetallic Layer

Now we consider multiple atomic layers of IMCs interacting with bulk Sn (Fig. 4.5). The interactions between IMC layers are ignored in the following analysis. In other words, IMC layers are separated from the bulk Sn as a whole, which provides an upper-limit of the interfacial strength. The interlayer spacing of the IMC layers is taken to be the average IMC lattice constants $a_{IMC}$, $b_{IMC}$ and $c_{IMC}$ by $t_{IMC} = (a_{IMC} + b_{IMC} + c_{IMC})/3 = 0.45nm$ . The total cohesive energy $\Phi_{multi-layer}$ is then given by:

$$\Phi_{multi-layer}(h) = \Phi(h) + \Phi(h + t_{IMC}) + \cdots + \Phi(h + n \cdot t_{IMC}) \tag{4.14}$$

where $\Phi(h)$ is the cohesive energy for the single layer of IMC/bulk Sn, given by Eq. (10); $n$+1 is the number of IMC layers. The expression for each term on the right hand side of Eq. (4.14) is the same as that given by Eq. (4.10) if $h$ is replaced by $h + t_{IMC}$.

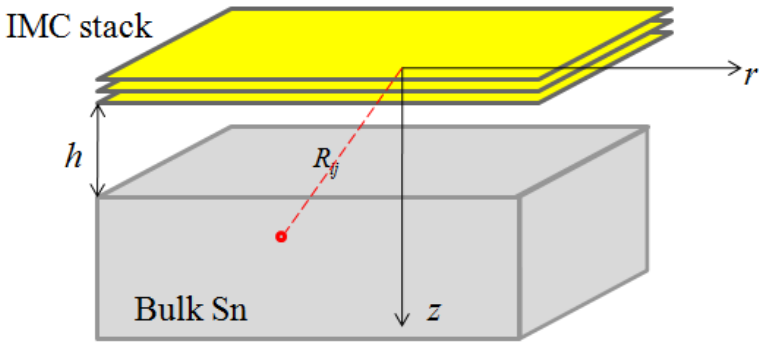


Figure 4.5. A schematic diagram of multilayer IMC parallel to the surface of an infinite bulk Sn. $h$ is the separation; $t_{IMC}$ is the interlayer spacing and $\Delta h$ is the opening displacement.

To study the influence of multilayer atoms on the interfacial properties, we investigated five cases, $n$ = 1~5, compared with the single layer case ($n$ = 0). The

equilibrium separation is then determined by energy minimization with respect to *h*. Table 5 shows the equilibrium separation and minimum energy for each *n*. The trend is very clear that the result converges at $n = 2$, which reflects the fact that the interaction between atoms is short distance potential, and the far-end atoms cannot affect the interface property much.

Table 5.

Equilibrium Separation and Minimum Energy for Single and Multiple Layer of Intermetallic Atoms.

| *n* | Equilibrium Distance (Å) | Minimum Energy ($eV/nm^3$) |
|---|---|---|
| 1 | 2.965637 | -44.16345503 |
| 2 | 2.963012 | -44.36531363 |
| 3 | 2.963011 | -44.36543298 |
| 4 | 2.963010 | -44.36543489 |
| 5 | 2.963010 | -44.36543489 |

Thus, equilibrium separation for $n \geq 1$ is,

$$h = h_0 \approx 0.296 \text{ nm}, \qquad n \geq 1 \tag{4.15}$$

The difference between the multilayer model ( $n \geq 1$ ) and single layer model ( $n = 0, h_0 \approx 0.297$ nm ) is negligible because of the steep decay of the interaction, characterized by the decay constants $\beta_{Cu}$ and $\beta_{Sn}$. The cohesive stress/separation and total cohesive energy are also similar to the single layer model. An application of traction-separation law on fracture model using cohesive element is provided in Appendix E.

4.4 Comparison with Experiments

Actually, most fractures, in experiments, occur in solder or intermetallic regions, instead of the interface. The high cohesive energy of the solder/intermetallic interface may explain this phenomenon. The cohesive energies for pure Sn and intermetallic have been given either by experiments or atomic simulations. The typical value for Sn is 0.681 $J/m^2$ [110] and for Cu 1.031 $J/m^2$ [110], which are much smaller than the cohesive energy $\Gamma = 2.22 J/m^2$ for the interface as predicted by the analysis in section 4.3. The cohesive energy provides the fracture resistance based on the Griffith energy balance. It should be noted that fracture in ductile materials, such as Cu and Sn or solder alloys, takes place by slip, void growth, etc., so it fails at a stress much lower than the cohesive strength.

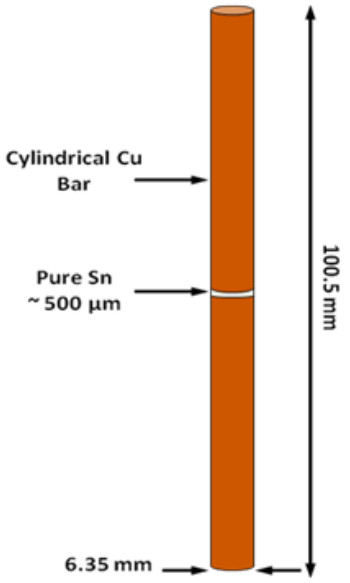


Figure 4.6. Experimental geometry of a pure Sn solder joint subjected to uniaxial tension. (Courtesy of K. Yazzie)

In order to validate our theoretical analysis, we compare with experiments with finite element analysis. A cylindrical sample, consisting of a thin Sn section sandwiched between two copper bars, is tested in tension. The dimension and the geometry of the joint are shown by Fig. 4.6.

The strain is measured by extensometer with a 10 mm gage length. Even though most of the strain comes from the plastic deformation of the Sn, the elastic contribution of the Cu bars is also subtracted. The finite element model consisted of Cu, IMC, interface and bulk Sn. Cu is modeled as an elastic material with Young's modulus of 116 GPa and Poisson's ratio of 0.3. IMC had a Young's modulus of 112.3 GPa and Poisson's ratio of 0.3. Pure Sn was modeled as an elastic-plastic material and was determined by experiments on bulk Sn. The stress-separation constitutive relation of IMC/Sn interface is given by Eq. (4.13) or Fig. 4.4. The same geometry and compensation are used to compare with experiments. The thickness of interface is taken to be 0.01 mm in the simulation. We used CAX4H axisymmetric elements in ABAQUS. Model convergence was reached by continuously refining the mesh until the values of stress did not change. Figure 4.7 shows the von-Misses stress and the effective plastic strain, in which it is noted that the maximum stress/strain takes place at Sn very close to IMC. This is another piece of evidence that the fracture always occurs in the solder region close to the solder/IMC interface.

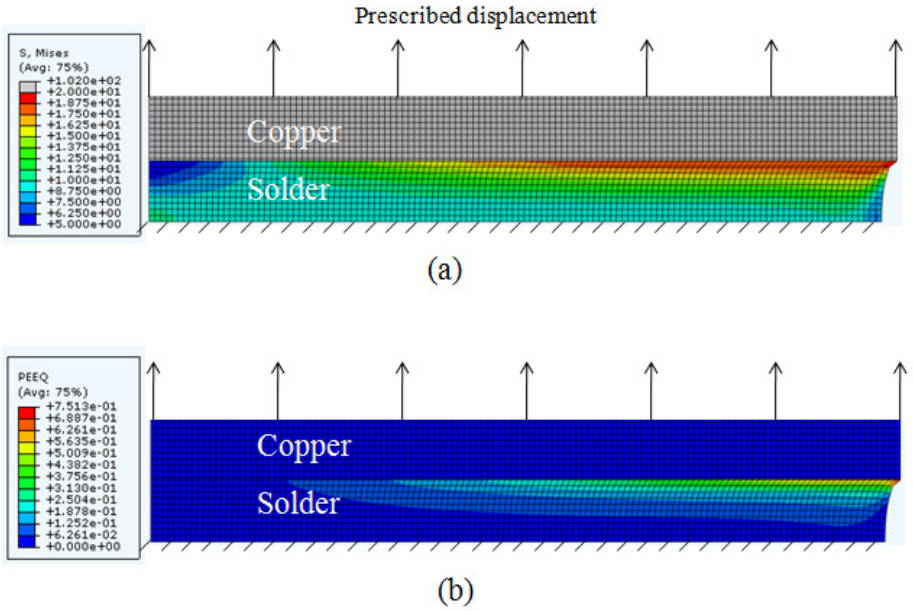


Figure 4.7. Finite element results of the effective stress and strain contours for a lead-free solder joint subject to uniaxial tension.

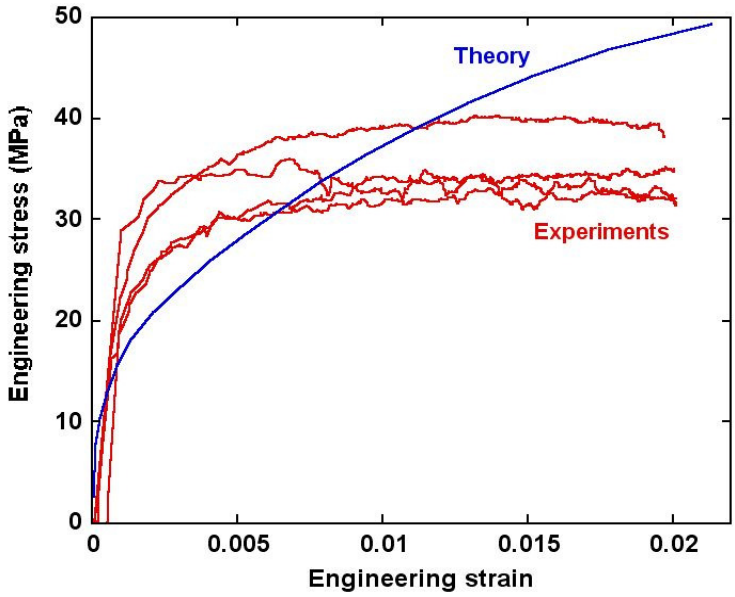


Figure 4.8. Stress-strain curve for a lead-free solder joint subjected to uniaxial tension for both theoretical analysis and experiments.

Figure 4.8 shows the stress-strain curve for both experiments and theoretical analysis. A fairly good agreement between experiment and simulation is observed. The simulation curve increases continuously, while the experiment

decreases more quickly. This can be attributed to the fact that a fracture criterion in the solder is not used, and that in the experiment fracture takes place by void growth in the Sn. These voids are nucleated by the nodular morphology of the IMC layer. A typical fracture surface is shown in Figure 4.9. Note that the nodules of $Cu_6Sn_5$ are at the base of the voids. A detailed discussion of plasticity fracture of the solder alloys will be seen in Chapter 5.

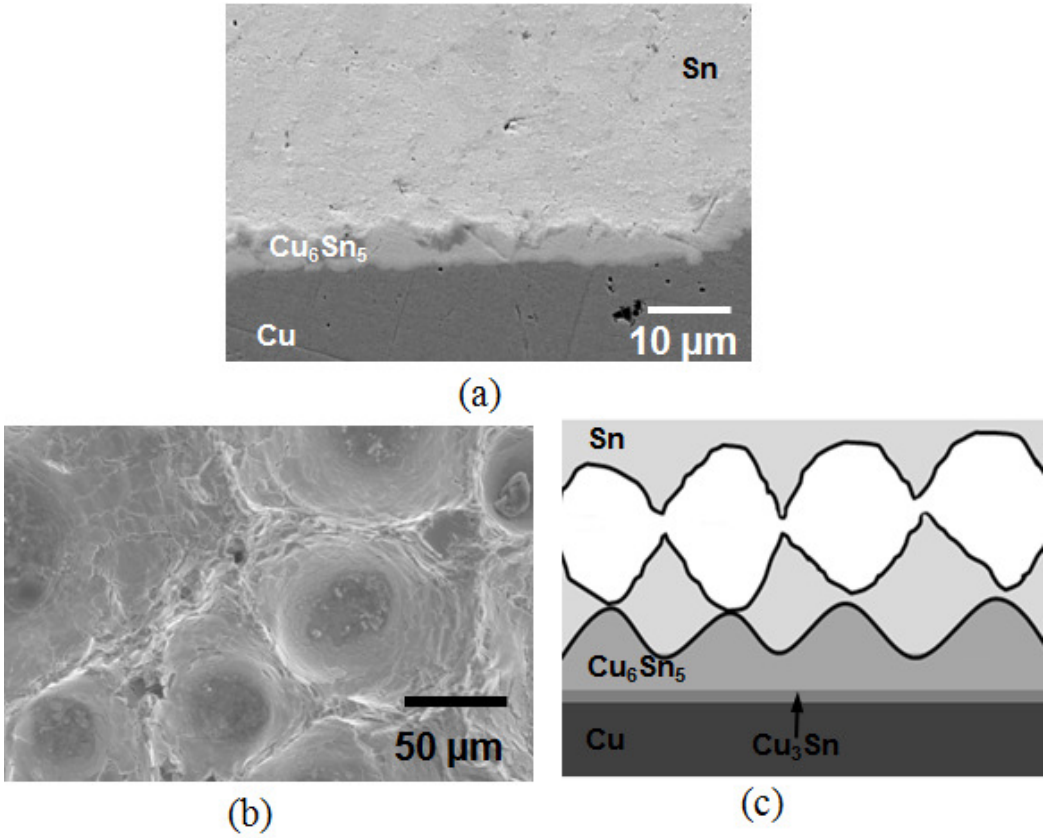


Figure 4.9. (a) Cross-section of untested joint; (b) Voids nucleated at tips of $Cu_6Sn_5$ nodules (top view); (c) Schematic side view of fracture mechanism. (Courtesy of K. Yazzie and N. Chawla)

## 4.5 Summary

In this chapter, we introduce an atomistic potential, the Modified Embedded Atom Method (MEAM). Then the MEAM is utilized to obtain the cohesive law for the interface between $Cu_6Sn_5$ and Sn. By converting atomistic relations to homogeneous continuum relation, an analytical interfacial traction-separation law for Sn/$Cu_6Sn_5$ interface is created, and the cohesive energy of the interface is also calculated. With the traction-separation law, both 2D and 3D cohesive fracture models are built and analyzed in ABAQUS. However, the theoretical analysis predicts that the interface has a greater cohesive energy compared with pure Sn and $Cu_6Sn_5$, which explains the reason why the facture, experimentally, always occurs in pure Sn or $Cu_6Sn_5$, other than the interface.

# CHAPTER 5

# MECHANICAL SHOCK BEHAVIOR OF PB-FREE SOLDER JOINT

## 5.1. Introduction

The mechanical performance and reliability of the solder joint are extremely important because solder joints must retain their mechanical integrity under various severe conditions [3, 18, 28, 29, 34, 35, 38, 39]. The understanding of the mechanism of joint failure cannot be overemphasized.

Very few reports to-date in the literature have delved into the microstructural mechanisms for fracture in Pb-free solder joints. The fracture mechanisms in Pb-free solder joints are quite complex due to: (a) the large difference in deformation behavior of the individual components, and (b) the many interfaces that are formed in the system. Generally speaking, the fracture in these joints can be categorized by solder-based fracture or IMC-controlled fracture. Chawla [1] notes that the type of fracture is likely a function of the applied strain rate and the thickness of the IMC layer. Higher strain rates and larger IMC thicknesses favor brittle fracture through the IMC. In many reports, fracture at or within the IMC layer is observed [111-113]. A recent report by Suh et al. [111] shows that by decreasing the content of Sn, more plasticity energy dissipation took place that enhanced the drop resistance by over a factor of ten in Sn-1Ag-0.5Cu compared to a conventional Sn-4Ag-0.5Cu. The fracture mode shifts from IMC failure in the higher content Ag material to that of failure within the solder at lower Ag content. Liu et al. [112] shows that solder aging decreased

the drop resistance of the solder joint, although it is not clear whether this is due to an increase in IMC thickness or a decrease in solder strength. Mattila et al. [113] studies the mechanical drop behavior of several solder and metallization combinations. They hypothesize that the main failure mechanism under mechanical shock loading is related to the high deformation rates and strain-rate hardening of the solder which forces cracks to propagate in the IMC layers instead of the bulk solder. Song et al. [114] examines the role of microstructure on the vibration fatigue properties of a Sn-rich solder alloy. Coarser eutectic regions with larger β-Sn dendrites contributed to a higher damping capacity and, thus, a greater vibration life. It is postulated that needle-like eutectic $Ag_3Sn$ and large primary $Ag_3Sn$ plates accelerate crack growth and, thus, degrade the ductility and vibration fracture resistance.

In previous chapters, we have investigated the macroscopic material behavior of bulk Pb-free alloys, material properties of micron-scale IMC and the atomistic-based cohesive law of the solder/IMC interface. In this chapter, the overall performance and fracture mechanisms of single solder joints will be investigated by using the constitutive relations obtained in previous chapters.

First, we will introduce an experimental observation of the crack surfaces of a Cu/Sn/Cu sandwich joint, which shows a large amount of voids in solder alloy. Then a porous plasticity model, namely Gurson-Tvergaard-Needleman model, will be applied to explain the nucleation, growth, and coalescence of microvoids in solder materials. A method to randomize the initial voids in the

solder is proposed. To investigate the solder-controlled fracture, we execute quasi-static analyses of solder with random microvoids. The fracture mechanism of the void-induced cracks is provided.

Then we improve our FE model by embedding brittle intermetallics in between solder and copper substrate. Plasticity fracture of the solder alloy and brittle fracture of the intermetallics are coupled in one model. The strain rate effect and intermetallic thickness effect are studied by a series of dynamic FEA simulations via ABAQUS/Explicit. Failure mechanism of the solder joints is investigated and theoretical explanation is provided.

## 5.2. Experiment Observation

Figure 5.1 shows a single sandwich joint of Cu/Sn/Cu tested in uniaxial tension. The joint is made of 99.99% pure tin (Sn) and oxygen-free high conductivity (OFHC) copper bars. The thickness of the pure Sn joint is 0.5 mm, and the diameter of cylindrical specimen is 6.35 mm, Figure 5.1c. Figure 5.1a is an optical micrograph of the side view of the joint before loading. Figure 5.1b are the scanning electron microscope (SEM) images of the fracture surfaces of the two specimens. The fracture surfaces on the left and right are opposing matching fracture surfaces. Clearly, there are a large number of voids on the fracture surface, and they are distributed randomly. We can also observe a fair amount of random initial voids from Figure 5.1a.

Many researchers [115-120] find that nucleation, growth, and coalescence of microvoids in metallic materials are important mechanisms in ductile failure. In

Pb-free solder alloys, particularly Sn-rich solders with Ag and Cu, second phase particles of $Ag_3Sn$ and $Cu_6Sn_5$ are present. These particles, which can be as large as tens of micrometers or as small as submicrometer in size, have been shown to nucleate voids [121-123]. Several investigators have conducted fractographic analyses that show a predominant distribution of voids, with the second phase particles at the base of these voids [124, 125]. In other cases, voids can be nucleated close to the $Cu_6Sn_5$ intermetallic compound (IMC) formed during reflow of the Sn-rich solder and Cu.

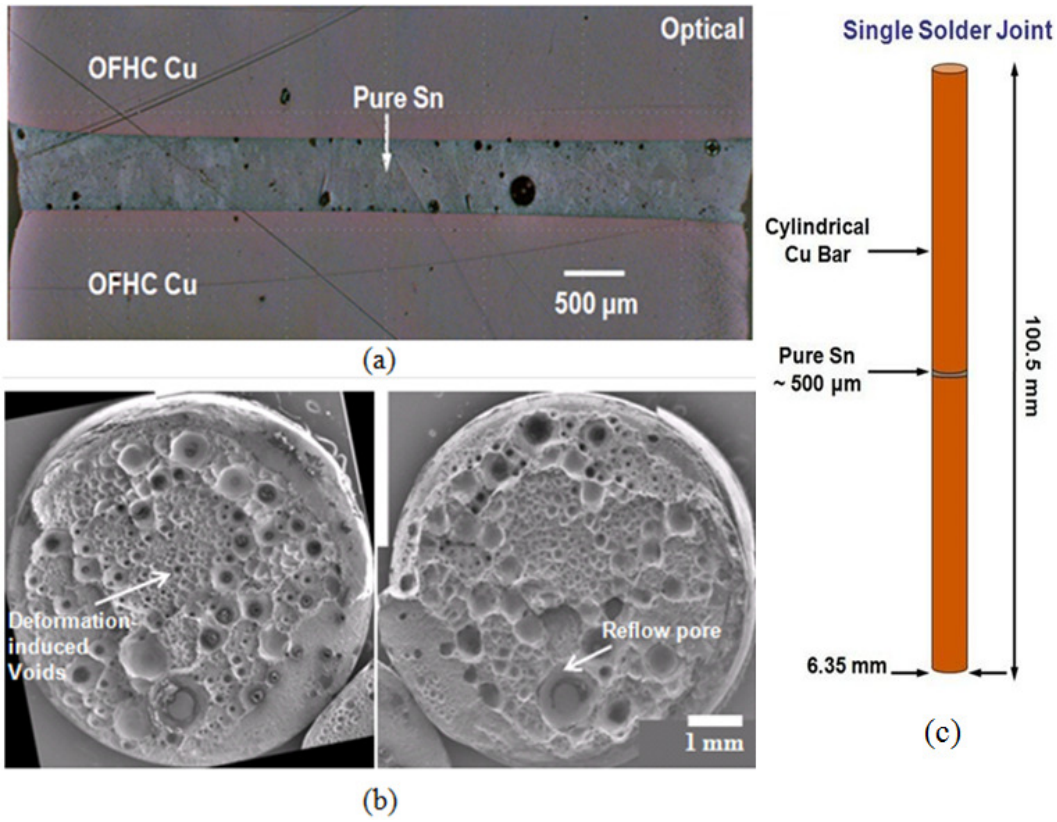


Figure 5.1. A sandwich joint of Cu/Sn/Cu. (a) Optical image of the side view of the joint. (b) Scanning electron microscope image of the crack surface. (c) The overall geometry of the single solder joint. (Courtesy of K. Yazzie)

Therefore, a theoretical description and predictive numerical model of ductile failure due to the incubation and coalescence of microvoids are of great interest.

## 5.3 Porous Plasticity Model

A proper porous plasticity model is desirable to characterize the void nucleation and coalescence, and crack propagation of the plastic solder alloys.

### 5.3.1 Review of Previous Work

Rice and Tracey [126] investigate the ductile enlargement of a single void in an infinite matrix, and propose that the void growth rate increases due to the hydrostatic stress $\sigma_{kk}$. Gurson [115] develops a porous plasticity model based on a unit cell with a single void in a finite matrix. Gurson [115] establishes a yield criterion for porous ductile metals that depends on, not only the von Mises effective stress $\sigma_e$ (as in conventional plasticity), but also the hydrostatic stress $\sigma_{kk}$ and void volume fraction $f$. Tvergaard and Needleman [117, 127-131] investigate the ductile crack growth based on the Gurson model, and modify and improve this model in order to account for plastic work hardening and damage evolution. This modified porous plasticity model is referred to as the Gurson-Tvergaard-Needleman (GTN) model or modified Gurson model, which is widely used in modeling microvoid-induced ductile fracture. The GTN model is included in the commercial finite element package ABAQUS as one of the plastic options to study the evolution of damage in metallic materials containing microvoids and to analyze ductile fracture. Recently, Wen et al. [132, 133] extends the GTN model

to account for the effect of void size, and observes that the yield surfaces for micrometer- and submicrometer-sized voids are significantly larger than that given by the Gurson model.

5.3.2 The GTN Model

The GTN model assumes a ductile metal matrix material either in fully dense form or with a small initial distribution of voids. Void volume fraction $f$ is defined as volume of voids divided by the total volume of the porous material. $f = 0$ describes a fully dense material and $f = 1$ represents a fully voided material. The GTN model proposes a yield surface given by [115, 127]

$$\phi = \left( \frac{\sigma_e}{\sigma_y} \right)^2 + 2q_1 f \cosh\left( -\frac{3q_2}{2\sigma_y} \sigma_{kk} \right) - (1 + q_3 f^2) = 0 \qquad (5.1)$$

where $\sigma_y$ is the yield stress of the matrix material, the three parameters ($q_1$, $q_2$, and $q_3$) are introduced by Tvergaard [127] to make the original Gurson model agree with numerical studies. Tervgaard [127] suggests that $q_1$ is dependent on the strain hardening behavior of the metal. For example, $q_1$ = 1.25 for $n$ = 20 and $q_1$ = 1.8 for $n$ = 5, where $n$ is the strain hardening exponent. It is also suggested that $q_2 = 1.0$ and $q_3 = q_1^2$. By setting the void volume fraction $f$ = 0, the GTN collapses to the classical $J_2$ theory, which use von Mises stress as yield condition. Figure 5.2 shows representative yield surfaces expressed as the relationship between normalized von Mises effective stress and hydrostatic stress for $q_1 = 1.8$, $q_2 = 1.0$ and $q_3 = 3.24$. One can clearly see that the yield condition depends on

both von Mises effective stress and hydrostatic stress and with the increase of void volume fraction, $f$, the material tends to yield at smaller von Mises stress and hydrostatic stress.

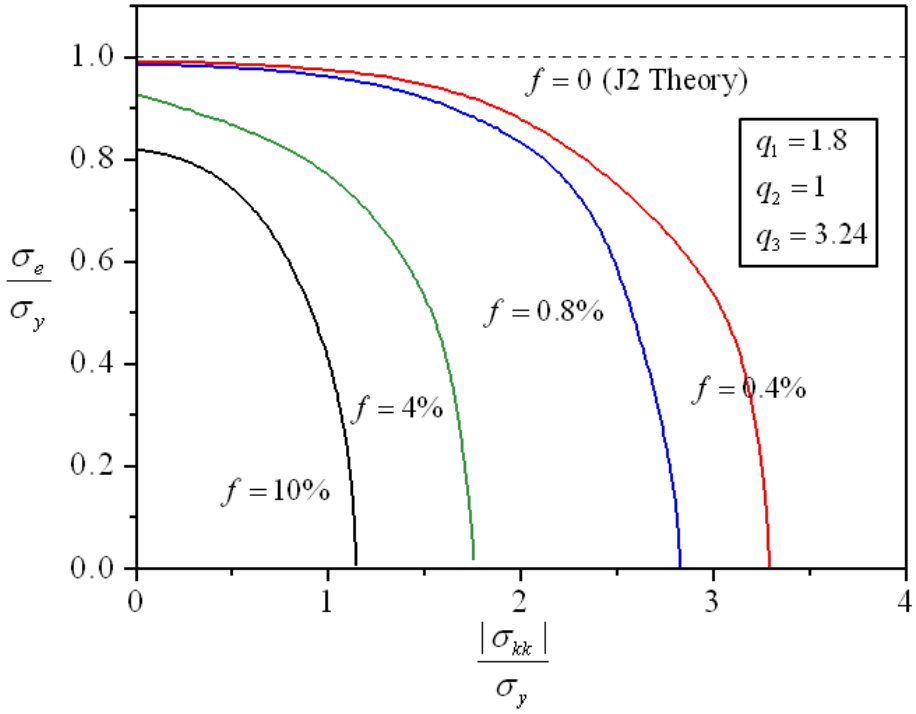


Figure 5.2. Schematic of the yield surface of the GTN model.

The evolution of the void volume fraction growth rate, $\dot{f}$ , has two contributions, namely, the nucleation rate and the growth rate,

$$\dot{f} = \dot{f}_{nucl} + \dot{f}_{gr} \tag{5.2}$$

where $\dot{f}_{nucl}$ changes due to nucleation of new voids and $\dot{f}_{gr}$ changes due to growth of existing voids. Chu and Needleman [129] assume that the nucleation of new voids is plastic strain-controlled and given by

$$\dot{f}_{nucl} = A\dot{\bar{\varepsilon}}_m^{pl} \tag{5.3}$$

where $A = \frac{f_N}{s_N\sqrt{2\pi}} \exp\left[-\frac{1}{2}\left(\frac{\bar{\varepsilon}_m^{pl} - \varepsilon_N}{s_N}\right)\right]$ is a normal distribution and $\dot{\bar{\varepsilon}}_m^{pl}$ is the rate of the equivalent plastic strain $\bar{\varepsilon}_m^{pl}$ of the material. Needleman and Rice [134] suggest that void nucleation may take place over a narrow range of nucleation strain, characterized by the mean value $\varepsilon_N$ and the standard deviation $s_N$. Usually, one can take $\varepsilon_N$ a strain value before the ultimate tensile strength (UTS) in stress/strain curve. $f_N$ is the upper limit of the total void volume fraction that can be nucleated, which is consistent with the volume fraction of second phase particles of the metal. The void growth rate is given by

$$\dot{f}_{gr} = (1-f)\dot{\varepsilon}_{kk}^{pl} \tag{5.4}$$

where $\dot{\varepsilon}_{kk}^{pl}$ is the rate of the volumetric plastic strain of the material. Eq. (5.4) was derived from the plastic incompressibility of the matrix material (not the material containing incompressible matrix and compressible voids).

5.3.3 Stochastic Model of Void Distribution

As the observation of random initial microvoids and fractured voids in Figure 5.1, it is necessary to be able to characterize the random nature of the void distribution.

Compared with classical metal plasticity, the GTN model introduces a new state variable, void volume fraction (VVF), *f*, in the constitutive relations. The randomness of the voids can be implemented via stochastic process of distributing initial void volume fraction to each element. The randomly assigned

initial void volume fraction obeys a certain type of random distributions, such as rectangular and Gaussian distributions. In order to handle large amount of elements, a C++ code is developed to generate and assign random initial void volume fractions to each element, based on the prescribed distribution of initial voids. The code generates a data file containing the initial VVF information, which will be incorporated into the input file for ABAQUS.

Here is an example of a random distribution of initial voids in a rectangular geometry. The initial VVFs (void volume fraction) ranges from 0.0001 to 0.01 are assigned to objective elements. Each element has an individual initial state, and we can increase the resolution of the randomness by refining the mesh. At each running, the C++ code will generate a new random set, as shown in Figure 5.3. This feature makes it possible to vary the microstructure of the solder while keeping the geometry and intermetallic thickness/shape unchanged, which is very challengeable in experiment.

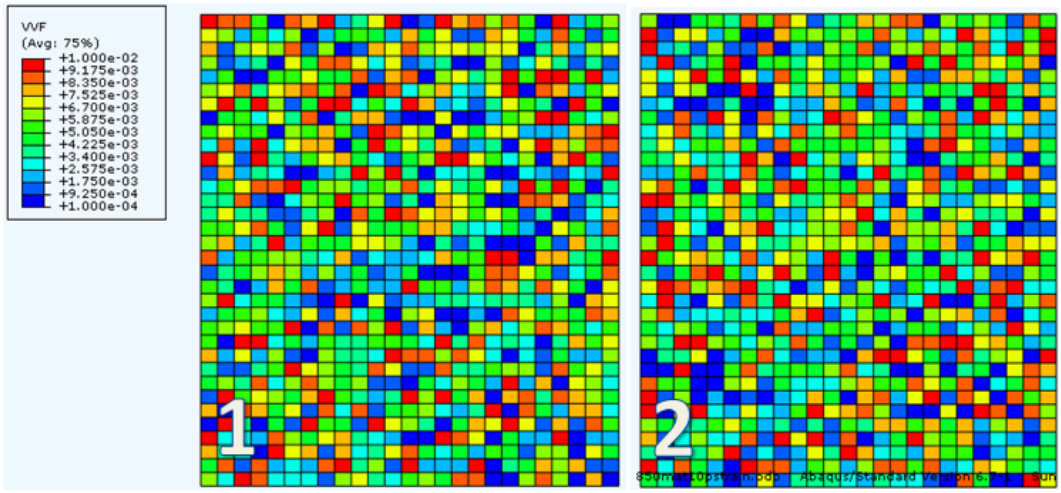


Figure 5.3. Two random sets of initial VVF for a rectangular geometry.

This stochastic approach can also be applied to materials with a random nature, such as defects, grain size, and crystallographic orientation, etc.

## 5.4 Sandwich Model of Solder Joint without intermetallic

As mentioned above, the solder-controlled fracture takes place mostly at low strain rate with a thin intermetallic layer. Thus, we begin with a simple model without intermetallic layer, and focus on failure in solder region at low strain rate. This simple model includes Cu bars and pure Sn solder. Cu is modeled as elastic metal, and Sn as the porous plasticity. Our main interest is to characterize the stress/strain response and failure mechanism of the solder segment.

### 5.4.1 Finite Element Model

The geometry of the experiment sample is a cylindrical rod as shown in Figure 5.1c. A 2D axisymmetric model is sketched to represent the original 3D cylinder. Figure 5.4 illustrates the geometry and boundary conditions of the of copper/tin/copper sandwich model.

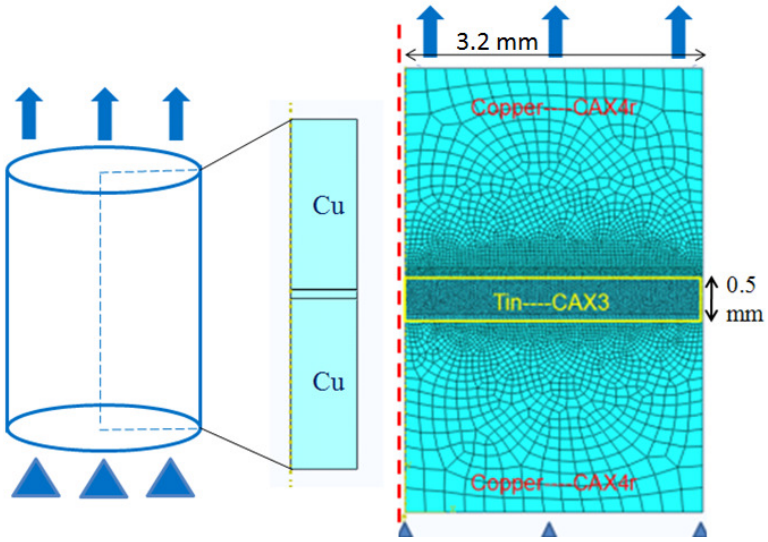


Figure 5.4. Axisymmetric geometry and boundary conditions of the sandwich model of solder joint without intermetallic.

The Sn part is 0.5 mm in thickness and 6.35 mm in diameter. Axisymmetric elements are used, namely CAX4R (4-node axisymmetric element with reduced integration) for copper and CAX3 (3-node axisymmetric element) for Sn. The symmetric boundary condition is applied on the symmetry axis (red dash line in Figure 5.4) and the bottom of the copper have a fixed displacement along the vertical direction. The prescribed displacement boundary condition is applied at the top of the copper in the vertical direction. Mesh convergence is examined by varying the element numbers of pure Sn, and finally the simulations used 8000 CAX3 elements in pure Sn. All the FE simulations are quasi-static with applied displacement, using ABAQUS/Standard.

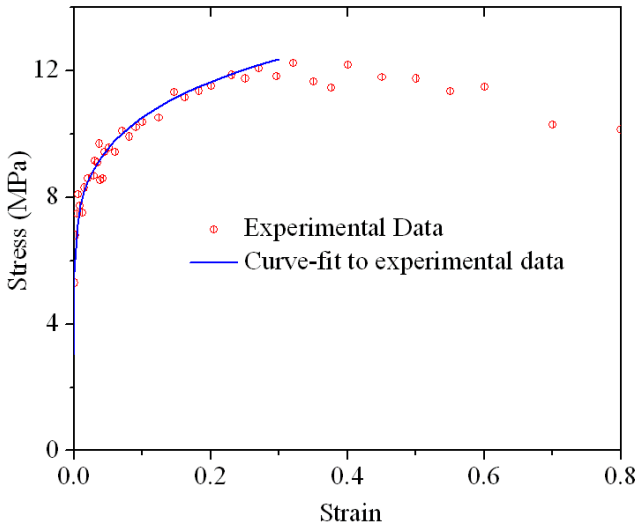


Figure 5.5. Stress-strain curve of pure Sn measured at strain rate 0.001/s.

Copper is modeled as an elastic material with Young's modulus, $E$ =116.5 GPa, and Poisson's ratio of $\nu$ =0.34. Sn is modeled as a GTN plastic material with a random initial void volume fraction. The elastic modulus of Sn is $E$ = 46.9 GPa and Poisson's ratio is $\nu$ = 0.36 [122, 135]. The experimentally measured

stress-strain curve of pure Sn at strain rate 0.001/s is given in Figure 5.5 (red dots), which is used as the plastic portion of the curve for the quasi-static analysis.

To best fit the stress-strain curve, the strain hardening index is obtained as $n = 5$. In the finite element analysis, we only use the hardening part (blue curve in Figure 5.5), up to the ultimate tensile stress (UTS). The three parameters in the yield surface (Eq. (5.1)) are taken as $q_1 = 1.8$, $q_2 = 1.0, q_3 = 3.24$ for $n$ =5 based on Tvergaard [127]. The mean value of the nucleation strain is taken as $\varepsilon_N = 0.1$, (less than the strain at UTS, 0.3) and the standard deviation is set to $s_N = 0.02$; the upper limit of the total void volume is taken as $f_N = 0.01$. It must be noted that although the aforementioned parameters are empirical, the simulation results based on these empirical values qualitatively captured the failure process of pure Sn joint.

The following method is used to calculate the stress and strain in Sn segment. Before necking, the stress state is uniaxial so that the nominal normal stress $\sigma$ was calculated by the reaction force at the loading point (i.e., top of the copper) divided by the original cross-sectional area. The strain in Sn was calculated by the height change of the Sn part divided by the original height of the Sn. By this means, the effect of copper length is minimized. It should be noted that, to be neat and clear, most of the contours/plots in this chapter only show solder (and intermetallic), and the copper part is excluded.

5.4.2 Radom Initial Void Volume Fraction

In this section, we will consider how the initial void volume fraction affects the fracture path. We compare three situations as shown in Fig. 5.6, in which the contour plots are for void volume fractions (VVF). Figure 5.6a shows a case with a uniform initial void volume fraction throughout all elements in the Sn segment. Figs. 5.6b and 5.6c show two cases with randomly distributed initial void volume fractions in Sn.

A rectangular distribution is used to generate the randomly distributed initial voids for Figs. 5.5b and 5.5c. The rectangular distribution is defined by two parameters $a$ and $b$, which are its minimum and maximum values. The initial void volume fraction of each porous element is of equal probability to be any number in the closed interval $[a, b]$. In our case, the average initial void volume fraction of the randomly distributed voids is taken as $f = 0.8\%$ and the range of variation of initial VVF is from 0.3% to 1.3%.

The randomness of the initial void volume fraction can be observed in Figs. 5.6b and 5.6c. After deformation, the three cases exhibited different fracture paths as shown in Figures 5.6d, 5.6e and 5.6f. Because of the randomly distributed initial void volume fraction, the localizations of void nucleation and growth are also random, which led to different fracture patterns.

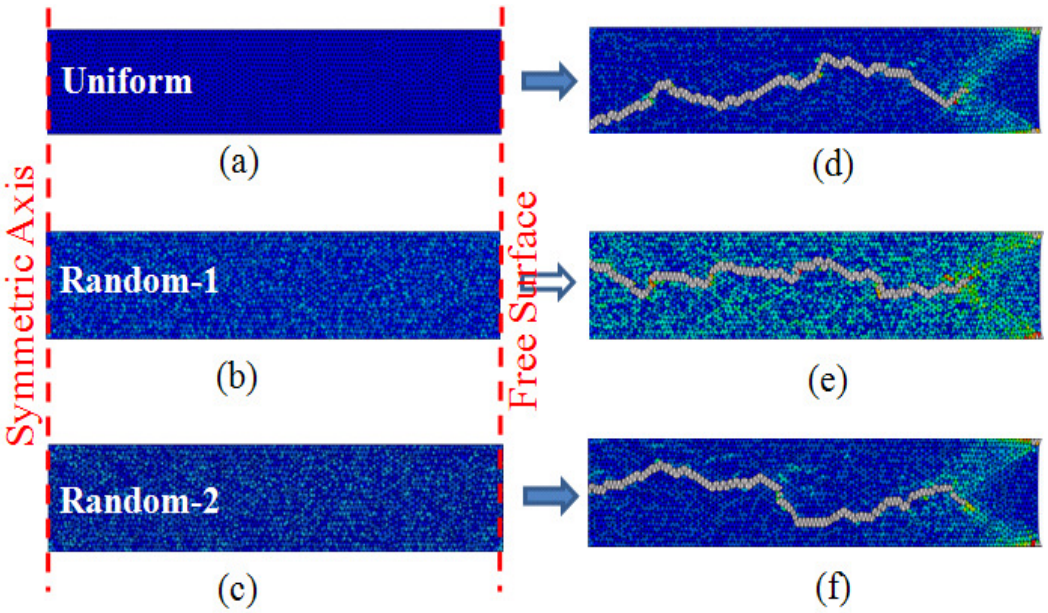


Figure 5.6. Contours of void volume fraction of solder zone. Dependence of crack path on the randomness of initial void volume fraction of solder.

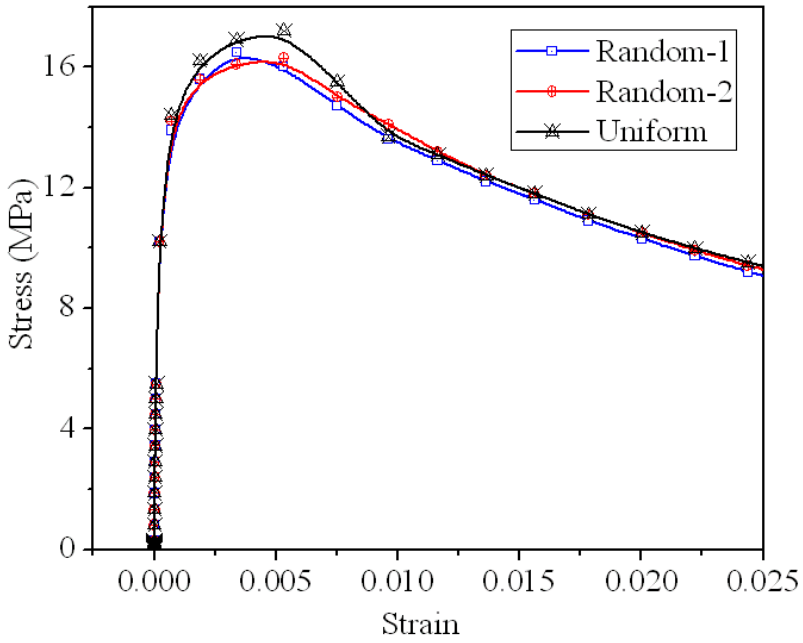


Figure 5.7. Macroscopic stress/strain behavior of the tin segment with uniform and random distributed voids.

Figure 5.7 compares the macroscopic stress/strain response of the Sn segment for the three cases in Figure 5.6. It is found that almost identical

macroscopic stress/strain responses (both hardening and softening) are obtained for the three cases (Figs. 5.5a-5.5c). This coincidence suggests that, by considering the randomly distributed voids in the GTN model, local microstructure details and their effects on the fracture paths can be gleaned, while the macroscopic stress/strain behavior of the solder joint remains unchanged.

It should be noticed that the softening segments of the output curves result from the increase of the void volume fraction, since the input has only the hardening segment (as shown in Fig. 5.5 blue curve). This observation qualitatively agrees with experiments in which different specimens prepared under the identical conditions may have different cracking paths but exhibit very similar macroscopic stress/strain curves.

### 5.4.3 Mechanism of Void Nucleation and Growth

In all aforementioned simulations of solder joint with random initial VVF, we find that all cracks initiate at the symmetry of axes and propagate towards the free surface of the cylindrical bar, even though the crack paths are different. We also observe this common phenomenon of the crack initiation and propagation in other complementary simulations with various random configurations.

Figure 5.8 provides a schematic of failure process due to voids nucleation and propagation. Voids can nucleate because of particle cracking or interfacial failure between precipitates and the matrix. Newly nucleated voids and/or existing voids coalesce when adjacent voids link together or the matrix material between

them experiences necking. The void coalescence leads to crack initiation and propagation, and finally fracture.

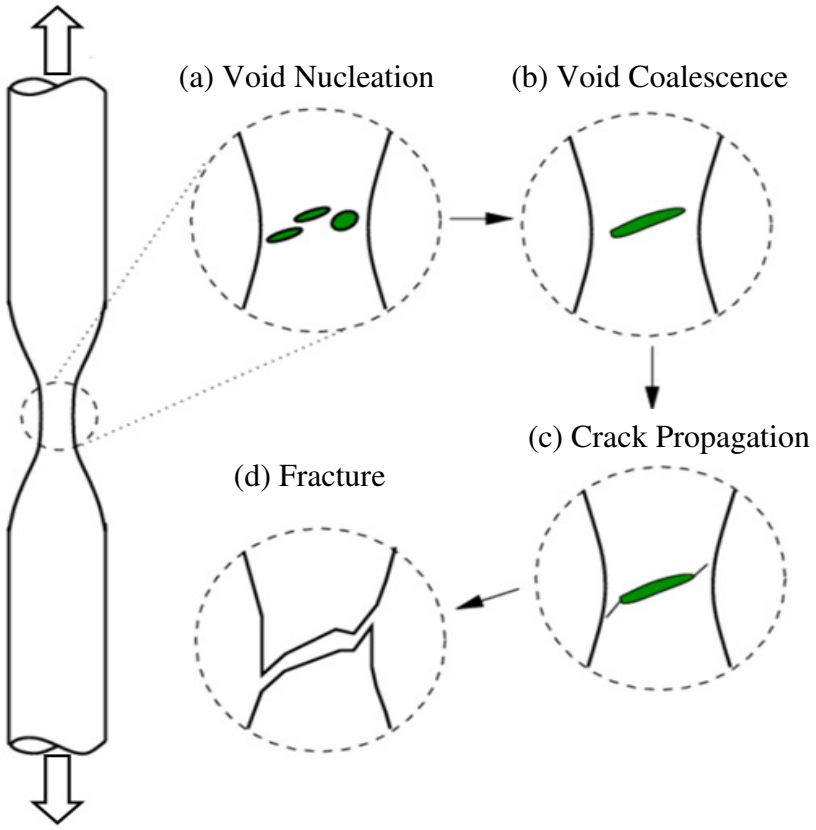


Figure 5.8. The schematic of failure process due to voids nucleation and propagation. The micro cracks always initiate inside the solder.

As tensile load increases, the stress and the plastic strain increase which in turn lead to the increase of the void volume fraction. In the yield surface given by Eq. (5.1), for a given void volume fraction, the yield condition is determined by two quantities, von Mises effective stress $\sigma_e$ and the hydrostatic stress $\sigma_{kk}$. Here a compressive hydrostatic stress is considered negative and the hydrostatic stress under tension is defined positive. Figure 5.9 shows the von Mises effective stress $\sigma_e$ and the hydrostatic stress $\sigma_{kk}$ in the Sn segment along the radial direction.

The von Mises stress along the radial direction does not change significantly. On the contrary, the hydrostatic stress drops significantly at the vicinity of the free surface. Based on the yield surface given by Fig. 5.2, the elements close to the symmetry axis (with larger hydrostatic stress, e.g. location #1 in Figure 5.9) will yield first, followed by the elements close to the free surface (with smaller hydrostatic stress, e.g. location #2 in Figure 5.9). Once the element yields, the void volume fraction starts to increase as characterized by Eqs.(5.2), (5.3) and (5.4). Fracture occurs once the void volume fraction reaches its critical value, 50%.

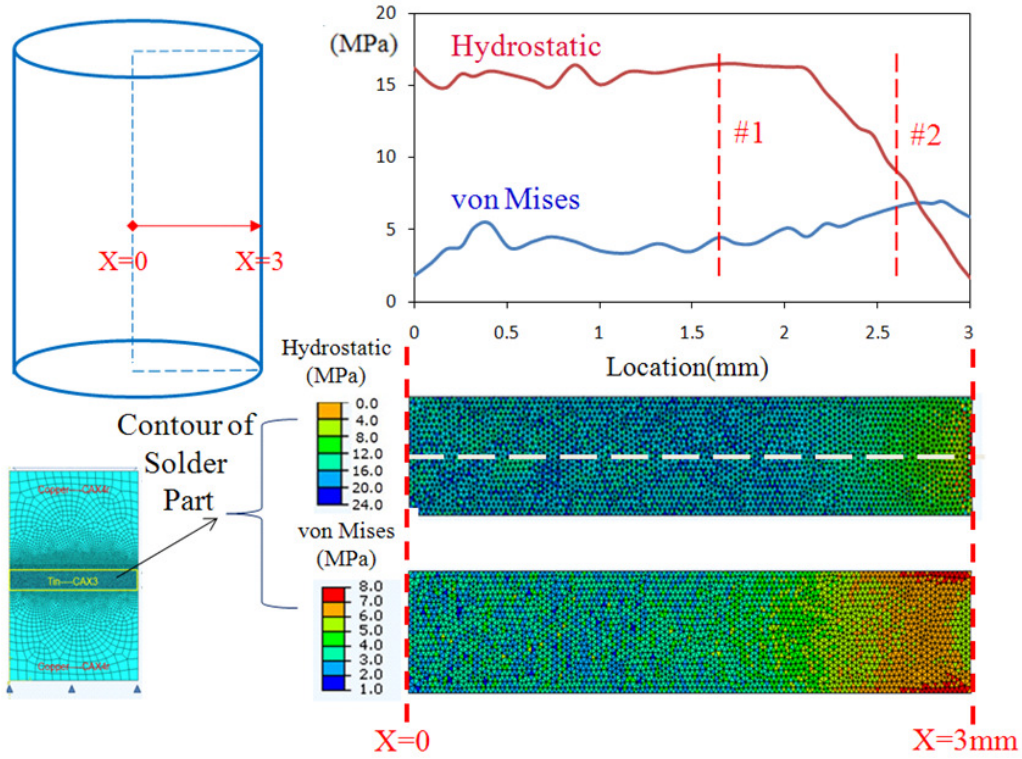


Figure 5.9. The variation of hydrostatic stress and the von Mises effective stress along the radial direction of the pure Sn segment.

5.4.4 Effect of Random Distribution Range

The default random distribution used in this chapter is rectangular distribution, which is also called continuous uniform distribution. The rectangular distribution is defined by two parameters $a$ and $b$, which are its minimum and maximum values. The initial void volume fraction of each porous element is of equal probability to be any number in the closed interval $[a, b]$. The integral of probabilities of all variables in $[a, b]$, so the probability density function for every single node in this interval are $1/(b-a)$.

In this section, we investigate the effect of the range of the rectangular distribution on the macroscopic stress/strain behavior. Figure 5.10 shows three cases that have the same average initial void volume fraction 0.8% but different ranges of normal distribution, from 0 ~ 1.6%, 0.3% ~ 1.3%, and 0.6% ~ 1.0%, along with a uniformly distributed initial void volume fraction of 0.8%.

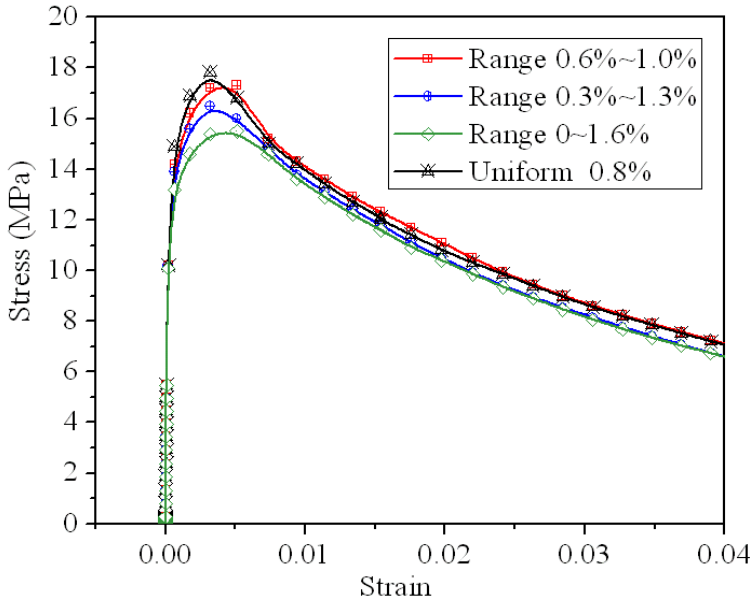


Figure 5.10. Effect of the range of random distribution on the macroscopic stress/strain behavior.

It is found that the different ranges do not affect the overall stress/strain curve very much but it did affect UTS. Specifically, the uniform case have the highest UTS and the case with the widest range (i.e., 0 ~ 1.6%) shows the smallest UTS. This is because the overall stress/strain behavior is determined by the total voids content in the material. Thus, for all four cases, regardless of the distribution, they exhibit similar macroscopic behavior. It should be noted that a much larger range of voids may have elicited different results, i.e., had a more profound effect on the deformation behavior. However, the UTS of the material is determined by the localization of the voids: Larger voids give smaller UTS, which explains that the case with the widest range of initial void volume fraction have the smallest UTS.

5.4.5 Effect of Random Distribution Type

Actually, we have no solid evidence to verify which type of void distribution is inside the solder. Besides rectangular distribution, we have also tested another well-known probability distribution, Gaussian distribution, which is also known as normal distribution. Different from rectangular distribution which has an even probability density, Gaussian distribution describe real-valued random variables that tend to cluster around a single mean value. The probability density of Gaussian distribution is as follows,

$$f(x) = \frac{1}{\sqrt{2\pi\sigma^2}} \exp\left( -\frac{(x-\mu)^2}{2\sigma^2} \right) \tag{5.5}$$

where $\mu$ is the mean value (location of the peak), and $\sigma$ is the standard deviation, which is the measure of the width of the distribution.

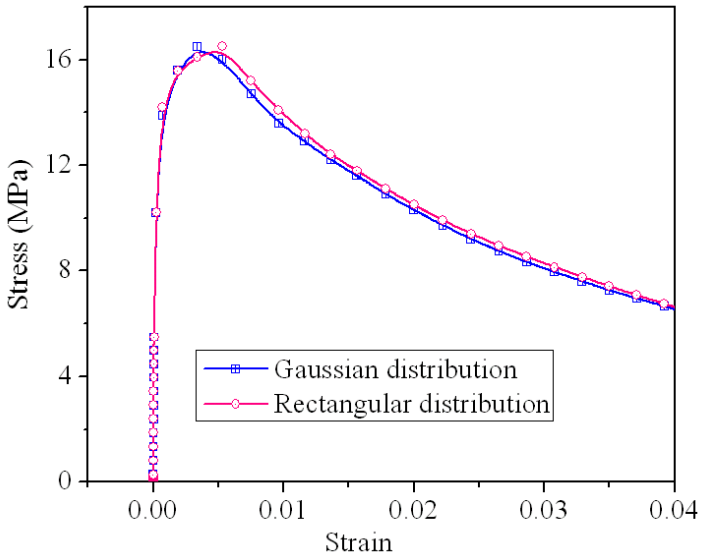


Figure 5.11. Effect of the type of random distribution on the macroscopic stress/strain behavior.

Figure 5.11 shows the stress/strain response curves of FEA results for rectangular and Gaussian distribution. The average initial void volume distribution is taken as 0.8% and the range for the rectangular distribution is 0.3% ~ 1.3% and the standard deviation of the Gaussian distribution is 0.02. The results suggest that the macroscopic stress/strain behavior is not sensitive to the distribution types, which is similar to the observation of Fig. 5.10, i.e., that the macroscopic stress/strain behavior is mainly determined by the total voids of the materials. More explicitly, the macroscopic stress/strain behavior represents the overall load bearing capability which is related to the total fraction of voids. Since the two distributions have comparable average and maximum voids volume fraction, the macroscopic stress/strain behaviors are similar.

## 5.5 Sandwich Solder Joint Model with Intermetallics

The nature of the interfacial products formed between solder and substrate greatly influences the thermomechanical behavior of the solder joint [59-61]. In this section, the intermetallic fracture is considered, coupling with the porous plasticity fracture of the solder. As mentioned above, the type of fracture is likely a function of the applied strain rate and the IMC thickness [1]. Therefore, the strain rate effect and IMC thickness effect are investigated for the coupled fracture model.

### 5.5.1 Finite Element Model

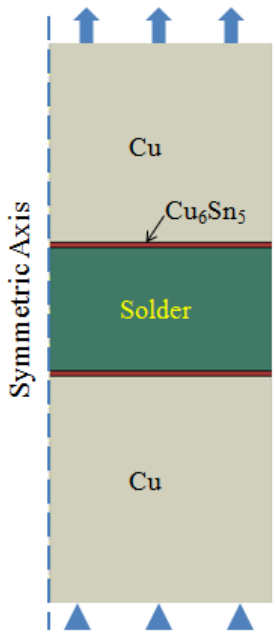


Figure 5.12. Symmetric geometry of sandwich joint model with intermetallic.

The intermetallic $Cu_6Sn_5$ layers (dark red regions in Figure 5.12) are added in between solder and copper substrate. The solder is 0.5 mm in thickness and 6.35 mm in diameter. Axisymmetric elements are used, namely CAX4R (4-node

axisymmetric element with reduced integration) and CAX3 (3-node axisymmetric element). The symmetric boundary conditions are applied in the symmetry axes and the bottom of the copper has a fixed displacement along the vertical direction.

The solder alloy is modeled as porous plasticity, which has been explored in section 5.4. The interface between solder and intermetallic is considered as a perfect bond, as it's been proved in Chapter 4 that the interface itself is stronger than solder and intermetallics. The intermetallic $Cu_6Sn_5$ is modeled as brittle material, which has been discussed in section 3.5. Young's Modulus is 112GPa. Direct cracking fracture strain is 1.21%, and fracture stress is 1356 MPa. Failure strain is 1.37%. Shear retention is described by power law retention in ABAQUS, and the power is set to 2. Thus, in this model, two materials, solder and intermetallic, are possible to fracture.

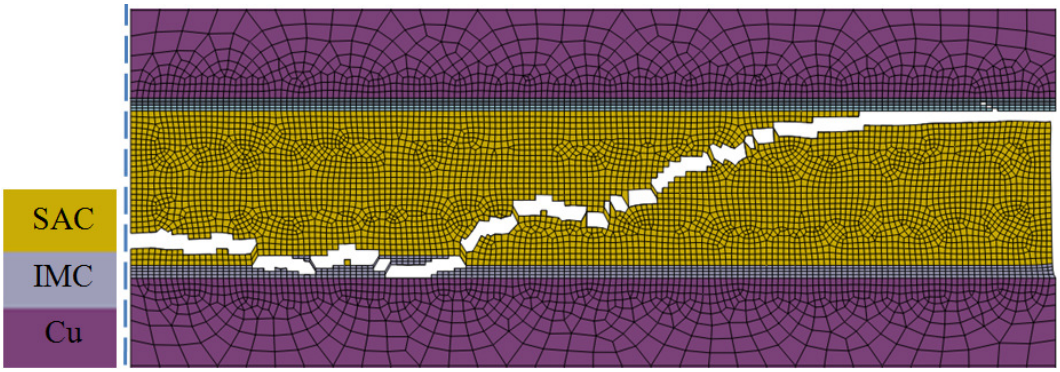


Figure 5.13. Fracture pattern of solder joint with intermetallic at strain rate of 30/s.

First, the coupled fracture model of the porous plastic solder and the brittle intermetallic is demonstrated via a trial simulation example. In Figure 5.13, the thicknesses of $Cu_6Sn_5$ and SAC are 0.05 mm and 0.5 mm, respectively. The solder used in this case is water-quench SAC, and material properties of SAC are shown

in Figure 2.8. The simulation is conducted by ABAQUS/Explicit. Tensile velocity (displacement rate) along axial direction is applied, and strain rate is 30/s.

In Figure 5.13, the yellow zone is SAC, the grey-purple is intermetallic, and the purple zone is the copper substrate (only part of it is shown). The fracture path is clearly shown. The crack path crosses both solder and IMC regions. In this example, both porous plasticity and brittle fracture contribute to the fracture; however, it's not always the case. Sometimes fracture only takes place in solder region, and sometimes intermetallic fracture dominates. Many factors affect the failure of the intermetallics, such as the shape and thickness of the intermetallics, defects in the intermetallics, strain rate, etc.

### 5.5.2 Intermetallic Thickness Effect

Preliminary reports indicate that the intermetallic thickness may be directly related to the mechanical shock resistance of the joint [21]. In this section, we will vary the intermetallic thickness while maintaining the microstructure and material property of the solder. To mimic the real shape of the intermetallic layer, a wavy interface between solder and intermetallic will be used, as shown in Figure 5.14.

The prescribed load is applied at the top of the copper in the vertical direction, and the strain rate is 30/s. About 25000 CAX3/CAX4R elements are used in the symmetric model. Dynamic analyses are conducted via ABAQUS/Explicit. We find that, if we set the $Cu_6Sn_5$ as a homogenous brittle material, the cracks occur only in the solder region. The straight-forward reason is

that the fracture stress of $Cu_6Sn_5$ (1,356 MPa) is way higher than the yield stress of Pb-free solders which is typically less than 100MPa (Figure 2.8).

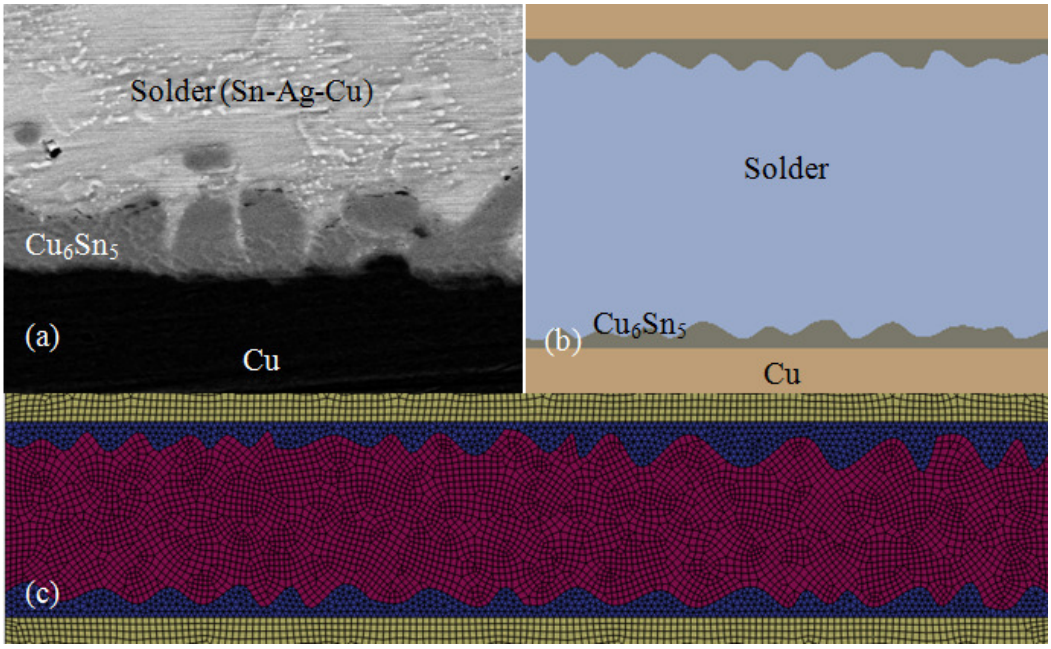


Figure 5.14. (a) The experimental image of intermetallics of SAC; (b)FEA model with the wavy shpae intermetallics; (c) Mesh of the SAC and IMC regions.

To solve this problem, we need to re-examine the material property of $Cu_6Sn_5$. The value 1356 MPa is measured from the single-crystal nodules of $Cu_6Sn_5$ under micro-compression [12]. First, the tension and compression behaviors are different for brittle materials. Second, the material property of intermetallic differs significantly in terms of grain size, defects and crystallographic orientations, which reduce the overall fracture stress of the intermetallic. Based on above two reasons, we can claim that the local fracture stress of $Cu_6Sn_5$ layer is less than that of the single-crystal nodules of it.

Due to the random nature of grain size, defects and crystallographic orientations of the intermetallic, we propose a stochastic method, which is similar

to the one we create for the GTN model in section 5.3. Elements of $Cu_6Sn_5$ are randomly categorized into couple of groups, and each group has its unique fracture stress and strain to failure, which are lower than the single-crystal compression case. The portion of lower fracture stress (empirically 400 ~ 600 MPa) can be controlled, which in our case is 20% ~ 60% of the total number of $Cu_6Sn_5$ elements. The $Cu_6Sn_5$ elements with lower fracture stress are called vulnerable elements, and the percentage of these elements to the total amount of elements is called vulnerable portion. By this means, the mechanical behavior of $Cu_6Sn_5$ is properly represented, and crack in the IMC region is successfully observed in Figure 5.15 (only the IMC and solder regions are shown).

To isolate the effect of vulnerable portion of intermetallics, we fix the mesh density, interface shape, loading condition and initial VVF distribution of the solder (in other words, solder microstructure), and only vary the vulnerable portion, ranging from 0% to 60% with a 20% interval. Figure 5.15a is the fracture pattern with perfect $Cu_6Sn_5$ single crystals, and all the cracks are in the solder region. Figures 5.15 b, c & d are fracture patterns of three cases with vulnerable portion of 20%, 40% and 60%, respectively. From contour (a) to (d), it is a very clear trend that more and more cracks initiate in the intermetallic region, when the vulnerable volume increases.

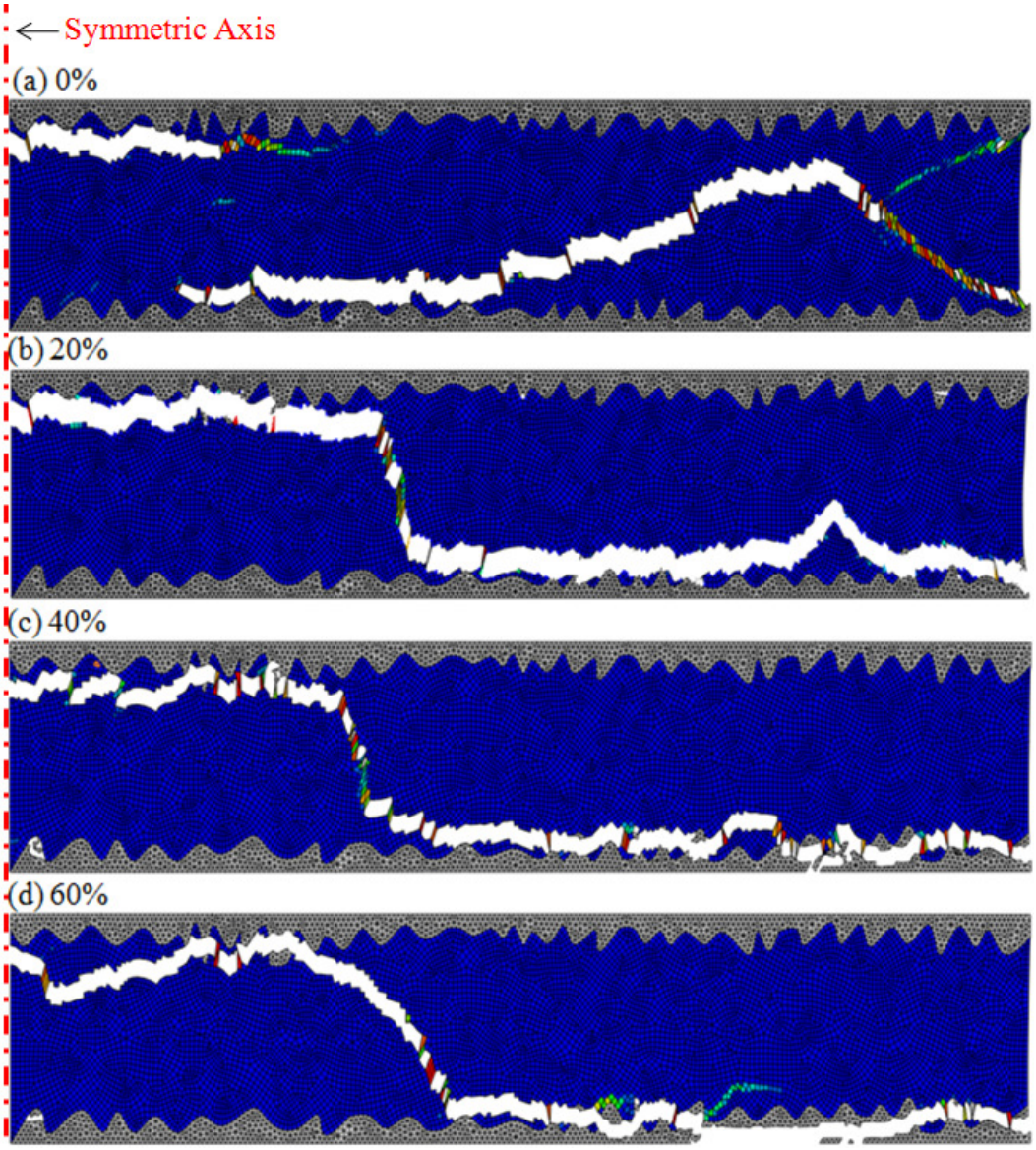


Figure 5.15. Effect of vulnerable portion of IMC on fracture patterns.

By comparing Figure 5.15 and Figure 5.6 (fracture patterns of joint model without IMC), we find that the void-induced cracks of the solder tend to be closer to the IMC layer, when the IMC fracture mechanism is introduced into the system. If there is no IMC layer in the model (Figure 5.6), the cracks are mostly in the

center of the solder. This observation of cracks close to the Solder/IMC interface has a good agreement to the experiments.

Although the aforementioned vulnerable portions are empirical, the simulation results based on these empirical values qualitatively captured the failure process of solder joint with intermetallic.

To isolate and validate the intermetallic thickness effect, the vulnerable portion will be fixed to 50% for the following FEA simulations, and the configuration of initial void volume fraction for the solder also keeps unchanged. Four IMC thickness are investigated, $10\,\mu m$, $40\,\mu m$, $80\,\mu m$ and $120\,\mu m$. Figure 5.16 illustrate the simulation results of IMC thickness effect. The blue part is the solder, the grey part is the IMC and copper, and the white strip is the fractured region. In Figures 5.16a&b, the IMC layer is relatively thin, and the cracks are mostly in the SAC region. When the IMC thicknesses are large in Figure 5.16c&d, there are cracks in IMC zone. In Figure 5.16d, where the thickness is $120\,\mu m$, a long crack crosses almost half of the solder joint at the top right corner of the IMC region.

Considering defects, grain size and crystallographic orientations in the IMC layer, a thin layer of intermetallic is more likely to be coherent than a thick one, so the thin IMC layer is more likely to carry a high fracture stress, i.e. 1356MPa. In other words, a relatively thin layer of intermetallic compounds may contribute to enhance the mechanical and chemical bond between Sn-rich solder and Cu substrate [60]. And when the intermetallic layer is thicker, it will serve as

a crack initiation site, leading to poor toughness of the joint, because of its brittle nature [58, 59, 63].

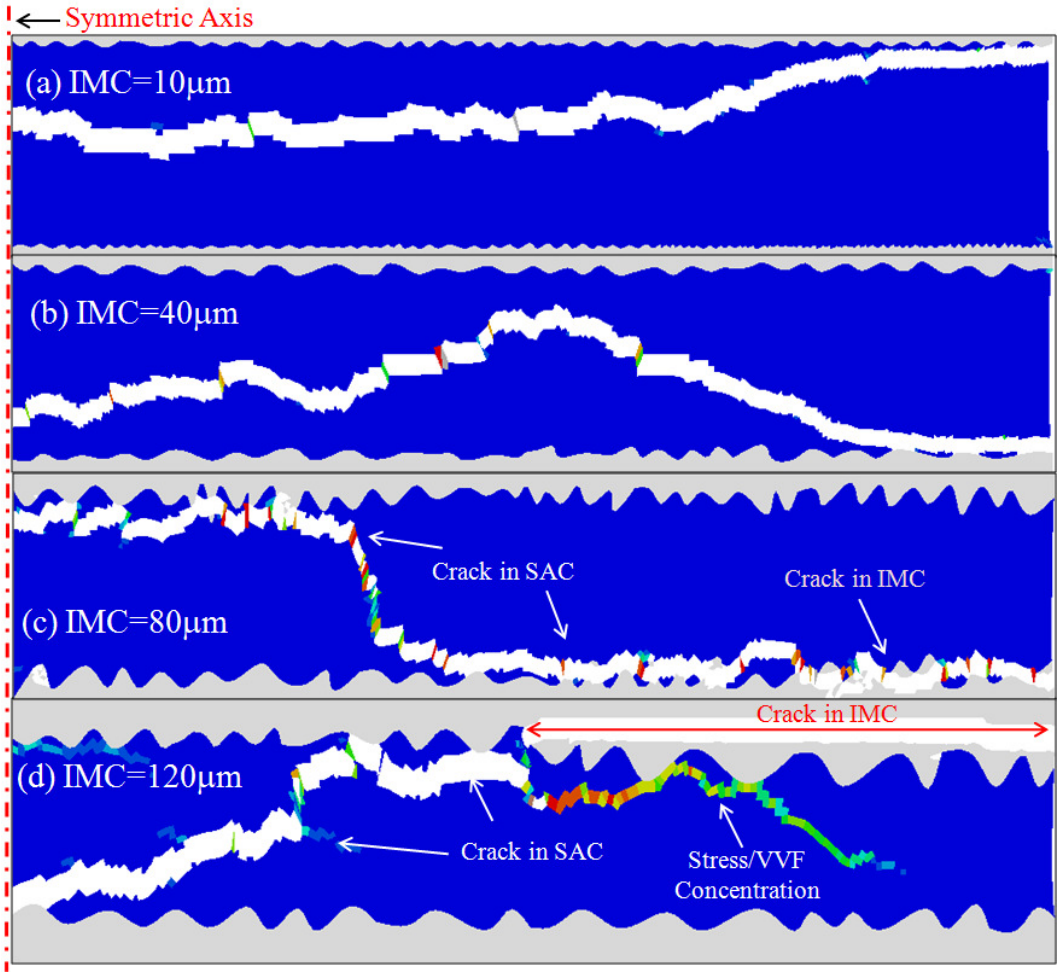


Figure 5.16. Contour of Void Volume Fraction and crack path of three cases with different average intermetallic thickness, i.e. (a) 10μm, (b) 40μm, (c)80μm and (d) 120 μm.

5.5.3 Strain Rate Effect

All the simulations in section 5.5.1 are conducted under the strain rate of 30/s. In Chapter 2, we have discussed the rate dependency of the Pb-free Sn-rich solder alloys. The higher the strain rate is, the stiffer the material is (Figure 2.8).

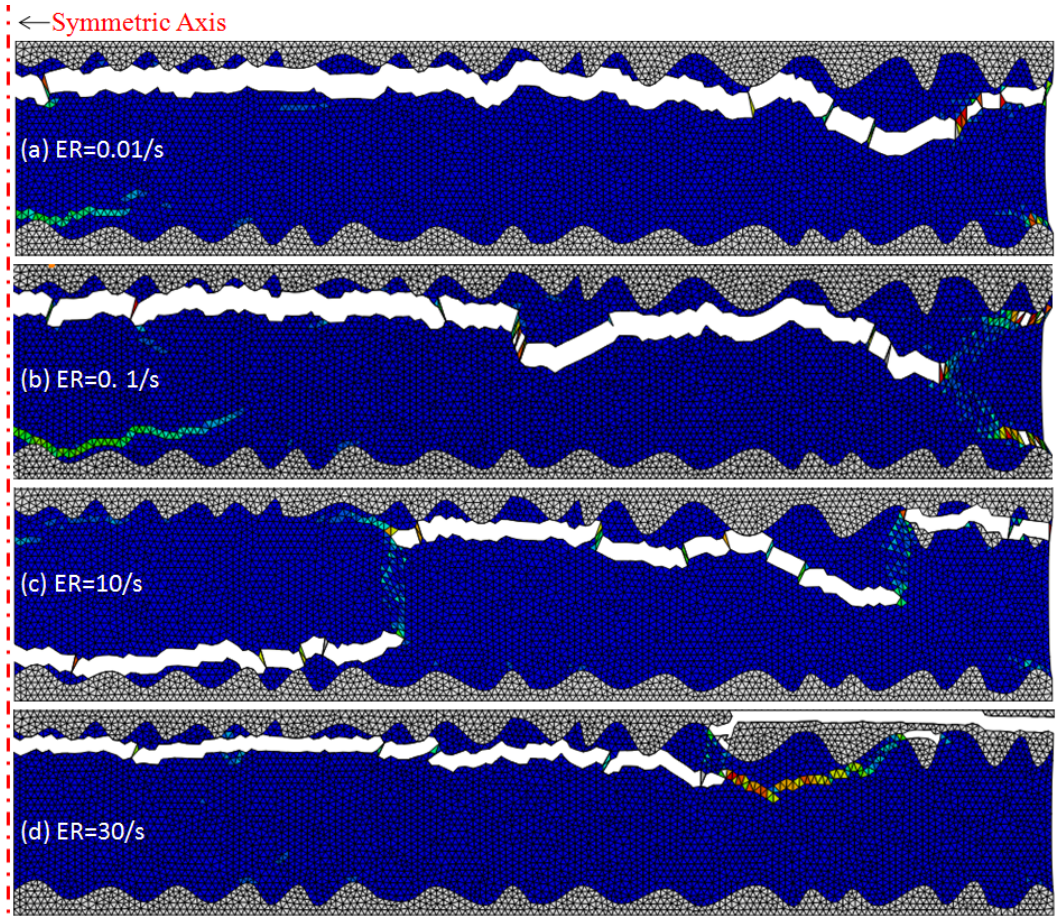


Figure 5.17. Crack patterns of SAC solder joints with a 0.1mm-thick intermetallic layer at different strain rate.

To study the strain rate effect, we conduct a series of FEA simulations, via ABAQUS/Explicit, with varying strain rate but same geometry, same intermetallic thickness/shape, and fixed initial void volume fraction of the solder. Velocity loadings are applied to control the strain rate, based on Eq. (2.1). Figure

5.17 shows the crack patterns of SAC solder joints at varying strain rates. The thickness of $Cu_6Sn_5$ is fixed to 100 micron. Based on finite element analysis of the joint tension, we find that at low strain rate, the crack tends to initiate and propagate inside solder. While at high strain rate, the crack also takes place in both the IMC layer and SAC region. The reason is that the $Cu_6Sn_5$ is much stiffer than water-quench SAC, or any other Sn-based solder alloys. At quasi-static state or low strain rate, the solder yields and fails before $Cu_6Sn_5$ reaches its failure criterion. However, at high strain rate, there is a chance that $Cu_6Sn_5$ reaches its failure criterion first, due to the strain rate hardening effect of the solder alloy [9].

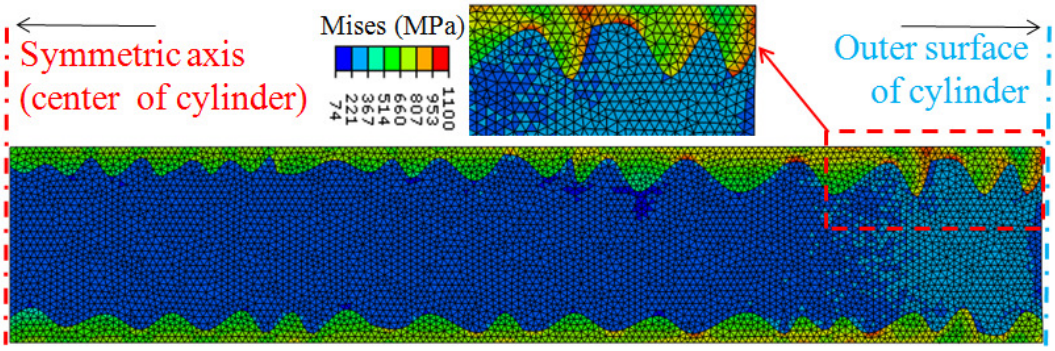


Figure 5.18 Contour of von Mises stress before intermetallic crack initiation. The stress concentrates in the intermetallic zone close to the free surface.

The results in Figure 5.17 also indicate that the cracks in IMC layer always initiate at the region close to free surface (right side in the plot) of the joint specimen. The reason is that the stress concentrates at that corner close to the outer free surface (Figure 5.18), due to necking. And the cracks are most likely to initiate at the stress concentrated locations. Therefore, regarding to the fracture locations, we can conclude that the void-induced fracture mostly initiates inside

the solder joint, and the intermetallic-controlled fracture always takes place close to the surface of the solder joint.

The study of strain rate effect predicts a transition from solder-controlled fracture to intermetallic-controlled fracture, when the strain rate increases, Figure 5.19. The solder-controlled fracture tends to initiate inside the solder near the solder/IMC interface, and the intermetallic-controlled fracture always initiate close to the corner of the outer surface.

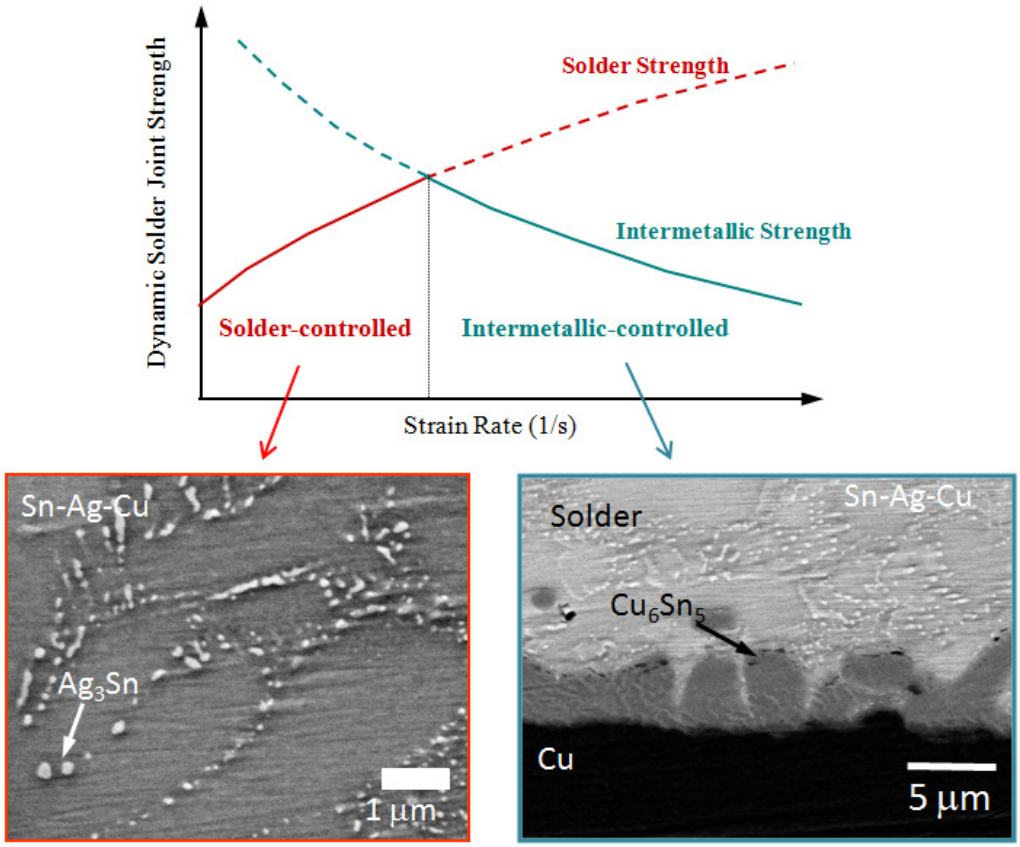


Figure 5.19. Domination of solder joint failure at different strain rate. (Courtesy of N. Chawla)

## 5.6 Summary

The ultimate aim of this study is to build a predictive model to investigate mechanical performance and fracture mechanisms of Pb-free solder joints. In this chapter, we propose two models to study the solder-controlled fracture and IMC-controlled fracture.

A porous plasticity model, the Gurson-Tvergaard-Needleman (GTN) method, is used to characterize the void-induced plastic fracture of the solder alloy. The randomness of the voids is considered, and a stochastic enhancement is created for the GTN model. The first FE model is a three-layer model of Cu/Solder/Cu without intermetallic, and it is designed to focus on the porous plasticity and void-induced fracture. Finite element simulations are conducted using ABAQUS/Standard. We have considered randomly distributed initial void volume fraction with different types of distribution and ranges, and then investigated the effects of this randomness on the crack path and macroscopic stress/strain behavior. It is find that this consideration of the random voids is able to capture more detailed and localized deformation features, such as different crack path and different UTS, and meanwhile does not significantly change the macroscopic stress/strain behavior. It turns out that the random voids are a good approach to qualitatively explain observations of the scatted voids at the crack surface in experiments. Moreover, it is observed that the cracks always initiate inside the solder and propagate towards free surface. A physical interpretation of this phenomenon is provided after examine the porous plasticity theory.

The second FE model includes intermetallic layers, so it is a five-layer coupled fracture model, including both plasticity fracture of solder and brittle fracture of IMC. Dynamic finite element analyses via ABAQUS/Explicit are executed to investigate how the brittle fracture of $Cu_6Sn_5$ contributes to the joint failure. The $Cu_6Sn_5$ is a brittle material with a small failure strain but high fracture stress, comparing with Pb-free solders. If $Cu_6Sn_5$ is modeled as homogenous material, no crack occurs in it. We introduce a concept called vulnerable portion, based on the fact that the intermetallic is inhomogeneous because of grain size, defects and crystallographic orientations, as well as the incoherence of tension and compression behaviors. By this means, the mechanical behavior of $Cu_6Sn_5$ is properly represented, and crack in the IMC region is successfully observed.

The IMC thickness effect and strain rate effect are investigated. Joints with thick intermetallic layer are more likely to have cracks in intermetallics than joints with thin layer, because thick IMC layer is likely to be more inhomogeneous and contain more vulnerable elements. As a result of strain rate hardening of solder alloys, brittle facture of intermetallics exists at high strain rate loading, but not at low strain rate.

The mechanisms of the two fracture patterns are also investigated. The void-induced cracks always occur inside the solder, which can be explained by the higher hydrostatic stress at inside than that close to outer surface. It is also found that the brittle facture always occurs at the region close to the outer free surface of the cylindrical joint, which is a result of stress concentration.

# CHAPTER 6

# CONCLUSION

## 6.1 Summary of the Dissertation

This dissertation has focused on the multi-scale modeling of the mechanical shock behavior of lead-free tin-rich solder alloys. First, the macroscopic stress/strain behaviors of bulk lead-free tin-rich solder alloys are examined at various strain rates. Finite element analysis is conducted to predict the proper geometry of the specimen and the double necking phenomenon. Then the material properties of micron-scale intermetallic are examined by micro-compression test. The accuracy of this measure is validated by a systematic study via finite element analysis. The traction-separation law of the solder/intermetallic interface is developed from an atomistic-based cohesive element method. Finally, the mechanical performance and fracture mechanism of single solder joints are examined via finite element analysis. Plasticity fracture of the solder alloy and brittle fracture of the intermetallics are coupled in one FE model. Failure mechanism of the solder joints are investigated and theoretical explanations are provided.

## 6.2 Conclusions

We have studied the mechanical shock behavior of three Pb-free solder alloys, namely recrystallized pure tin (Sn), furnace-cooled SAC (tin/silver/copper alloy) and water-quench SAC. The applied strain rate ranges from 0.001/s to 30/s. As a result of the strain rate hardening, higher strain rate will make material stiffer.

To achieve a higher strain rate for a given applied displacement rate, parametric FEM analysis has been conducted. With other parameters fixed, the gage length of dogbone sample has been varied from 5 mm to 50 mm in the finite element analysis. 10 mm specimen is more suitable for obtaining reliable and accurate constitutive data for FEM reliability models. Smaller gage length allows a higher strain rate for a given applied displacement rate.

To accurately convert the experimentally measured engineering stress-strain relation to true stress-strain relation, we have developed a self-consistent true stress correction method to calculate correction function, which itself is a function of plastic strain and strain rate. We have corrected the experiment data of three Pb-free solder alloys, recrystallized pure Sn, furnace-cooled SAC and water-quench SAC.

A double-necking phenomenon is observed in the ASTM E-8M specimen (25 mm), which is not observed in the 10 mm specimen. The gage length effect and strain rate effect on the double-necking phenomenon have been investigated via FEA parametric study. The FEM modeling of the dynamic behavior of longer specimens correlates very well with the experimental observations. In particular, the trends observed in experiments could be rationalized based on the FEM modeling results.

To obtain the mechanical behavior of micron-scale intermetallics in the solder joint, micro-compression method has been introduced. Because of the small scale, the stress and strain are indirectly measured in the experiment. To

eliminate the systematic error and improve the accuracy of the measurement, we systematically investigated factors that may affect the stress/strain measurement in the micro-compression test. With certain empirical adjustments to stress/strain measurement, the micro-compression test is believed to be a reliable method to obtain the elastic-plastic properties of intermetallics and other small scale materials.

In the study of interfacial law for solder/intermetallic interface, we started with an atomistic potential, the Modified Embedded Atom Method (MEAM). By using the continuum homogeneous approach, an analytical cohesive traction-separation law for Sn/$Cu_6Sn_5$ interface has been developed, and the cohesive energy of the interface has also been obtained. The cohesive fracture model is studied using ABAQUS, under the assumption that the cohesive zone is the only breakable region. However, the theoretical analysis predicts that the interface has a greater cohesive energy compared with pure Sn and $Cu_6Sn_5$, which explains the reason why in experiment the facture always occurs in pure Sn or $Cu_6Sn_5$, other than the interface.

Due to the experimental observation of numerous voids are observed at the crack surface of the solder joints, a porous plasticity model, the Gurson-Tvergaard-Needleman (GTN) model, has been introduced to study the mechanical performance of Pb-free solder joints. To mimic the random distribution of micro-voids, we have enhanced the GTN method by randomizing the initial void volume fraction. The embedment of random voids is a good approach to capture more

detailed and localized deformation features, such as various crack path and different UTS, and meanwhile it does not significantly change the macroscopic stress/strain behavior of the solder joint.

Moreover, the intermetallic facture is also considered, and coupled with the existing model. Thickness effect and strain rate effect has been investigated in a coupled fracture model, including both plasticity fracture of solder and brittle fracture of IMC. Joints with thick IMC layer are more likely to initiate cracks in IMC region than joints with thin IMC layer. As a result of strain rate hardening of Pb-free solders, brittle facture of intermetallics only exists at high strain rate loading, which predicts the fact that the joint fracture is solder-controlled at low strain rate, and intermetallic-controlled at high strain rate.

The physics and mechanisms of the two fracture patterns are also investigated. The void-induced cracks always occur inside the solder, which can be explained by the higher hydrostatic stress at inside of solder than that close to free surface. It is also found that the brittle facture always occurs at the region close to the outer surface of the cylindrical joint, which is a result of stress concentration at the corner region.

REFERENCES


1. N. Chawla, Thermomechanical behaviour of environmentally benign Pb-free solders, *International Materials Reviews* 54 (2009) 368.

2. K. N. Tu, A. M. Gusak, M. Li, Physics and materials challenges for lead-free solders, *Journal of Applied Physics* 93 (2003) 1335.

3. K. Zeng, K. N. Tu, Six cases of reliability study of Pb-free solder joints in electronic packaging technology, *Materials Science & Engineering R-Reports* 38 (2002) 55.

4. M. Abtew, G. Selvaduray, Lead-free solders in microelectronics, *Materials Science & Engineering R-Reports* 27 (2000) 95.

5. Y. Li, C. P. Wong, Recent advances of conductive adhesives as a lead-free alternative in electronic packaging: Materials, processing, reliability and applications, *Materials Science & Engineering R-Reports* 51 (2006) 1.

6. S. Sathe, B. Sammakia, A review of recent developments in some practical aspects of air-cooled electronic packages, *Journal of Heat Transfer-Transactions of the Asme* 120 (1998) 830.

7. C. P. Wong, R. S. Bollampally, Thermal conductivity, elastic modulus, and coefficient of thermal expansion of polymer composites filled with ceramic particles for electronic packaging, *Journal of Applied Polymer Science* 74 (1999) 3396.

8. N. Chawla, R. S. Sidhu, Microstructure-based modeling of deformation in Sn-rich (Pb-free) solder alloys, *Journal of Materials Science-Materials in Electronics* 18 (2007) 175.

9. K. E. Yazzie, H. Fei, J. J. Williams, H. Jiang, N. Chawla, Mechanical Shock Behavior of Bulk Pure Sn Solder, *Journal of Electronic Materials* 38 (2009) 2746.

10. F. D. Silva, J. J. Williams, B. R. Muller, M. P. Hentschel, P. D. Portella, N. Chawla, Three-Dimensional Microstructure Visualization of Porosity and

Fe-Rich Inclusions in SiC Particle-Reinforced Al Alloy Matrix Composites by X-Ray Synchrotron Tomography, *Metallurgical and Materials Transactions a-Physical Metallurgy and Materials Science* 41A (2010) 2121.

11. K. E. Yazzie, J. J. Williams, D. Kingsbury, P. Peralta, H. Jiang, N. Chawla, Digital Image Correlation Analysis of the Deformation Behavior of Pb-free Solders at Intermediate Strain Rates, *Jom* 62 (2010) 16.

12. L. Jiang, N. Chawla, Mechanical properties of Cu6Sn5 intermetallic by micropillar compression testing, *Scripta Materialia* 63 (2010) 480.

13. M. A. Dudek, N. Chawla, Nanoindentation of rare earth-Sn intermetallics in Pb-free solders, *Intermetallics* 18 (2010) 1016.

14. T. Laurila, V. Vuorinen, J. K. Kivilahti, Interfacial reactions between lead-free solders and common base materials, *Materials Science & Engineering R-Reports* 49 (2005) 1.

15. H. Y. Fei, K. Yazzie, J. Williams, N. Chawla, H. Q. Jiang, Multiscale Modeling of the Interfacial Fracture Behavior in the Sn-Cu-6 Sn-5-Cu System, *Journal of Computational and Theoretical Nanoscience* 8 (2011) 873.

16. Poison PCs/Toxic TVs Executive Summary, Silicon Valley Toxic Corporation, (2007).

17. R. R.R. Tummala, and J. Eugene,, Microelectronics Packaging Handbook, van Norstrand Reinhold, (1989).

18. P. L. Hacke, A. F. Sprecher, H. Conrad, Microstructure coarsening during thermo-mechanical fatigue of Pb-Sn solder joints, *Journal of Electronic Materials* 26 (1997) 774.

19. K. N. Tu, K. Zeng, Tin-lead (SnPb) solder reaction in flip chip technology, *Materials Science & Engineering R-Reports* 34 (2001) 1.

20. N. Chawla, S. Chada, S. K. Kang, C. R. Kao, K. L. Lin, J. Lucas, L. Turbini, Lead-free solder implementation: Reliability, alloy development, new technology - Foreword, *Journal of Electronic Materials* 35 (2006) 2073.

21. J. Glazer, Metallurgy of Low-Temperature Pb-Free Solders for Electronic Assembly, *International Materials Reviews* 40 (1995) 65.

22. J. Glazer, Microstructure and Mechanical-Properties of Pb-Free Solder Alloys for Low-Cost Electronic Assembly - a Review, *Journal of Electronic Materials* 23 (1994) 693.

23. M. Mccormack, S. H. Jin, Progress in the Design of New Lead-Free Solder Alloys, *Jom-Journal of the Minerals Metals & Materials Society* 45 (1993) 36.

24. P. T. Vianco, D. R. Frear, Issues in the Replacement of Lead-Bearing Solders, *Jom-Journal of the Minerals Metals & Materials Society* 45 (1993) 14.

25. D. R. Frear, Issues related to the implementation of Pb-free electronic solders in consumer electronics, *Journal of Materials Science-Materials in Electronics* 18 (2007) 319.

26. W. J. Plumbridge, Solders in electronics, *Journal of Materials Science* 31 (1996) 2501.

27. R. S. Sidhu, N. Chawla, Thermal fatigue behavior of Sn-rich (Pb-Free) solders, *Metallurgical and Materials Transactions a-Physical Metallurgy and Materials Science* 39A (2008) 799.

28. R. S. Sidhu, N. Chawla, Microstructure characterization and creep behavior of Pb-free Sn-rich solder alloys: Part I. Microstructure characterization of bulk solder and solder/copper joints, *Metallurgical and Materials Transactions a-Physical Metallurgy and Materials Science* 39A (2008) 340.

29. R. S. Sidhu, X. Deng, N. Chawla, Microstructure characterization and creep behavior of Pb-free Sn-rich solder alloys: Part II. Creep behavior of bulk solder and solder/copper joints, *Metallurgical and Materials Transactions a-Physical Metallurgy and Materials Science* 39A (2008) 349.

30. M. Kerr, N. Chawla, Creep deformation behavior of Sn-3.5Ag solder/Cu couple at small length scales, *Acta Materialia* 52 (2004) 4527.

31. M. Kerr, N. Chawla, Creep deformation behaviour of Sn-3.5Ag solder at small length scales, *Jom* 56 (2004) 50.

32. J. E. Field, S. M. Walley, W. G. Proud, H. T. Goldrein, C. R. Siviour, Review of experimental techniques for high rate deformation and shock studies, *International Journal of Impact Engineering* 30 (2004) 725.

33. T. Y. Tee, H. S. Ng, C. T. Lim, E. Pek, Z. W. Zhong, Impact life prediction modeling of TFBGA packages under board level drop test, *Microelectronics Reliability* 44 (2004) 1131.

34. D. Reiff, E. Bradley, A Novel Mechanical Shock Test Method to Evaluate Lead-Free BGA Solder Joint Reliability, *Electronic Components and Technology Conference* (2005) 1519.

35. M. Date, T. Shoji, M. Fujiyoshi, K. Sato, K. N. Tu, Impact Reliability of Solder Joints, *Electronic Components and Technology Conference* (2004) IEEE 668.

36. K. T. Tsai, F. L. Liu, E. H. Wong, R. Rajoo, High strain rate testing of solder interconnections, *Soldering & Surface Mount Technology* 18 (2006) 12.

37. J. Y. H. Chia, B. Cotterell, T. C. Chai, The mechanics of the solder ball shear test and the effect of shear rate, *Materials Science and Engineering a-Structural Materials Properties Microstructure and Processing* 417 (2006) 259.

38. R. Pandher, M. Boureghda, Identification of Brittle Solder Joints Uding High Strain Rate Testing of BGA Solder Joints, *45th Annual International Reliability Physics Symposium* (2007) 107.

39. K. Newman, BGA Brittle Fracture – Alternative Solder Joint Integrity Test Methods, *Proc. 55th Electronic Components & Technology Conference* (2005) 1194.

40. B. L. Boyce, T. B. Crenshaw, Servohydraulic Methods For Mechanical Testing in the Sub-Hopkinson Rate Regime up to Strain Rates of 500 1/s, *SAND2005-5678* (2005).

41. ABAQUS Inc., ABAQUS Analysis User's Manual V. 6.9, (2009).

42. P. W. Bridgman, Studies in Large Plastic Flow and Fracture, McGraw-Hill, New York (1952).

43. M. Alves, N. Jones, Influence of hydrostatic stress on failure of axisymmetric notched specimens, *Journal of the Mechanics and Physics of Solids* 47 (1999) 643.

44. J. W. Hancock, D. K. Brown, On the Role of Strain and Stress State in Ductile Failure, *Journal of the Mechanics and Physics of Solids* 31 (1983) 1.

45. Z. L. Zhang, M. Hauge, J. Odegard, C. Thaulow, Determining material true stress-strain curve from tensile specimens with rectangular cross-section, *International Journal of Solids and Structures* 36 (1999) 3497.

46. G. La Rosa, G. Mirone, A. Risitano, Postnecking elastoplastic characterization: Degree of approximation in the Bridgman method and properties of the flow-stress/true-stress ratio, *Metallurgical and Materials Transactions a-Physical Metallurgy and Materials Science* 34 (2003) 615.

47. J. M. Choung, S. R. Cho, Study on true stress correction from tensile tests, *Journal of Mechanical Science and Technology* 22 (2008) 1039.

48. J. Aronofsky, Evaluation of Stress Distribution in the Symmetrical Neck of Flat Tensile Bars, *Journal of Applied Mechanics-Transactions of the Asme* 18 (1951) 75.

49. Y. Ling, Uniaxial true stress-strain after necking, *AMP J. Technol.* 5 (1996) 37.

50. J. Wilde, K. Becker, M. Thoben, W. Blum, T. Jupitz, G. Z. Wang, Z. N. N. Cheng, Rate dependent constitutive relations based on Anand model for 92.5Pb5Sn2.5Ag solder, *Ieee Transactions on Advanced Packaging* 23 (2000) 408.

51. P. R. Guduru, L. B. Freund, The dynamics of multiple neck formation and fragmentation in high rate extension of ductile materials, *International Journal of Solids and Structures* 39 (2002) 5615.

52. V. B. Shenoy, L. B. Freund, Necking bifurcations during high strain rate extension, *Journal of the Mechanics and Physics of Solids* 47 (1999) 2209.

53. X. Long, I. Dutta, V. Sarihan, D. R. Frear, Deformation behavior of Sn-3.8Ag-0.7Cu solder at intermediate strain rates: Effect of microstructure and test conditions, *Journal of Electronic Materials* 37 (2008) 189.

54. Z. Mei, A. J. Sunwoo, J. W. Morris, Analysis of Low-Temperature Intermetallic Growth in Copper-Tin Diffusion Couples, *Metallurgical Transactions a-Physical Metallurgy and Materials Science* 23 (1992) 857.

55. P. T. Vianco, P. F. Hlava, A. C. Kilgo, Intermetallic Compound Layer Formation between Copper and Hot-Dipped 100in, 50in-50sn, 100sn, and 63sn-37pb Coatings, *Journal of Electronic Materials* 23 (1994) 583.

56. S. Choi, T. R. Bieler, J. P. Lucas, K. N. Subramanian, Characterization of the growth of intermetallic interfacial layers of Sn-Ag and Sn-Pb eutectic solders and their composite solders on Cu substrate during isothermal long-term aging, *Journal of Electronic Materials* 28 (1999) 1209.

57. K. S. Kim, S. H. Huh, K. Suganuma, Effects of intermetallic compounds on properties of Sn-Ag-Cu lead-free soldered joints, *Journal of Alloys and Compounds* 352 (2003) 226.

58. D. R. Frear, P. T. Vianco, Intermetallic Growth and Mechanical-Behavior of Low and High-Melting Temperature Solder Alloys, *Metallurgical and Materials Transactions a-Physical Metallurgy and Materials Science* 25 (1994) 1509.

59. D. R. Frear, The mechanical behavior of interconnect materials for electronic packaging, *Jom-Journal of the Minerals Metals & Materials Society* 48 (1996) 49.

60. P. Protsenko, A. Terlain, V. Traskine, N. Eustathopoulos, The role of intermetallics in wetting in metallic systems, *Scripta Materialia* 45 (2001) 1439.

61. Y. C. Chan, A. C. K. So, J. K. L. Lai, Growth kinetic studies of Cu-Sn intermetallic compound and its effect on shear strength of LCCC SMT solder joints, *Materials Science and Engineering B-Solid State Materials for Advanced Technology* 55 (1998) 5.

62. E. I. Stromswold, R. E. Pratt, D. J. Quesnel, The Effect of Substrate Surface-Roughness on the Fracture-Toughness of Cu/96.5sn-3.5ag Solder Joints, *Journal of Electronic Materials* 23 (1994) 1047.

63. R. E. Pratt, E. I. Stromswold, D. J. Quesnel, Mode-I Fracture-Toughness Testing of Eutectic Sn-Pb Solder Joints, *Journal of Electronic Materials* 23 (1994) 375.

64. Subrahma.B, Elastic-Moduli of Some Eutectic Alloy Systems, *Transactions of the Japan Institute of Metals* 13 (1972) 89.

65. Subrahma.B, Elastic-Moduli of Some Complicated Binary Alloy Systems, *Transactions of the Japan Institute of Metals* 13 (1972) 93.

66. H. Rhee, J. P. Lucas, K. N. Subramanian, Micromechanical characterization of thermomechanically fatigued lead-free solder joints, *Journal of Materials Science-Materials in Electronics* 13 (2002) 477.

67. D. Tabor, The Hardness of Metals, Oxford University Press, (2005).

68. M. D. Uchic, D. M. Dimiduk, J. N. Florando, W. D. Nix, Sample dimensions influence strength and crystal plasticity, *Science* 305 (2004) 986.

69. Z. L. Liu, X. M. Liu, Z. Zhuang, X. C. You, A multi-scale computational model of crystal plasticity at submicron-to-nanometer scales, *International Journal of Plasticity* 25 (2009) 1436.

70. S. Akarapu, H. M. Zbib, D. F. Bahr, Analysis of heterogeneous deformation and dislocation dynamics in single crystal micropillars under compression, *International Journal of Plasticity* 26 (2010) 239.

71. C. M. Byer, B. Li, B. Y. Cao, K. T. Ramesh, Microcompression of single-crystal magnesium, *Scripta Materialia* 62 (2010) 536.

72. J. A. El-Awady, S. I. Rao, C. Woodward, D. M. Dimiduk, M. D. Uchic, Trapping and escape of dislocations in micro-crystals with external and internal barriers, *International Journal of Plasticity* 27 (2011) 372.

73. D. Kaufmann, R. Monig, C. A. Volkert, O. Kraft, Size dependent mechanical behaviour of tantalum, *International Journal of Plasticity* 27 (2011) 470.

74. H. Zhang, B. E. Schuster, Q. Wei, K. T. Ramesh, The design of accurate micro-compression experiments, *Scripta Materialia* 54 (2006) 181.

75. ABAQUS Inc., ABAQUS Analysis User's Manual V. 6.7, (2007).

76. I. N. Sneddon, The relation between load and penetration in the axisymmetric boussinesq problem for a punch of arbitrary profile, *Int. J. Engng Sci.* 3 (1965) 47.

77. C. P. Frick, B. G. Clark, S. Orso, A. S. Schneider, E. Arzt, Size effect on strength and strain hardening of small-scale [111] nickel compression pillars, *Materials Science and Engineering a-Structural Materials Properties Microstructure and Processing* 489 (2008) 319.

78. C. A. Volkert, E. T. Lilleodden, Size effects in the deformation of sub-micron Au columns, *Philosophical Magazine* 86 (2006) 5567.

79. G. Simmons, H. Wang, Single Crystal Elastic Constants and Calculated Aggregate Properties: A Handbook, MIT Press, Cambridge, MA (1971).

80. D. S. Dugdale, Yielding of Steel Sheets Containing Slits, *Journal of the Mechanics and Physics of Solids* 8 (1960) 100.

81. G. I. Barenblatt, Citation Classic - the Mathematical-Theory of Equilibrium Cracks in Brittle-Fracture, *Current Contents/Engineering Technology & Applied Sciences* (1983) 20.

82. J. Rice, Mathematical analysis in the mechanics of fracture, Academic Press, New York (1968).

83. O. Samudrala, A. J. Rosakis, Effect of loading and geometry on the subsonic/intersonic transition of a bimaterial interface crack, *Engineering Fracture Mechanics* 70 (2003) 309.

84. D. V. Kubair, P. H. Geubelle, Y. G. Y. Huang, Analysis of a rate-dependent cohesive model for dynamic crack propagation, *Engineering Fracture Mechanics* 70 (2003) 685.

85. A. Needleman, A Continuum Model for Void Nucleation by Inclusion Debonding, *Journal of Applied Mechanics-Transactions of the Asme* 54 (1987) 525.

86. G. T. Camacho, M. Ortiz, Computational modelling of impact damage in brittle materials, *International Journal of Solids and Structures* 33 (1996) 2899.

87. P. H. Geubelle, J. S. Baylor, Impact-induced delamination of composites: a 2D simulation, *Composites Part B-Engineering* 29 (1998) 589.

88. P. Zhang, P. Klein, Y. Huang, H. Gao, P. D. Wu, Numerical simulation of cohesive fracture by the virtual-internal-bond model, *Cmes-Computer Modeling in Engineering & Sciences* 3 (2002) 263.

89. Y. Huang, H. Gao, Intersonic crack propagation - Part I: The fundamental solution, *Journal of Applied Mechanics-Transactions of the Asme* 68 (2001) 169.

90. D. V. Kubair, P. H. Geubelle, Y. Y. Huang, Intersonic crack propagation in homogeneous media under shear-dominated loading: theoretical analysis, *Journal of the Mechanics and Physics of Solids* 50 (2002) 1547.

91. P. H. Geubelle, D. V. Kubair, Intersonic crack propagation in homogeneous media under shear-dominated loading: numerical analysis, *Journal of the Mechanics and Physics of Solids* 49 (2001) 571.

92. O. Samudrala, Y. Huang, A. J. Rosakis, Subsonic and intersonic mode II crack propagation with a rate-dependent cohesive zone, *Journal of the Mechanics and Physics of Solids* 50 (2002) 1231.

93. G. Thiagarajan, Y. Y. Huang, K. J. Hsia, Fracture simulation using an elasto-viscoplastic virtual internal bond model with finite elements, *Journal of Applied Mechanics-Transactions of the Asme* 71 (2004) 796.

94. H. Tan, C. Liu, Y. Huang, P. H. Geubelle, The cohesive law for the particle/matrix interfaces in high explosives, *Journal of the Mechanics and Physics of Solids* 53 (2005) 1892.

95. H. Tan, Y. Huang, C. Liu, P. H. Geubelle, Effect of nonlinear interface debonding on the constitutive model of composite materials, *International Journal for Multiscale Computational Engineering* 4 (2006) 147.

96. L. Y. Jiang, Y. Huang, H. Jiang, G. Ravichandran, H. Gao, K. C. Hwang, B. Liu, A cohesive law for carbon nanotube/polymer interfaces based on

the van der Waals force, *Journal of the Mechanics and Physics of Solids* 54 (2006) 2436.

97. W. B. Lu, J. Wu, J. Song, K. C. Hwang, L. Y. Jiang, Y. Huang, A cohesive law for interfaces between multi-wall carbon nanotubes and polymers due to the van der Waals interactions, *Computer Methods in Applied Mechanics and Engineering* 197 (2008) 3261.

98. L. Y. Jiang, H. L. Tan, J. Wu, Y. G. Huang, K. C. Hwang, Continuum modeling of interfaces in polymer matrix composites reinforced by carbon nanotubes, *Nano* 2 (2007) 139.

99. H. Tan, L. Y. Jiang, Y. Huang, B. Liu, K. C. Hwang, The effect of van der Waals-based interface cohesive law on carbon nanotube-reinforced composite materials, *Composites Science and Technology* 67 (2007) 2941.

100. W. B. Lu, J. Wu, L. Y. Jiang, Y. Huang, K. C. Hwang, B. Liu, A cohesive law for multi-wall carbon nanotubes, *Philosophical Magazine* 87 (2007) 2221.

101. M. S. Daw, S. M. Foiles, M. I. Baskes, The Embedded-Atom Method - a Review of Theory and Applications, *Materials Science Reports* 9 (1993) 251.

102. R. G. Hoagland, M. S. Daw, S. M. Foiles, M. I. Baskes, An Atomic Model of Crack Tip Deformation in Aluminum Using an Embedded Atom Potential, *Journal of Materials Research* 5 (1990) 313.

103. M. I. Baskes, S. M. Foiles, M. S. Daw, Application of the Embedded Atom Method to the Fracture of Interfaces, *Journal De Physique* 49 (1988) 483.

104. S. M. Foiles, M. I. Baskes, C. F. Melius, M. S. Daw, Calculation of Hydrogen Dissociation Pathways on Nickel Using the Embedded Atom Method, *Journal of the Less-Common Metals* 130 (1987) 465.

105. S. M. Foiles, M. I. Baskes, M. S. Daw, Embedded-Atom-Method Functions for the Fcc Metals Cu, Ag, Au, Ni, Pd, Pt, and Their Alloys, *Physical Review B* 33 (1986) 7983.

106. M. I. Baskes, M. S. Daw, Applications of the Embedded Atom Method to Hydrogen Embrittlement, *Journal of Metals* 37 (1985) A22.

107. M. S. Daw, M. I. Baskes, Embedded-Atom Method - Derivation and Application to Impurities, Surfaces, and Other Defects in Metals, *Physical Review B* 29 (1984) 6443.

108. M. I. Baskes, Modified Embedded-Atom Potentials for Cubic Materials and Impurities, *Physical Review B* 46 (1992) 2727.

109. M. I. Baskes, R. A. Johnson, Modified Embedded-Atom Potentials for Hcp Metals, *Modelling and Simulation in Materials Science and Engineering* 2 (1994) 147.

110. J. F. Aguilar, R. Ravelo, M. I. Baskes, Morphology and dynamics of 2D Sn-Cu alloys on (100) and (111) Cu surfaces, *Modelling and Simulation in Materials Science and Engineering* 8 (2000) 335.

111. D. Suh, D. W. Kim, P. L. Liu, H. Kim, J. A. Weninger, C. M. Kumar, A. Prasad, B. W. Grimsley, H. B. Tejada, Effects of Ag content on fracture resistance of Sn-Ag-Cu lead-free solders under high-strain rate conditions, *Materials Science and Engineering a-Structural Materials Properties Microstructure and Processing* 460 (2007) 595.

112. Y. L. Liu, S. Gale, R. W. Johnson, Investigation of the role of void formation at the Cu-to-intermetallic interface on aged drop test performance, *Ieee Transactions on Electronics Packaging Manufacturing* 30 (2007) 63.

113. T. T. Mattila, P. Marjamaki, J. K. Kivilahti, Reliability of CSP interconnections under mechanical shock loading conditions, *Ieee Transactions on Components and Packaging Technologies* 29 (2006) 787.

114. J. M. Song, J. J. Lin, C. F. Huang, H. Y. Chuang, Crystallization, morphology and distribution of Ag3Sn in Sn-Ag-Cu alloys and their influence on the vibration fracture properties, *Materials Science and Engineering a-Structural Materials Properties Microstructure and Processing* 466 (2007) 9.

115. A. L. Gurson, Continuum Theory of Ductile Rupture by Void Nucleation and Growth .1. Yield Criteria and Flow Rules for Porous Ductile Media, *Journal of Engineering Materials and Technology-Transactions of the Asme* 99 (1977) 2.

116. V. Tvergaard, Material Failure by Void Growth to Coalescence, *Advances in Applied Mechanics* 27 (1990) 83.

117. V. Tvergaard, Material Failure by Void Coalescence in Localized Shear Bands, *International Journal of Solids and Structures* 18 (1982) 659.

118. R. Becker, A. Needleman, O. Richmond, V. Tvergaard, Void Growth and Failure in Notched Bars, *Journal of the Mechanics and Physics of Solids* 36 (1988) 317.

119. R. Becker, A. Needleman, S. Suresh, V. Tvergaard, A. K. Vasudevan, An Analysis of Ductile Failure by Grain-Boundary Void Growth, *Acta Metallurgica* 37 (1989) 99.

120. R. D. Thomson, J. W. Hancock, Ductile Failure by Void Nucleation, Growth and Coalescence, *International Journal of Fracture* 26 (1984) 99.

121. X. Deng, R. S. Sidhu, P. Johnson, N. Chawla, Influence of reflow and thermal aging on the shear strength and fracture behavior of Sn-3.5Ag Solder/Cu joints, *Metallurgical and Materials Transactions a-Physical Metallurgy and Materials Science* 36A (2005) 55.

122. X. Deng, N. Chawla, K. K. Chawla, M. Koopman, Deformation behavior of (Cu, Ag)-Sn intermetallics by nanoindentation, *Acta Materialia* 52 (2004) 4291.

123. S. H. Chiu, C. Chen, Investigation of void nucleation and propagation during electromigration of flip-chip solder joints using x-ray microscopy, *Applied Physics Letters* 89 (2006).

124. F. Ochoa, J. J. Williams, N. Chawla, The effects of cooling rate on microstructure and mechanical behavior of Sn-3.5Ag solder, *Jom-Journal of the Minerals Metals & Materials Society* 55 (2003) 56.

125. D. J. Wang, R. L. Panton, Experimental study of void formation in eutectic and lead-free solder bumps of flip-chip assemblies, *Journal of Electronic Packaging* 128 (2006) 202.

126. J. R. Rice, D. M. Tracey, On Ductile Enlargement of Voids in Triaxial Stress Fields, *Journal of the Mechanics and Physics of Solids* 17 (1969) 201.

127. V. Tvergaard, Influence of Voids on Shear Band Instabilities under Plane-Strain Conditions, *International Journal of Fracture* 17 (1981) 389.

128. V. Tvergaard, Influence of Void Nucleation on Ductile Shear Fracture at a Free-Surface, *Journal of the Mechanics and Physics of Solids* 30 (1982) 399.

129. C. C. Chu, A. Needleman, Void Nucleation Effects in Biaxially Stretched Sheets, *Journal of Engineering Materials and Technology-Transactions of the Asme* 102 (1980) 249.

130. V. Tvergaard, On Localization in Ductile Materials Containing Spherical Voids, *International Journal of Fracture* 18 (1982) 237.

131. A. Needleman, V. Tvergaard, A Numerical Study of Void Distribution Effects on Dynamic, Ductile Crack-Growth, *Engineering Fracture Mechanics* 38 (1991) 157.

132. J. Wen, Y. G. Huang, K. C. Hwang, The void-size effect on plastic flow localization in the Gurson model, *Acta Mechanica Sinica* 20 (2004) 393.

133. J. Wen, Y. Huang, K. C. Hwang, C. Liu, M. Li, The modified Gurson model accounting for the void size effect, *International Journal of Plasticity* 21 (2005) 381.

134. A. Needleman, J. R. Rice, Mechanics of Sheet Metal Forming, Plenum Press, New York (1978).

135. X. Deng, M. Koopman, N. Chawla, K. K. Chawla, Young's modulus of (Cu, Ag)-Sn intermetallics measured by nanoindentation, *Materials Science and Engineering a-Structural Materials Properties Microstructure and Processing* 364 (2004) 240.

# APPENDIX A

# CALCULATION OF LOCAL STRESS/STRAIN AT IRREGULAR-SHAPED CROSS SECTION

A.1 The Stress/Strain Calculation at Necking Zone

Stress is calculated by

$$\sigma = \frac{P}{A} \tag{A.1}$$

and strain is calculated by

$$\varepsilon = \ln\left(\frac{A_0}{A}\right) \tag{A.2}$$

where $P$ is applied load, and $A_0$ is the original cross section area of the specimen. Both of them are known. The only unknown is the instantaneous cross section area $A$.

A.2 Measurement of Instantaneous Cross Section Area in Experiment

Figure A.1 shows the necking and failure process of a pure Sn dogbone specimen. The instantaneous cross section area is calculated by

$$A = \left(\frac{t^1 + t^2}{2}\right) \cdot b \tag{A.3}$$

where $t^1$, $t^2$ and $b$ can be measured form the images (Figure A.1) obtained by experiments.

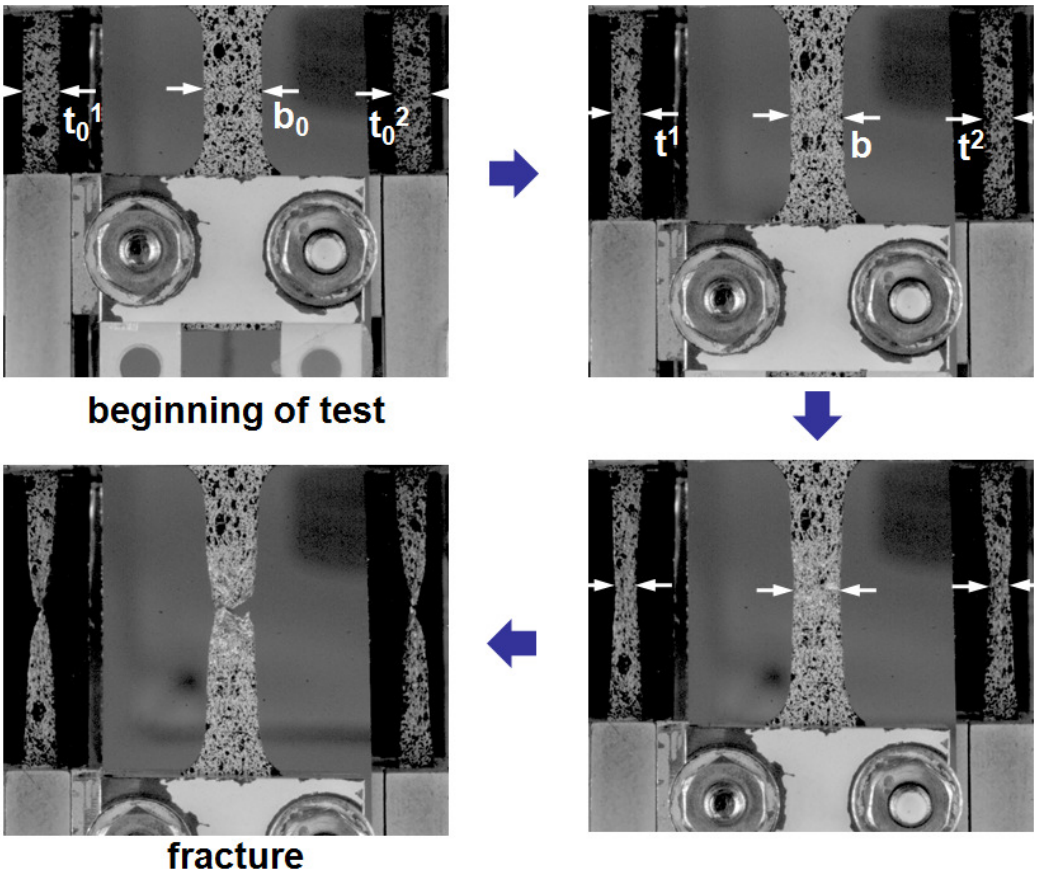


Figure A.1. Furnace-cooled pure Sn tested at 0.001/s (Courtesy of K. Yazzie and N. Chawla)

A.3 Measurement of Instantaneous Cross Section Area in FEA

In finite element analysis, to obtain the cross section area of the necking zone, the coordinates of the nodes at the boundary is exported to MATLAB, and then MATLAB re-plots the irregular shape of the cross section area (Figure A.2). The area of the irregular shape is calculated by the function POLYAREA.

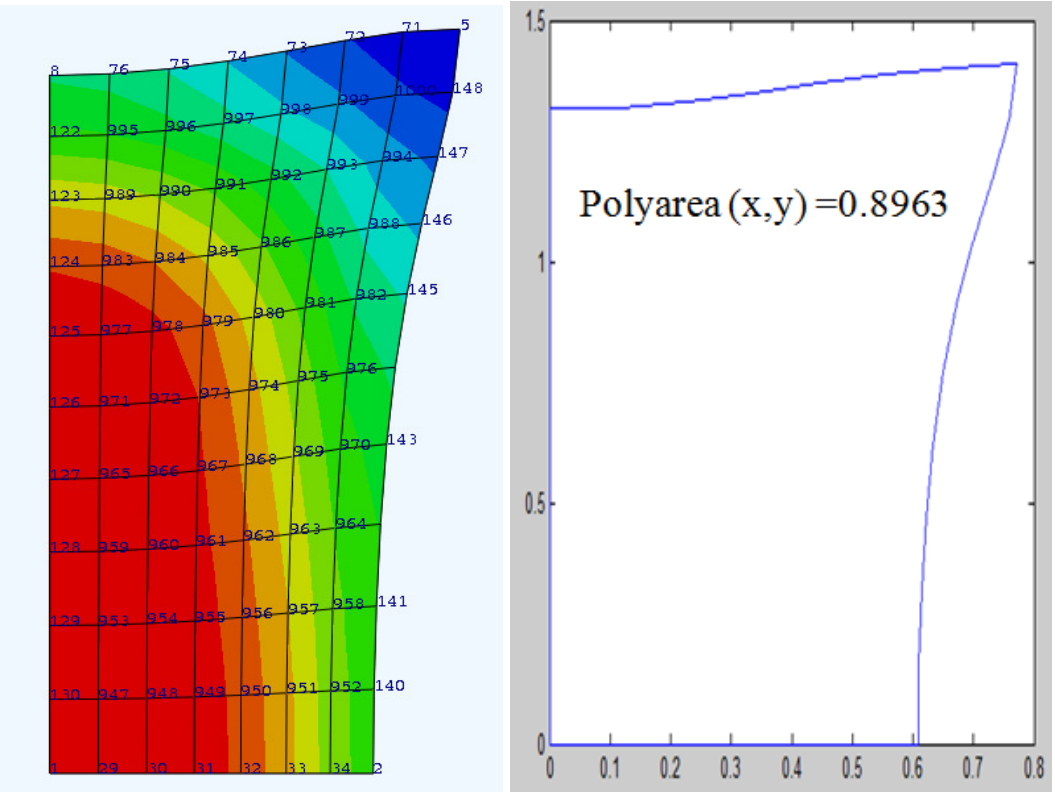


Figure A.2. Cross section area of the necking zone of a 1/4 symmetric rectangular specimen under simple tension loading

# APPENDIX B

## CORRECTION FUNCTIONS FOR PB-FREE SOLDERS AT ALL STRAIN RATES (0.001/S to 30/s)

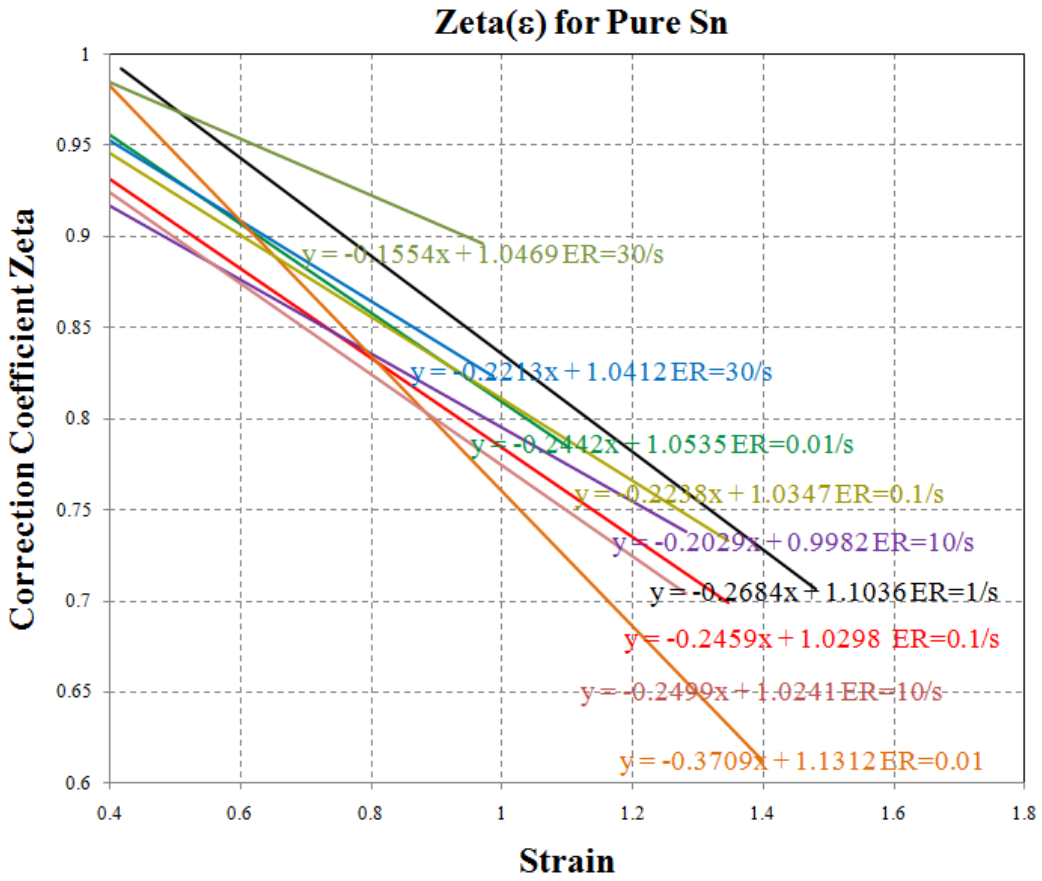

Figure B.1. Correction functions for pure Sn at all strain rates.

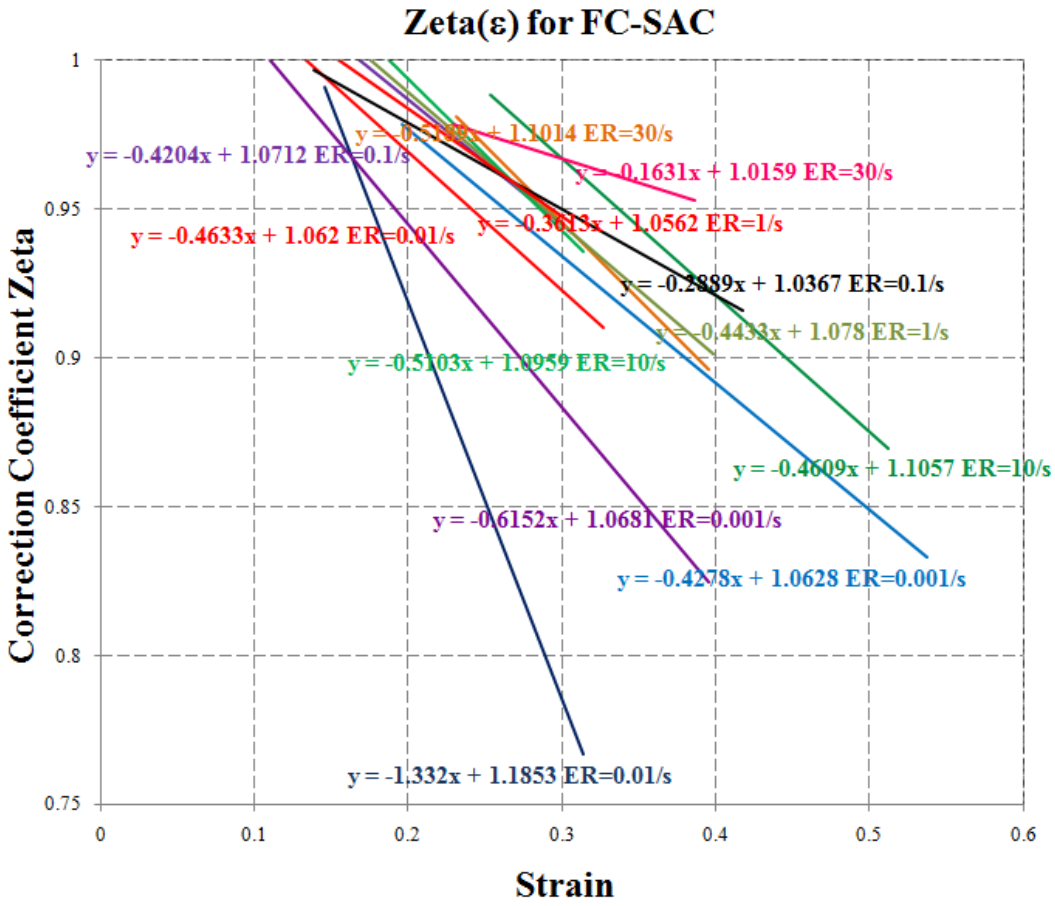


Figure B.2. Correction functions for Furnace-cooled SAC at all strain rates.

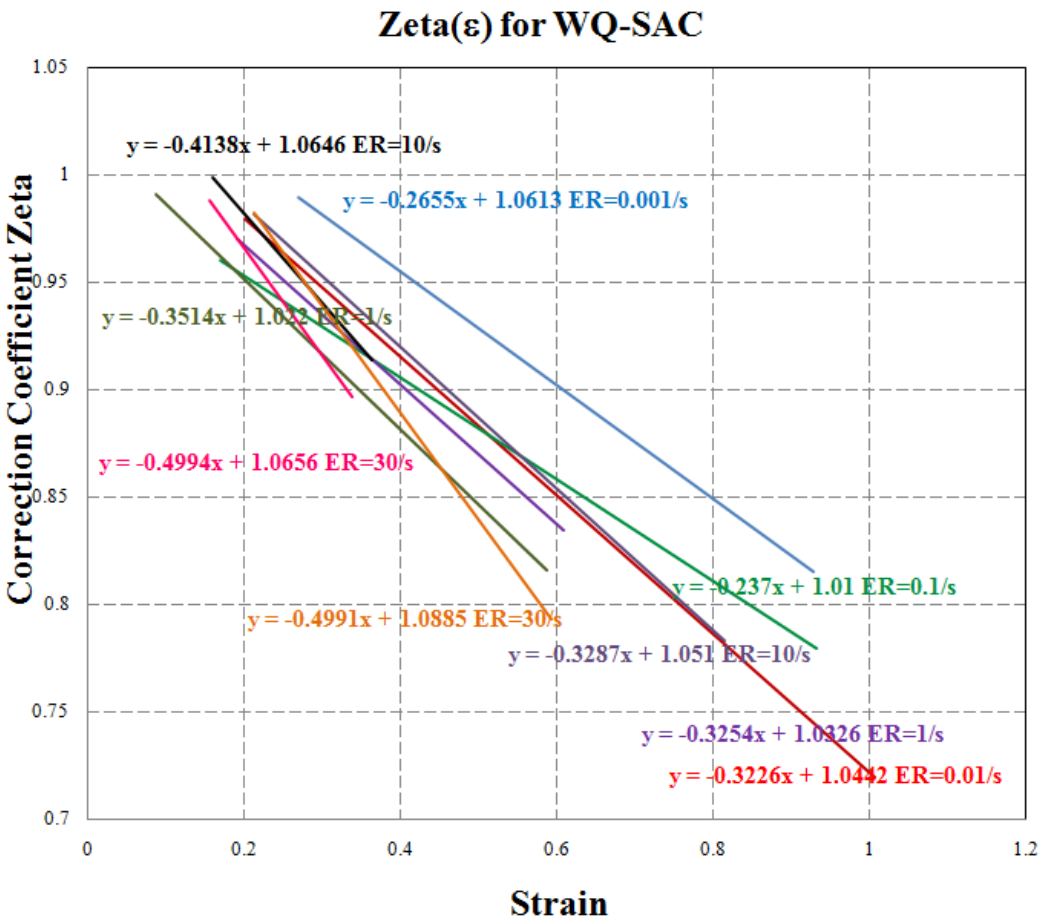


Figure B.3. Correction functions for Water-quench SAC at all strain rates.

# APPENDIX C

# NUMBER DENSITY OF CU AND SN ATOMS OF PURE TIN AND INTERMETALLICS

Figure C.1 shows the crystal structure of bulk Sn. $a$ = 3.18 Å, c = 5.81 Å.

The number density of Sn atom in bulk Sn is

$$\rho_{Sn}^{bulk} = \frac{2}{0.318 \times 0.318 \times 0.581} = 34 / nm^3 \tag{C.1}$$

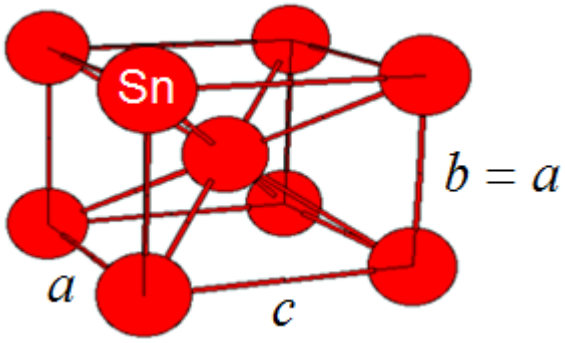


Figure C.1. Schematic crystal structure of bulk Sn

Figure C.2 shows the crystal structure of $Cu_6Sn_5$. $a$ = 4.02 Å, c = 5.09 Å.

The number density of Sn atom in $Cu_6Sn_5$ is

$$\rho_{Sn}^{IMC} = \frac{2}{a \times b \times c} = 22.3 / nm^3 \tag{C.2}$$

and number density of Cu atom in $Cu_6Sn_5$ is

$$\rho_{Cu}^{IMC} = \frac{6}{5} \rho_{Sn}^{IMC} = 26.76 / nm^3 \tag{C.3}$$

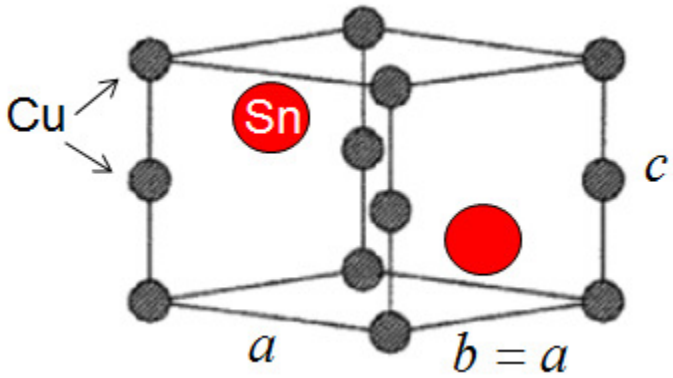


Figure C.2. Schematic crystal structure of $Cu_6Sn_5$

# APPENDIX D

# INTEGRALS OF SN-SN AND CU-SN PAIR POTENTIALS

The integrals of pair potential over the volume of the bulk Sn can be expressed by a double integral as follows.

Sn atoms embedded into bulk Sn matrix,

$$
\begin{aligned}
&\frac{1}{2}\int_{V_{\text{bulk Sn}}} \phi_{Sn-Sn}(R)\,\rho_{Sn}^{bulk}\,dV \\
&=\frac{1}{2}\int_{z=h}^{\infty}\int_{r=0}^{\infty}\phi_{Sn-Sn}(R)\,\rho_{Sn}^{bulk}\,2\pi r dr dz \\
&=\frac{1}{2}\pi\rho_{Sn}^{bulk}\frac{R_{Sn}^{0}h^{2}E_{Sn}^{0}}{(\alpha_{Sn})^{3}}\exp\left[\alpha_{Sn}\left(1-\frac{h}{R_{Sn}^{0}}\right)\right]\left[-(\alpha_{Sn})^{2}-\frac{5R_{Sn}^{0}\alpha_{Sn}}{h}\right. \\
&\left.+\frac{R_{Sn}^{0}(\alpha_{Sn})^{2}}{h}-8\left(\frac{R_{Sn}^{0}}{h}\right)^{2}+2\alpha_{Sn}\left(\frac{R_{Sn}^{0}}{h}\right)^{2}\right] \\
&-\frac{1}{2}\pi\rho_{Sn}^{bulk}\frac{R_{Sn}^{0}h^{2}A_{Sn}E_{Sn}^{0}}{\beta_{Sn}^{3}}\exp\left[\beta_{Sn}\left(1-\frac{h}{R_{Sn}^{0}}\right)\right]\left[-\beta_{Sn}^{2}-\frac{4R_{Sn}^{0}\beta_{Sn}}{h}\right. \\
&\left.+\frac{R_{Sn}^{0}\beta_{Sn}^{2}}{h}-6\left(\frac{R_{Sn}^{0}}{h}\right)^{2}+2\beta_{Sn}\left(\frac{R_{Sn}^{0}}{h}\right)^{2}\right]
\end{aligned}
\qquad \text{(D.1)}
$$

Cu atoms embedded into bulk Sn matrix,

$$
\begin{aligned}
&\frac{1}{2}\int_{V_{\text{bulk Sn}}}\phi_{Cu-Sn}(R)\,\rho_{Sn}^{bulk}\,dV \\
&=\frac{1}{2}\int_{z=h}^{\infty}\int_{r=0}^{\infty}\phi_{Cu-Sn}(R)\,\rho_{Sn}^{bulk}\,2\pi r dr dz \\
&=\frac{1}{3}\pi\rho_{Sn}^{bulk}\frac{R_{Cu_3Sn}^0 h^2 E_{Cu_3Sn}^0}{\left(\alpha_{Cu_3Sn}\right)^3}\exp\left[\alpha_{Cu_3Sn}\left(1-\frac{h}{R_{Cu_3Sn}^0}\right)\right]\left[-\left(\alpha_{Cu_3Sn}\right)^2\right. \\
&\left.-\frac{5R_{Cu_3Sn}^0\alpha_{Cu_3Sn}}{h}+\frac{R_{Cu_3Sn}^0\left(\alpha_{Cu_3Sn}\right)^2}{h}-8\left(\frac{R_{Cu_3Sn}^0}{h}\right)^2+2\alpha_{Cu_3Sn}\left(\frac{R_{Cu_3Sn}^0}{h}\right)^2\right] \\
&-\frac{1}{6}\pi\rho_{Sn}^{bulk}\frac{R_{Cu}^0 h^2 E_{Cu}^0}{\left(\alpha_{Cu}\right)^3}\exp\left[\alpha_{Cu}\left(1-\frac{h}{R_{Cu}^0}\right)\right]\left[-\left(\alpha_{Cu}\right)^2-\frac{5R_{Cu}^0\alpha_{Cu}}{h}\right. \\
&\left.+\frac{R_{Cu}^0\left(\alpha_{Cu}\right)^2}{h}-8\left(\frac{R_{Cu}^0}{h}\right)^2+2\alpha_{Cu}\left(\frac{R_{Cu}^0}{h}\right)^2\right] \\
&-\frac{1}{12}\pi\rho_{Sn}^{bulk}\frac{R_{Cu}^0 h^2 A_{Cu}E_{Cu}^0}{\beta_{Cu}^3}\exp\left[\beta_{Cu}\left(1-\frac{h}{R_{Cu}^0}\right)\right]\left[-\beta_{Cu}^2-\frac{4R_{Cu}^0\beta_{Cu}}{h}\right. \\
&\left.+\frac{R_{Cu}^0\beta_{Cu}^2}{h}-6\left(\frac{R_{Cu}^0}{h}\right)^2+2\beta_{Cu}\left(\frac{R_{Cu}^0}{h}\right)^2\right] \\
&-\frac{1}{12}\pi\rho_{Sn}^{bulk}\frac{R_{Sn}^0 h^2 A_{Sn}E_{Sn}^0}{\beta_{Sn}^3}\exp\left[\beta_{Sn}\left(1-\frac{h}{R_{Sn}^0}\right)\right]\left[-\beta_{Sn}^2-\frac{4R_{Sn}^0\beta_{Sn}}{h}\right. \\
&\left.+\frac{R_{Sn}^0\beta_{Sn}^2}{h}-6\left(\frac{R_{Sn}^0}{h}\right)^2+2\beta_{Sn}\left(\frac{R_{Sn}^0}{h}\right)^2\right]
\end{aligned}
\qquad \text{(D.2)}
$$

# APPENDIX E

# FRACTURE MODEL WITH COHESIVE ELEMENTS

With the success of cohesive zone model, commercial finite element package ABAQUS has incorporated the cohesive zone model in its Standard package (for static analysis) and Explicit package (for dynamic analysis) modules since version 6.7.1. Here we demonstrate a simple example of cohesive element fracture as an application of the cohesive zone law discussed in previous sections.

A simple 2D model is built as a three-layer composite consisting of solder, copper and a cohesive layer in between. The solder is modeled as elastic-plastic material and the copper as elastic, and plane stress elements (CPS4) are used.

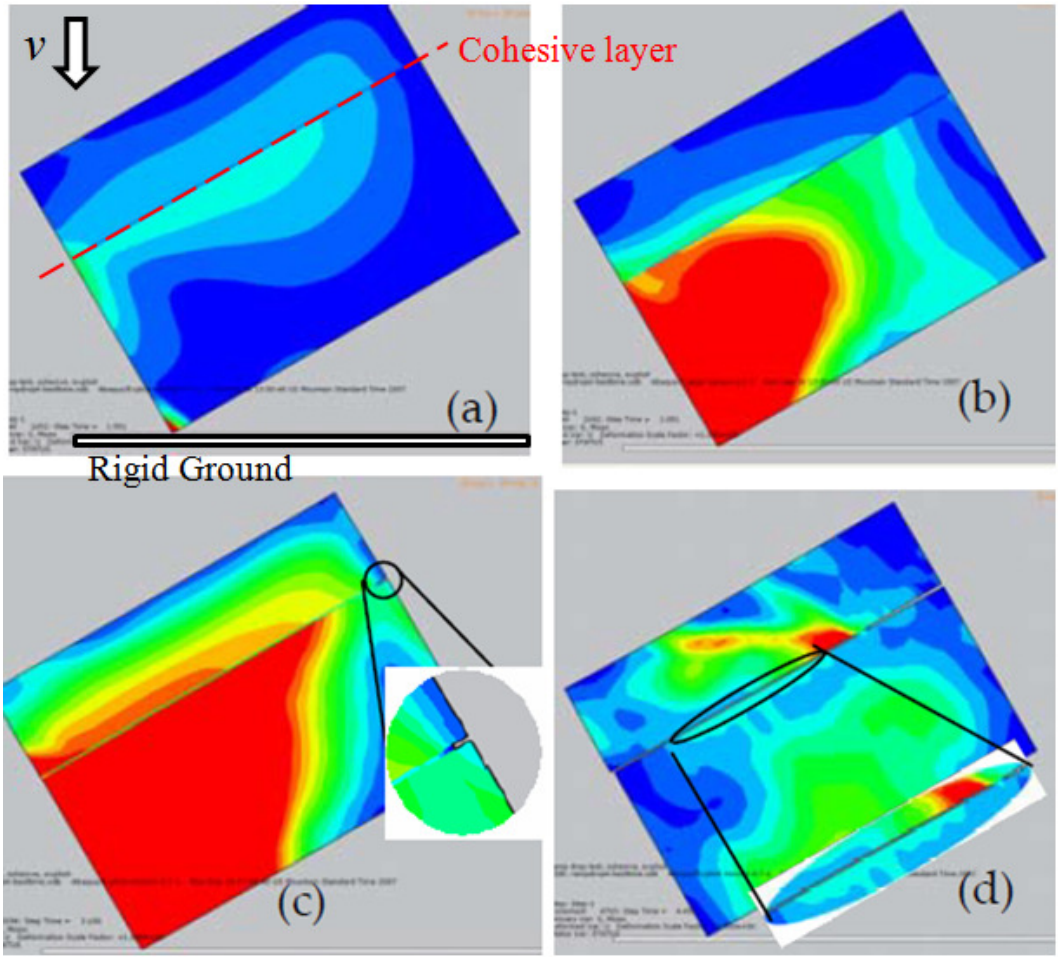


Figure E.1. Von Mises stress contour of dropping test of the 2D sandwich model at different stages. The cracks initiate and propagate due to the failure of the cohesive elements.

The cohesive layer is characterized with separation-traction constitutive relation obtained in Chapter 4. The ground is set as rigid ground. In this model, only the cohesive element is destructible, and element type for it is COH2D4 (4-node, two-dimensional cohesive element). We conduct a dynamic analysis of the object dropping down from a table, one meter above the ground. Figure E.1a shows the von Misses effective stress just after hitting the ground (t = 1.55 μs). The stress wave is clearly shown. The stress wave propagates and reaches the upper right corner of the copper layer (t = 2.05 μs), Figure E.1b. The time interval between Figure E.1a and E.1b is 0.5 μs. This agrees very well with theoretical analysis based on the stress wave speed given by $\sqrt{E_{Cu} / \rho_{Cu}}$ , where $E_{Cu}$ (= 116.5 GPa) and $\rho_{Cu}$ (= 8.96 g/cm3) are shear modulus and density of the copper, respectively. Finally, the stress wave propagates through the intermetallic layer. The stress wave increases the stress level in the intermetallic layer and causes delamination of this layer at the upper corner, Figure E.1c. Unlike the steady-state crack propagation problem, the crack at the upper corner of the intermetallic layer does not immediately propagate through the entire layer because the cracking process releases the stress. It is interesting to observe that the next interfacial crack appears at the other side of the intermetallic layer when the stress wave bounces back, Figure E.1d. This unusual but reasonable fracture phenomenon is due to the dynamic mechanical shock process and provides an insight on how to design the intermetallic and solder layers to prevent crack nucleation and propagation.

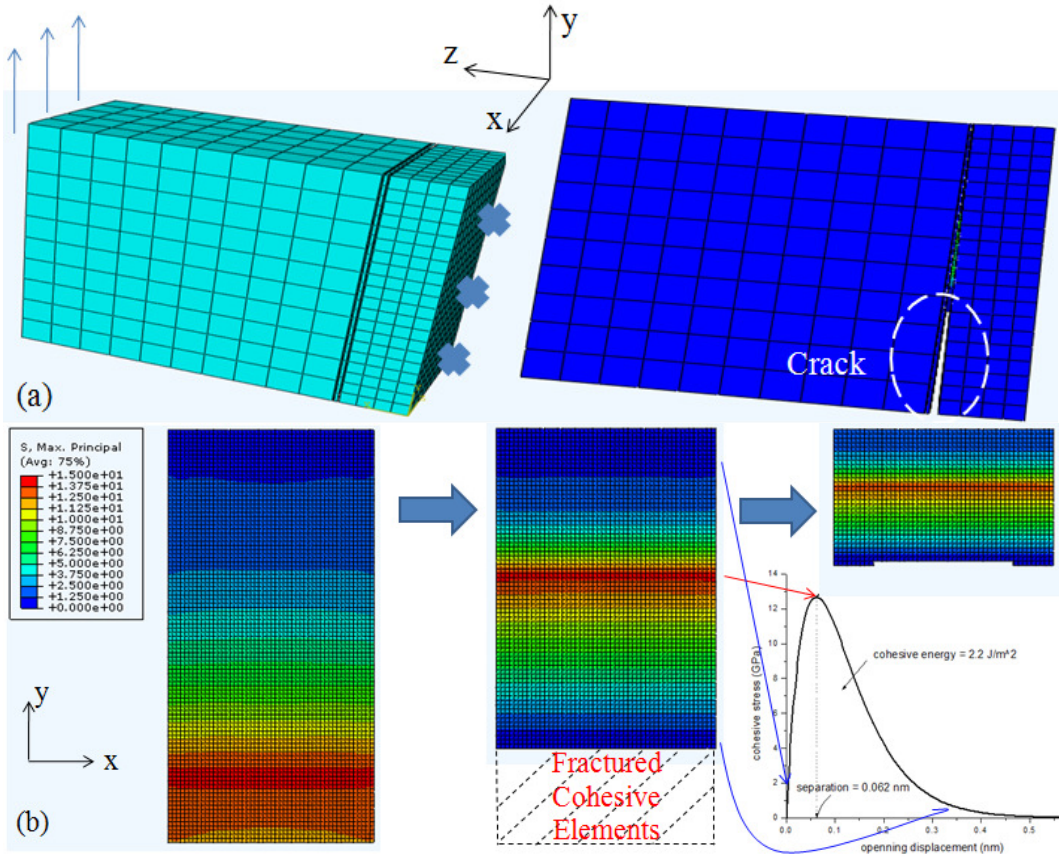


Figure E.2. (a) The geometry, boundary condition and macroscopic crack of the brick model. (b) The cross-sectional view of the element deletion during the crack propagation.

Moreover, a brick model is constructed to demonstrate the usage of 3D cohesive elements (COH3D8). The brick is subjected to shear loads at left end, and the right end is fixed. Again, other materials in this model are not breakable, only the cohesive element is destructible. Figure E.2a demonstrates the crack opening due to the shear load. Figure E.2b shows the cross-sectional view of the cohesive elements (the copper and solder elements are hidden). The cohesive elements are deleted due to the failure, during the crack propagation. The stress distribution of the cohesive section correlates very well with the inputted traction-separation law.

# APPENDIX F

# COPYRIGHT

This dissertation includes some of my own published work. The detailed copyright permission is showing as below.

Chapter 2 is reproduced with permission from K. E. Yazzie, H. Fei, J. J. Williams, H. Jiang, N. Chawla, Mechanical Shock Behavior of Bulk Pure Sn Solder, Journal of Electronic Materials 38 (2009) 2746. Copyright © 2009 TMS (The Minerals, Metals & Materials Society).

Chapter 4 is reproduced with permission from H. Fei, K. Yazzie, J. Williams, N. Chawla, H. Jiang, Multiscale Modeling of the Interfacial Fracture Behavior in the Sn-Cu-6 Sn-5-Cu System, Journal of Computational and Theoretical Nanoscience 8 (2011) 873. Copyright © 2011 American Scientific Publishers.